Sustainable Materials and Process Techniques for Engineering Solution-Based Organic Light-Emitting Devices

Serpil Tekoglu

Dissertation submitted as a requirement for the degree of Doctor of Engineering (Dr.-Ing)

July 2018 – Technical University of Darmstadt (TUD) – D17

TECHNISCHE
UNIVERSITÄT
DARMSTADT

Sustainable Materials and Process Techniques for Engineering Solution-Based Organic Light-Emitting Devices

Dissertation submitted to the Department of Materials and Earth Sciences at Technische Universität Darmstadt

In Fulfillment of the Requirements for the Degree of Doctor of Engineering (Dr.-Ing.)

by

Serpil Tekoglu

Born in Turkey

Referee: Prof. Dr.-Ing. Horst Hahn
Co-Referee: Prof. Dr.rer.nat. Uli Lemmer

Darmstadt 2018

Tekoglu, Serpil: Sustainable Materials and Process Techniques for Engineering Solution-Based Organic Light-Emitting Devices
Darmstadt, Technische Universität Darmstadt
Publication Year of Dissertation at TUprints: 2018

Date of Submission: 26.07.2018
Date of Oral Examination: 16.10.2018

Darmstadt – D 17

Please quote this document as:
URN: urn:nbn:de:tuda-tuprints-85642
URL: http://tuprints.ulb.tu-darmstadt.de/id/eprint/8564

This Document is provided by TUprints,
E-Publishing-Service of TU Darmstadt
http://tuprints.ulb.tu-darmstadt.de
tuprints@ulb.tu-darmstadt.de

Erklärung zur Dissertation

Hiermit versichere ich, die vorliegende Dissertation ohne Hilfe Dritter nur mit den angegebenen Quellen und Hilfsmittel angefertigt zu haben. Alle Stellen, die aus Quellen entnommen wurden, sind als solche kenntlich gemacht. Diese Arbeit hat in gleicher oder ähnlicher Form noch keiner Prüfungsbehörde vorgelegen.

Heidelberg, den 31. Januar 2019

_____

Serpil Tekoglu

Abstract

Sustainable Materials and Process Techniques for Engineering Solution-Based Organic Light-Emitting Devices

Advances in organic light emitting devices are crucial for the development of the display and solid state lighting (SSL) technologies. This dissertation is organized and pursued in three main projects to meet some problems in the field.

Printing technologies can be the key to next-generation affordable, flexible, large area displays and lighting elements by eliminating vacuum processing. In the first part of the thesis, the conventional gravure printing technique was adapted for the processing of emissive layers in the small molecule based organic light-emitting diodes (OLEDs) and light-emitting electrochemical cells (LECs). The homogeneous printed layers were granted by either modifying the functional ink properties or altering the printing process parameters. Different functional inks comprising the small molecule as an emissive material were formulated by adjusting viscosity, surface tension, and solvent drying kinetics of the inks. As for the process parameters, the gravure cell parameters such as line screen and tone values were altered to control the overall transfer volume of the ink and the thickness of the printed layers. In both cases, the electrically inert polymers were used as host materials to modify the rheological behavior of the ink while suppressing the aggregation of the small molecule in a solid film. The thin film characteristics of printed layers were analyzed in both qualitative and quantitative ways. The printed films were successfully implemented in the active layer of efficient small molecule based electroluminescent devices on flexible plastic foil. The optical and electrical device performance were considered as well as the effect of the printing process in comparison to spin-coated pristine small molecule based reference devices. The quality and performance of the printed emissive layers in both device type showed that the gravure printing method can be an alternative solution for wet-processing roll-to-roll (R2R) manufacturing in the future.

White light-emitting diodes draw particular attention in the field, due to their potential application as the backlight in displays or as energy efficient luminaires for SSL. Even though polymer OLEDs are well-suited for wet-based continues R2R fabrication, evaporation of low work function cathodes and therewith encapsulation remain as major obstacles. In the second part of the work, a novel hybrid device architecture was suggested for the color-tuning and

white light emission in polymer light-emitting diodes. The single component polymer LEC layer performed as the electron injection layer as well as the second emissive layer on top of a conventional polymer OLED stack. The hybrid structure maintained a sufficient charge carrier injection from an air-stable cathode, due to the unique operation principles of LECs. As a proof of charge transport at the intersection of two emissive layers, dual color emission was simultaneously observed in a bilayer device configuration. A color-tuning in emission was obtained by changing the thickness of the LEC layer. The emission of hybrid devices was shifted from yellow to white light emission region of the CIE color chromaticity diagram, resulting in OLEDs with the high color temperature values. The results demonstrated that this approach showed a promising potential to achieve color-tuning and white light emission from solution processed OLEDs bearing air-stable cathodes.

Sustainable bioelectronics is an emerging technology which to replace conventional electronics with disposable counterparts in the future. Thus, bioinspired and bioderived materials usage in organic electroluminescent devices gained much attention in the last years. In the last part of the thesis, we investigated biodegradable natural and naturally derived polymers such as gelatin, deoxyribonucleic acid (DNA) as the ion-solvating polymers in the emissive layer of polymer LECs. Notably, we focused on DNA and DNA-lipid complex based polyelectrolytes due to the unique hybrid ionic/electronic conductivity behavior of DNA. Different solid polymer electrolytes (SPE) were tested with varying additives of salts at different ratios towards improving the ionic conductivity. Additionally, the electrochemical stability window of SPEs was defined to eliminate nonreversible electrochemical side reactions during device operation. The optoelectrical device characteristics, as well as lifetime measurements, were obtained to determine the stability of LECs. Furthermore, the surface morphology of the active layers was investigated to characterize the phase separation between SPE and emissive polymer and aggregations in thin films, which have a significant influence on the device performance. Biosolid polymer electrolytes were successfully implemented in LECs as promising materials of bio-based LECs.

Zusammenfassung

Nachhaltige Materialien und Prozessierungstechnologien für die Entwicklung flüssig-prozessierter organischer Leuchtdioden

Fortschritte im Bereich organischer, lichtemittierender Bauteile sind unerlässlich für die Entwicklung neuer Bildschirm- und Feststoffbeleuchtungstechnologien. Diese Dissertation ist thematisch in drei Projekte unterteilt, welche jeweils einige der Probleme in diesem Forschungsfeld adressieren.

Drucktechnologien könnten durch die Eliminierung aufwendiger Vakuumprozessschritte der Schlüssel zur Realisierung kostengünstiger, flexibler und großflächiger Bildschirme und Beleuchtungselemente der nächsten Generation sein. Im ersten Projekt wurde konventioneller Tiefdruck für die Prozessierung der Emissionsschicht organischer Leuchtdioden (OLEDs) und lichtemittierender elektrochemischer Zellen (LECs) auf der Basis kleiner Moleküle untersucht. Homogene gedruckte Schichten wurden entweder durch Anpassung der funktionellen Tinte oder der Druckprozessparameter erzielt. Es wurden verschiedene funktionelle Tinten, welche kleine Moleküle als Emitter beinhalteten, formuliert und Viskosität, Oberflächenspannung und Trocknungsverhalten eingestellt. Hinsichtlich der Prozessparameter wurden Raster und Tonwert des Tiefdruckzylinders angepasst, um das transferierte Tintenvolumen und damit die Dicke der gedruckten Filme einzustellen. Elektrisch inerte Polymere wurden dabei als Matrix genutzt, um die rheologischen Eigenschaften der Tinte zu beeinflussen und gleichzeitig eine Agglomeration der kleinen Moleküle im resultierenden Materialfilm zu unterdrücken. Die Dünnfilmeigenschaften der gedruckten Schichten wurden sowohl qualitativ als auch quantitativ untersucht. Die Druckergebnisse wurden weiterhin erfolgreich als Aktivschicht in effizienten elektrolumineszenten Bauteilen auf Plastikfolien eingesetzt. Die optischen und elektrischen Bauteileigenschaften wurden im Hinblick auf Einflüsse des Druckprozesses untersucht und mit Referenzbauteilen ohne Polymermatrix, welche durch Rotationsbeschichtung hergestellt wurden, verglichen. Der Vergleich der Leistungsfähigkeit der Emissionsschichten zeigte, dass Tiefdruck eine mögliche Methode für die zukünftige Herstellung opto-elektrischer Bauteile mittels Rolle-zu-Rolle-Verfahren ist.

Weiß leuchtende Dioden erfahren aufgrund ihrer potentiellen Anwendung als Hintergrundbeleuchtung in Bildschirmen und als energieeffizientes Leuchtmittel besondere Aufmerksamkeit. Wenngleich polymerbasierte OLEDs mittels Rolle-zu-Rolle basierter Nassfilmtechnologien hergestellt werden können, stellen das Aufdampfen der reaktiven

Kathode und damit einhergehend die Einkapselung der Bauteile Hindernisse dar. Daher wurde im zweiten Projekt eine neuartige Hybridbauteilarchitektur vorgeschlagen, welche eine Anpassung der Emissionsfarbe in Richtung Weißpunkt ermöglicht. Die hierbei eingesetzte polymerbasierte, einkomponentige LEC-Schicht fungiert als Elektroneninjektionsschicht sowie als zweite Emissionsschicht und wurde auf einem konventionellen OLED-Aufbau abgeschieden. Aufgrund der physikalischen Funktionsweise von LECs garantierte die Hybridstruktur eine ausreichende Ladungsträgerinjektion aus einer luftstabilen Kathode. Als Beweis des vorliegenden Ladungsträgertransportes an der Grenzfläche der beiden Emissionsschichten wurde simultan die Emission beider Materialien beobachtet. Durch Veränderung der Dicke der LEC-Schicht konnte die hieraus resultierende Emissionsfarbe angepasst werden. Die Emission wurde ausgehend vom gelb-grünen Bereich im CIE Farbraum bis in die Nähe des Weißpunkts verschoben und es wurden OLEDs mit einer hohen Farbtemperatur realisiert. Die Ergebnisse demonstrieren, dass es sich hierbei um einen vielversprechenden Ansatz handelt, um die Emissionsfarbe flüssig hergestellter OLEDs mit luftstabilen Kathoden anzupassen und Weißlichtemission zu erzielen.

Nachhaltige Bioelektronik ist eine aufstrebende Technologie mit dem Ziel, konventionelle in Wegwerfprodukten eingesetzte Elektronik zu ersetzen. Daher erfährt die Nutzung biologisch inspirierter Materialien in organischen, elektrolumineszenten Bauteilen ein großes Interesse in den letzten Jahren. Im dritten Projekt wurden biologisch abbaubare, natürliche Polymere bzw. hiervon abgeleitete Materialien wie Gelatine und Desoxyribonukleinsäure (DNS) als Ionen-lösende Polymere in der Emissionsschicht polymerbasierter LECs untersucht. Der Fokus lag hierbei insbesondere auf Polyelektrolyten auf der Basis von DNS und DNS-Lipid-Komplexen aufgrund deren einzigartiger hybrider ionisch-/elektronischer Leitfähigkeit. Verschiedene Feststoffpolymerelektrolyte (SPEs) wurden mit Salz-Additiven gemischt und im Hinblick auf eine Verbesserung der ionischen Leitfähigkeit untersucht. Außerdem wurde das elektrochemische Stabilitätsfenster der SPEs bestimmt, um irreversible elektrochemische Nebenreaktionen während des Betriebs der Bauteile auszuschließen. Es wurden sowohl die opto-elektrischen Eigenschaften als auch die Betriebslebensdauer der elektrochemischen Zellen bestimmt. Zusätzlich wurde die Oberfläche der aktiven Schicht der Bauteile im Hinblick auf eine mögliche Phasentrennung von SPE und Emittermaterial untersucht, da eine solche üblicherweise einen großen Einfluss auf die Performance der Bauteile hat. Biopolymere wurden erfolgreich als Feststoffelektrolyt in LECs verbaut und es wurde somit die Machbarkeit von LECs auf der Basis biologischer Materialien nachgewiesen.

Curriculum Vitae

SERPIL TEKOGLU

Karlsruhe Institute of Technology (KIT), Light Technology Institute (LTI)
Engesserstrasse 13, Gebäude 30.34, 76131 Karlsruhe, GERMANY
Gsm: +49 (0)152 599 26722, Office: +49 (0)6221 5419134
Email: serpil1305@yahoo.com

Place of Birth: Sivrihisar/ Turkey

EDUCATION:

2014-2018	Ph.D. Technical University of Darmstadt, Department of Materials and Earth Sciences Supervision: Prof. Horst Hahn 2nd Supervision: Prof. Uli Lemmer (KIT, LTI)
2006-2009	M.Sc. Ege University / Izmir-Turkey Solar Energy Institute (Energy Department) Supervision: Prof. Sule Erten-Ela CGPA: 89/100
2001-2006	B.Sc. 9 Eylül University / Izmir –Turkey Department of Science and Mathematics, Division of Chemistry Education CGPA: 3.02/4

WORK EXPERIENCE:

2012-2016	Research Scientist at Karlsruhe Institute of Technology , Light Technology Institute, Karlsruhe/Germany (Prof. Uli Lemmer)
2009-2010 (17 months)	Reserach Scientist at Johannes Kepler University, Linz Institute for Oranic Solar Cells (LIOS), Linz/Austria (Prof. N. Serdar Sariciftci)

PUBLICATIONS:

1) **S. Tekoglu,** G. N. Yeo, M. Bender, A. Morfa, U. Lemmer, M. Hamburger and G. Hernandez-Sosa, "*Deoxyribonucleic acid (DNA) Based Polymer Electrolyte Systems for Light-Emitting Electrochemical Cells*", (Manuscript).
2) J. Zimmermann, N. Jürgensen, A. J. Morfa, B. Wang, **S. Tekoglu** and G. Hernandez-Sosa, "*Poly (lactic-co-glycolic acid) (PLGA) as Ion-Conducting Polymer for Biodegradable Light-Emitting Electrochemical Cells*", ACS Sustainable Chem. Eng. 2016, doi**:**10.1021/acssuschemeng.6b01953.
3) S. Raupp, D. Daumm, **S. Tekoglu**, L. Merklein, U. Lemmer, G Hernandez-Sosa, E. Dörsam, P. Scharfer and W. Schabel, "*Slot Die Coated and Flexo Printing Highly Efficient Small SMOLEDs*", (Advanced Materials Technologies, http://dx.doi.org/10.1002/admt.201600230.
4) **S. Tekoglu,** M. Petzoldt, S. Stolz, U. Lemmer, U. Bunz, M. Hamburger and G. Hernandez-Sosa, "*Emissive Polyelectrolytes as Interlayer for Color-Tuning and Electron Injection in Solution-Processed Light-Emitting Devices*", ACS App. Mater. Interfaces, 2016, 8(11), pp 7320-7325.
5) G. Hernandez-Sosa, **S. Tekoglu**, S. Stolz, R. Eckstein, J. Trapp, C. Teusch, U. Lemmer, M. Hamburger and N. Mechau, "*The Compromises of Printing Organic Electronics: A Case Study of Gravure Printed Light-Emitting Electrochemical Cells*", Advanced Materials, 2014, doi:10.1002/adma.201305541.
6) **S. Tekoglu**, G. Hernandez-Sosa, E. Kluge, U. Lemmer, N. Mechau, "*Gravure Printed Flexible Small-Molecule Organic Light Emitting Diodes*", Organic Electronics, 14, (2013) 3493-3499.
7) G. Hernandez-Sosa, R. Eckstein, **S. Tekoglu**, T. Becker, F. Mathies, U. Lemmer and N. Mechau, "*The Role of the Polymer Solid Electrolyte Molecular Weight in Light-Emitting Electrochemical Cells"*, Organic Electronics, Vol:14, Issue 9, pages 2223-2227 (2013).
8) S. Erten-Ela, M. Marszalek**, S. Tekoglu,** M. Can and Siddik Icli, *"Synthesis, characterization and photovoltaic properties of novel molecules based on triarylamine dyes"*, Current Applied Physics, Vol:10, Issue 3, pages 749-756 (2010).

Book Chapter:

1) G. Hernandez-Sosa, A. J. Morfa, N. Jürgensen, **S. Tekoglu**, J. Zimmermann, (2017) Morphology Engineering and Industrial Relevant Device Processing of Light-Emitting Electrochemical Cells. In: R. Costa (ed) Light-Emitting Electrochemical Cells. Springer.

SYMPOSIUMS& WORKSHOPS:

1) **S. Tekoglu,** G. N. Yeo, M. Bender, A. Morfa, U. Lemmer, M. Hamburger and G. Hernandez-Sosa, "*Deoxyribonucleic acid (DNA) Based Polymer Electrolyte Systems for Light-Emitting Electrochemical Cells*", November 19-21, 2016, Hannover, Germany.
2) **S. Tekoglu,** G. Ni Yeo, M. Bender, A. J. Morfa, U. Lemmer, M. Hamburger and G. Hernandez-Sosa, "Bio- organic light-emitting electrochemical cells comprising DNA-based polymer electrolytes", International Workshop on Advanced Materials and Processes for Energy Applications, April 20-24, 2016, Istanbul, Turkey. (Invited Flash Talk)*
3) **S. Tekoglu,** G. Ni Yeo, M. Bender, A. J. Morfa, U. Lemmer, M. Hamburger and G. Hernandez-Sosa, "DNA-Based Solid Polyelectrolytes for Bio Light-Emitting Electrochemical Cells: BioLECs", BioEL 2016, March 21, 2016. (Talk)*
4) **S. Tekoglu,** M. Petzoldt, S. Stolz, U. Lemmer, U. Bunz, M. Hamburger and G. Hernandez-Sosa, "LEC/OLED Hybrid Device Architecture for Solution-Processed Multi-Color Emission Devices", MRS Fall, 29 Nov-04 Dec 2015, Boston, USA.
5) I. Oner, **S. Tekoglu**, G. Hernandez-Sosa, U. Lemmer, C. Varlikli, "Fabrication of Large-Area White Organic Light Emitting Diodes (WOLED) by Blade Coating", 01-04 October 2015, Istanbul, Turkey.
6) **S. Tekoglu,** M. Petzoldt, S. Stolz, U. Lemmer, U. Bunz, M. Hamburger and G. Hernandez-Sosa, "Precise Color-Tuning using Solution Processed LECs in Hybrid Device Architecure", SPIE, 9-13 August 2015, San Diego, USA.
7) **S. Tekoglu**, D. Daume, C. Leonhard, E. Kluge, E. Dörsam, U. Lemmer, N. Mechau, G. Hernandez-Sosa, Ink Formulation for Gravure Printed Organic Light-Emitting Devices, 10th International Conference on Electroluminescence and Organic Optoelectronics (ICEL-10), August 31 - September 3, 2014, Cologne, Germany.
8) **S. Tekoglu**, D. Daume, C. Leonhard, E. Kluge, E. Dörsam, U. Lemmer, N. Mechau, G. Hernandez-Sosa, Ink Formulation for Gravure Printed Organic Light-Emitting Devices, The Internatıonal Workshop on Flexible Bio- and Organic Printed Electronics (IWOBOE), 1-3 May 2014, Konya, Turkey.
9) **S. Tekoglu**, G. Hernandez-Sosa, E. Kluge, U. Lemmer, N. Mechau, "Flexible Small Molecular Phosphorescent Organic Light Emitting Diodes by Gravure Printing Technique", NanoMat Symposium, 26-27 September 2013, Karlsruhe, Germany.
10) **S. Tekoglu**, G. Hernandez-Sosa, E. Kluge, U. Lemmer, N. Mechau,*"Fabrication of Small Molecule Organic Light Emitting Diodes by Gravure Printing",* MRS Spring Meeting Spring 2013, 1-5 April, San Francisco, USA.
11) **S. Tekoglu**, U. Abaci, M. Kus, C. Ünlü, S. Tilki, S. Özcelik, N. S. Sariciftci, *Influence of alloyed nanocrystal doping on performance of polymer-hybrid light emitting diodes (PLEDs),* The 3rd International Symposium on Flexible Organic Electronics (IS-FOE10)**,** 6-9 July 2010**,** Halkidiki, Greece**.**
12) **S. Tekoglu**, U. Abaci, M. Kus, C. Ünlü, S. Tilki, S. Özcelik, N. S. Sariciftci, *Electroluminescence enhancement of alloyed CdS_xSe_{1-x} doped polymer-hybrid light emitting diodes (PLEDs),* NanoTR-VI Conference 15-18 June 2010, Izmir Institute of Technology, Izmir-Cesme, Turkey.
13) **S. Tekoglu**, A. Montaigne Ramil, B. Meana-Esteban, A. Balan, D. Baran, L. Toppare, H. Neugebauer, and N. S. Sariciftci, *Investigation of Transport Properties of a New Donor-Acceptor Polymer, Poly-2-Dodecyl-4,7-Di(Thiophene-2-yl)-2H-Benzo[1,2,3] Triazole (PTBT),* NFN Winterschool on Organic
14) **S. Tekoglu**, M. Egginger, S. Erten-Ela, S. Icli, N. S. Sariciftci, *"Investigation of Different Organic Field Effect Transistor Geometries",* NanoTR-IV Conference 9-13 June 2008, Istanbul Technical University, Istanbul, Turkey. (Talk)*
15) **S, Tekoglu**, M. E. Akin, S. Cogal, S. Erten, S. Icli, "*Perylene Based Heterojunction Solar Cell:'Tang Cell",* NanoTR-III , 11-14 June 2007, Bilkent University, Ankara, Turkey. (Talk)*

AWARDS and GRANTS:

11-12.2015 (7days) German Academic Exchange Service (DAAD) Scholarship, Material Research Society (MRS) Fall 2015, Boston, USA.

06-07.2013 (11days) Inter-Continental Advanced Materials for Photonics (I-CAMP'13) Summer School participation fellowship, Cambridge, United Kingdom.

2009-2010 (17months) The Marie Curie Research Training Network (MC-RTN) within FP6 - Early Stage Researcher (ESR), Johannes Kepler University, Linz, Austria.

2007-2008 (3months) Socrates-Erasmus Exchange Program, Johannes Kepler University, Institute for Organic Solar Cells (LIOS), Austria.

OTHER PROFESSIONAL ACTIVITIES:

- Member of the Organizing Committee - International Workshop on Flexible Bio- and Organic Printed Electronics (IWOBOE), 1-3 May2014, Konya, Turkey.
- Invited Talk - Linz Institute for Solar Cells (LIOS), Johannes Kepler University, Linz, Austria, "Ink formulation for gravure printed phosphorescent light emitting diodes", 27.03-28.03.2014.
- Scientific visit (3 weeks) - The National Research Council (CNR), Institute for Macromolecular Studies, (ISMac), Milan/Italy. 17.05-05.06.2010.
- Supervisor and coordinator for the Nanotechnology Lab. Course (Fabrication and Characterization of OFETs) during 2013 - 2016.
- Nominally supervised master's thesis:

(1) Bohui WANG, Master's Thesis, "Investigation of PLGA-based Polymer Solid Electrolyte Systems for Light-Emitting Electrochemical Cells"**,** 23rd December 2014, Light Technology Institute, Karlsruhe Institute of Technology. (Supervisor: Serpil Tekoglu)

(2) Guan Ni YEO, Master's Thesis, "Investigation of DNA-based Polymer Solid Electrolyte Systems for Light- Emitting Electrochemical Cells", 5th September 2014, Light Technology Institute, Karlsruhe Institute of Technology. (Supervisor: Serpil Tekoglu)

Acknowledgments

I would like to take the opportunity and express my thanks to all those people who helped me to make this thesis possible by giving endless support and encouragement. I am incredibly indebted to Prof. Uli Lemmer for giving me the possibility to work in KIT group at InnovationLab and providing necessary infrastructure and resources to accomplish my research work. I'm very much thankful to Prof. Horst Hahn for accepting me as his Ph.D. student at the critical stage of the individual Ph.D. program. I warmly thank our group leader Dr. Gerardo Hernandez-Sosa for his advice and constructive criticism for my work. I sincerely thank our former group leader Dr. Norman Mechau, for giving me encouragement and freedom to start working on DNA material.

Most of the results described in this thesis would not have been succeeded without collaboration with some researchers. I would like gratefully acknowledge Dr. Manuel Hamburger for fruitful discussions and supplying freshly synthesized materials. I want to thank Dominik Daume, Sebastian Raupp and Christoph Leonhard for the excellent collaborative work within the PrintOLED project. I want to acknowledge Dr. Martin Petzoldt and Dr. Markus Bender for the synthesis of a few materials which were utilized in this thesis. My warm appreciation is due to my master students Guan Ni Yeo and Bohui Wang for their successful work which contributed to the findings in this dissertation. I would like kindly acknowledge Dr. Sebastian Beck for infrared spectroscopy measurements. Also, I expand my thanks to our group members Anthony, Sebastian S., Ralph, Tobias for all discussions and helpful suggestions! Sharing an office with seven guys for almost four years brought a different perspective on life.

InnovationLab has a different meaning in the heart. Not only the scientific staff but also the people administrative people at the 9th floor support me during writing my dissertation. Special thanks go to Hildegard for her support and solving the conflicts. Thomas Peissing, thank you for your big heart, positive smiles, and technical assistance. You showed me that it is possible to get along well, even if you do not speak a common language.

My sincere gratitude goes to Derya and Asli for their endless encouragement and constant moral support. Thank you for your tolerance and accepting me as I am. Derya, my Sis, my soulmate, thank you for being there whenever I need. Asli deserved special mention here for proofreading of some chapters. I am grateful to my best friends Cihan and Piotr for their love, care, and support. Cihan and Cumhur deserved special thanks for their technical assistance when my laptop was crashed.

The last, but not the least, a deep appreciation goes to my family for their endless support and love. Son olarak teşekkürlerimi aileme sunmak istiyorum. Anne ve Baba, bu uzun yolculukta beni yalnız bırakmadığınız icin sonsuz teşekkürler! Ve zor günlerimde odamı aydınlatan iki küçük ruh “İrem ve Dila”, sizin yeriniz çok ayrı…

"It is during our darkest moments that we must focus to see the light."

Aristotle

"Varsın küçücük olsun fütuhatın, fakat bil,
Onu fetheden sensin, yoksa başkası değil."

Cyrano de Bergerac / Edmond Rostand

Dedicated to the dark lady of DNA, ***Rosalind Franklin****,*

and all invisible women in science…

Table of Contents

List of figures

List of tables

Abbreviations and list of symbols

CCT	Correlated Color Temperature
CRI	Color Rendering Index
CT	Charge Transfer
DNA	Deoxyribonucleic acid
E_g **or** E_{opt}	Optical Band Gap
EL	Electroluminescence
EQE	External Quantum Efficiency
FTIR	Fourier Transform Infrared Spectroscopy
HOMO	Highest Occupied Molecular Orbital
IQE	Internal Quantum Efficiency
J-V	Current Density- Voltage
LUMO	Lowest Unoccupied Molecular Orbital
L-V	Luminance-Voltage
MEH-PPV	Poly[2-methoxy-5-(2-ethylhexyloxy)-1,4-phenylenevinylene]
OD	Optical Density
OLED	Organic Light Emitting Diode
OPV	Organic Photovoltaic
OSC	Organic Semiconductor
PEDOT:PSS	Poly(3,4 ethylenedioxythiophene):poly(styrenesulfonate)
PL	Photoluminescence
PMMA	Polymethyl methacrylate
RGB	Red-Green- Blue
SCE	The Saturated Calomel Electrode
TADF	Thermally Activated Delayed Fluorescence
a	Absorbance
c	Speed of Light
E	Electric Field
h	Planck's Constant
v	Photon Energy
Ɛ	Dielectric Constant
σ	Conductivity
Φ_f	Fluorescence Quantum Efficiency
S_1	Singlet Excited State
T_1	Triplet Excited State
ΔE	Energetic Loss
μ	Mobility
π – π*	pi-pi*
σ – σ*	sigma-sigma*

Chapter 1
Introduction

Rapid progress in technology and electronics have brought about adverse effects on the environment. Global electricity consumption for artificial lighting as well as increasing electronic waste generation contributes to these environmental problems. Therefore, there is a demand for energy-saving lighting technology such as organic electroluminescent devices and sustainable electronics[1].

Organic electroluminescent devices studied in this thesis are the main focus for the display and solid state lighting (SSL) technology. Their low power consumption during operation, easy and low-cost fabrication makes them advantageous over their conventional counterparts[2]. As a consequence, organic light-emitting diode (OLED) displays have become the real asset of organic semiconductors in large scale electronics production.

This chapter gives an overview of the technological developments in the field. Afterward, the outline of the thesis will be laid out.

1.1 General overview and motivation

There is a close relationship between material development and engineering. While engineering describes the demand and design, materials provide the artifacts. Advancements in one have triggered advances in the other. New materials and methods to process materials lead engineering possibilities which result in novel products or improved product performance. For example, everyday products such as light-emitting diode light bulbs, optical-fiber-based cable television, compact disc players have been produced thanks to the invention of the molecular beam epitaxy process forming compound semiconductor materials at atomic level[3].

The technology is currently evolving at a more rapid pace than at any point in history. As a result, modern technology has become indispensable for us. We are surrounded by electronics such as sensors, displays, lasers, etc., assisting our daily routine. In the electronics industry, the higher demand of the market led to higher energy consumption during the fabrication process. The higher energy consumption in the manufacturing process for inorganic semiconductors and wafers played a critical role in the electronics evolution where high-quality inorganic semiconductors were replaced with less energy required organic semiconductors during their fabrication[4].

After the discovery of semiconducting polymers in 1977 [5], they became an alternative class of materials, owing to features such as lightness, flexibility and solution processability. Organic materials have the potential to reduce the cost in fabrication even further, through roll-to-roll processing on flexible and cheap plastic or paper sheets as a substrate, using more energy-efficient manufacturing techniques such as printing and coating[6]. Thanks to the intense efforts of researchers during the past 40 years, currently, printed applications in photovoltaics, flexible displays, lighting, electronics, and integrated smart systems are a few examples of the market that will be revolutionized by organic and printed electronics as pointed out by Organic and Printed Electronics Association[7].

According to the OE-A Roadmap 2017, OLED displays, the only real presence of organic semiconductors in large scale electronics production worldwide, account for the largest share of the organic and printed electronics market[7]. So, the organic semiconductors draw increasing attention in the field of displays. Several milestones have been made in the improvement of the emissive materials used in these devices after the world's first practical OLED released in 1987[8]. Nevertheless, the low charge mobility and air stability of organic semiconductors remain the two obstacles for the high performance of organic electronic devices comparing to the inorganic ones based on silicon and gallium arsenide. However, the efficient and high mobility luminescent materials open up a new gate for the device processing in the direction of printing materials by using the most suitable techniques. In the field of printing and coating, many of the same methods are common in graphics and the coatings industry and require modifications in respect to printing units, process parameters, and ink formulations to be used in organic electronics for resolution, film thickness, etc. Related work is summarized in Chapter 4 in detail.

Rapid progress in technology and electronic products have brought about the environmental impact which is another major concern of people today. Consumers tend to replace existing electronic products when they are damaged or outdated, or a new product is introduced to the market. Electronic waste (e-waste) is defined as all types of electrical or electronic equipment and its parts that have been discarded without intention for reuse by the owner[9]. Global e-waste generation was estimated to be 41.8 million tons in 2014 and is expected to reach 65.4 million tons by 2017[10]. Only an estimated 15 percent of global e-waste can be fully recycled[11]. Disposing of it in underdeveloped countries is often unsafe and leads to environmental pollution and health problems. During uncontrolled recycling procedures, workers are exposed to harmful elements in e-waste[12]. In the quest for sustainable electronics, last decade, researchers have explored the use of bio-inspired and bio-derived compounds as emerging materials. As reviewed recently, several significant contributions have been made in various applications in the field of electronics, photonics, biomedical engineering and biomimetics[1]. Organic bioelectronics will, therefore, open a pathway for the possibility of replacing disposable electronics with their conventional counterparts in the future.

In addition to the cost and environmental problems as mentioned above, another issue is the emerging need for energy-saving lighting systems. About 19% of total global electricity production is used for artificial lighting, resulting in 1900 Mt of CO_2 emission per year[13]. Solid State Lighting (SSL) technology based on both inorganic and organic materials has the potential for replacing conventional light sources by offering energy-efficient, long-term sustainable products. Particularly, SSL based on organic semiconductors in the context of display technology, has superior properties with thin, light-weight, flexible light sources deliver uniform, warm white light (sunlight-like) illumination without noise, glare or heat problem[14]. Progress in the development of white OLEDs, which uses white OLED source and color filters on top, has also triggered advancements in OLED lighting. Different approaches have been made to obtain white light emission and color-tuning. Further details and relevant work are shown in Chapter 5.

In 1995, light emitting electrochemical cells (LECs) came out[15] as an alternative device concept to OLEDs. LECs have always been considered the simplest SSL device[16]. They are prominent with fault-tolerant thickness properties for the roll to roll mass processing in ambient conditions[17]. In-situ doping characteristic of the device concept enables using air-stable electrodes and renders the possibility to eliminate encapsulation. However, despite the simple device structure, the underlying device physic of LECs is complex. The origin of degradation is still not very well understood, and ion-solvating polymers with large electrochemical stability window are proposed as a probable solution for better performance[16]. Seeking a variety of polyelectrolyte systems suggests the question of how to incorporate particularly natural polyelectrolytes in LECs. This approach would also be beneficial for the future of sustainable electronics. Related work can be read in Chapter 6 in detail.

The interplay between materials and engineering is still ongoing by developing widely different material systems and different process techniques. Currently, the ultimate goal in the field of organic electronics is to search for new materials and methods to achieve fully printed, cheap and eco-friendly electronics. Therefore, in this thesis, we have investigated sustainable materials and processing methods for engineering electroluminescent devices.

1.2 Outline of the thesis

This thesis spans material characterization and processing techniques, as well as device design. The work on the feasibility of various materials for wet processing, in combination with different device concepts, will be laid out to address some of the problems which were mentioned above.

First, we adapted the gravure printing technique for printing the organic layers of small molecule LEDs on a flexible substrate and confirmed that the strategy used for the ink formulation could be transferred to different material combinations. Subsequently, we printed solid polymer electrolytes bearing small molecule, to achieve small molecule LECs with air-stable cathodes. After, we introduced a bilayer hybrid device structure, which enables color-tuning using LEC as a potential electron injection layer in solution-processed OLEDs with the air-stable electrodes. Finally, we demonstrated the applicability of biodegradable natural materials as solid polymer electrolytes (SPE) systems for LECs as a proof of concept towards degradable luminescent devices. The thesis is divided into 7 Chapters. The following is a brief explanation of each chapter.

Chapter 1 gives an overview of the technological developments and problems in the field of organic electronics, as well as the outline of the thesis. ***Chapter 2*** describes the fundamentals of organic semiconductors in terms of band theory and charge transport. A brief history of organic light-emitting devices: fundamental materials and device breakthroughs, besides a basic understanding of their operational principles is supplied. An overview of printed organic electronics including the state-of-the-art examples and remaining challenges in the field are provided afterward. The comparison of different printing techniques is given, and the principle of the gravure printing process is elaborated.

Chapter 3 is devoted to experimental techniques and materials used in this thesis. The chemical structures of polymers and other organic compounds are given, and instructions about the experimental methods are explained. Working principles of the spectroscopic techniques (absorption, photoluminescence, and fluorescence microscopy) and electrochemical techniques

(cyclic voltammetry, impedance spectroscopy) are summarized. The physical principles of device processing methods and optoelectrical device characterization techniques are elaborated. The rheometry technique is explained in detail to define the viscosity behavior of ink formulations. The surface analysis techniques (polarized light microscopy, atomic force microscopy, and white light interferometry) are discussed for determining the film morphology.

In ***Chapter 4***, we present the implementation of the gravure printing technique for flexible Small Molecule OLEDs and Small Molecule LECs by defining the ink viscosity, the surface tension and solvent drying kinetics of the functional inks or altering the gravure cell parameters such as line screen and tone value. The film leveling and drying time are considered for a quantitative explanation of the printed layer undulations. The rheological properties of the functional ink are investigated to grant a homogeneous printed layer for device fabrication. We obtained the electrical characterization of the printed layers in the complete device stack.

In ***Chapter 5***, we introduce a novel device concept, comprising of the light-emitting electrochemical cell on top of a conventional OLED bearing a silver (Ag) cathode. The LEC layer improves the charge injection from the air-stable electrode while performing as the second emissive layer for color-tuning. The presented hybrid device structure can be potentially be used to achieve electron injection as well as color-tuning in solution processed OLEDs, employing air-stable electrodes.

Chapter 6 focuses on the investigation of biopolymers as SPEs for LECs by taking advantage of their natural ion-conducting mechanism. Different salts and plasticizers are engaged to enhance the ionic conductivity which is investigated using impedance spectroscopy. The device performances, lifetime characteristics of the devices are obtained. Morphology of the active layers is examined to understand efficiency changes. As the proof of concept; biopolymers are utilized successfully as ion solvating polymers within the active layer of LECs.

Chapter 7 provides a conclusion of the main findings of this thesis and the contribution to the field, as well as limitations and suggestions for the future research aspects.

Chapter 2
Theoretical background

Improvements and novel approaches in electroluminescent devices at lab scale are crucial for the development of flexible, bendable, rollable, even stretchable display and lighting elements, as well as their large area, low-cost production that would make them more affordable in the future. Although state-of-the-art OLED displays are already commercially available; problems such as air stability, lifetime, manufacturing costs, etc. remain challenging. Therefore, OLEDs are still drawing intense attention of industrial and scientific researchers.

In this chapter, a brief introduction to the fundamentals of organic semiconductors and the physical understanding of charge transport phenomena is presented first. Then, an overview on the historical progress of organic light-emitting devices will be laid out: principal materials and device breakthroughs; state-of-the-art architectures which those breakthroughs enabled; the current processing methods that those device concepts facilitated. After that, we will focus illustratively on the device principles and working mechanisms of OLEDs and LECs. A basic understanding of their structure and the operational principles are essential to address the remaining challenges and to propose possible solutions.

2.1 Organic semiconductors and charge transport

Organic semiconductors (OSCs) are the core elements for the discovery of organic electronics. OSCs, in general terms, are π-bonded materials represented by alternating single and double bonds (conjugation) within their carbon backbone. They are classified into two main groups with low molecular weight materials (small molecules, oligomers) and polymers. In both systems, sp^2 hybridization of carbon allows the p_z orbitals to form π-bonds, and the respective π-orbitals are 'delocalized' along the molecule, giving rise to electronic mobility along the chain and between neighbouring units. However, the conjugated double bonds do not render the electrical conductivity. Adding or removing electrons in such a system (doping) may result in high electronic conductivity. The pioneering work related to the semiconducting polymers concerned on a network, in which a halogen dopant removes an electron from delocalized bonding creating a hole[18]. Then, an electron at a neighbouring position jumps and fills that hole, generating a new hole and allowing charge to flow through the polymer chain (see Figure 2.1).

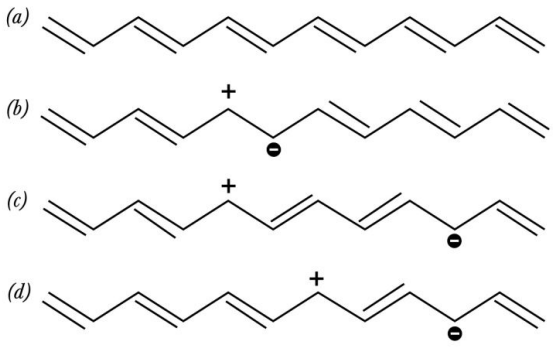

Figure 2.1The combination of the charge carrier and the polarization due to the displacement of the atoms is called a polaron. A polaron formed by removal of one electron on the 5th carbon atom of an undecahexaene chain (a→b). The polaran migration shown in (c→d). Adapted from ref.[5]. *Copyright © The Royal Swedish Academy of Sciences, source, https://www.nobelprize.org/*

All conjugated polymers posses p_z orbitals overlap and form π and π* orbitals. The energies of π and π* are defined as the highest occupied molecular orbital (HOMO), the lowest unoccupied molecular orbital (LUMO), respectively. The energy difference between HOMO and LUMO specifies the electrical band gap of organic material. In such material systems, the lowest electronic transition occurs between the π-π* bands via excitation energies between 1.1-3.5 eV[19]. The excitation energies are usually at the visible spectrum (within 380-750 nm), so the materials are defined as optically active. The possibility of changing the HOMO and LUMO levels and accordingly tuning band gap via chemical modification is one of the most important benefits of OSCs comparing to inorganic counterparts. The color of emission can be controlled by tuning the band gap of emissive materials, so that is quite advantageous for OLED display applications.

Charge transport characteristics of OSCs are more complex than in covalently bonded inorganic semiconductors that rely on the band transport mechanism. In such a rigid regular or crystalline system, strong coupling between atoms and long-range order ensure the delocalization of the electronics states. The electron-vibration (phonon) interactions are negligible compared to the electronic interactions and results in scattering of the delocalized carriers. However, in organic molecules, weak van der Waals forces effect on the intermolecular interactions. The narrow energy bands can be easily disrupted by disorder arising from the chemical and physical defects in organic materials. Increasing the number of disorders in the system results in more localized states in the band. All the states of the band become localized in the case of vigorous disorder, so charges jump between the localized states across the interacting molecules. Thus, charge transport takes place in the form of hopping mechanism that works for most of OSCs. The energy levels of the hopping sites are assumed to be randomly distributed according to a Gaussian density of states (DOS) width, σ[20]. The weak van der Waals forces create a weak dielectric shielding effect of Coulomb interactions due to randomly oriented polarizations in OSCs. This results in the low dielectric constants, which leads to strong binding energy (0.3-1 eV) between electron and holes [21]. Radiative relaxation of these electron-hole pairs at charge transfer state is the basic principle for light emitting diodes.

2.2 Organic light-emitting diodes

Transparent touch-control screens, bendable phones, roll-up and go monitors, wearable or skin attached displays were only as science-fiction movie gadgets for us and just a dream 40 years ago. Innovations in the last five years, e.g., LG's 65-inch rollable OLED TV[22], transparent and touch-control OLED displays for smart windows[23], Sony's head-mounted wearable 0.23-inch color OLED which performs near-to-eye microdisplay[24] have proved that they are not much of a dream anymore. Research on the skin-adaptable displays is still ongoing at laboratory scale[25]. OLEDs are recognized as the next-generation display and solid state lighting (SSL) technology due to their high display resolution with low power consumptions[2] and efficient high-intensity illumination[26], respectively. High picture quality independent on the viewing angle, fast response time, high contrast ratio, and high color reproduction features make OLED displays superior to LED and LCD.

The first report on EL from an organic material was reported by Pope et al. in 1963[27]. In 1987, Tang and VanSlyke produced the first reasonably efficient light emission from a two-layer OLED structure[8]. Two monomer layers were vacuum deposited in developing a device called a small molecule OLED (SMOLED). After that, OLEDs have drawn intense attention in both scientific and industrial field due to their potential applications in solid-state lighting[28], [29] and flat-panel displays[30]. In 1990, the second breakthrough was the implementation of single layer poly(p-phenylene vinylene), PPV in polymer light-emitting diodes (PLEDs)[30]. While small molecules are usually evaporated, polymers are compatible with solution processing techniques like spin-coating, doctor-blading, etc.

Improvements in the emitting materials used in these devices have also marked several breakthroughs (see section 1.1). The fundamental device physics is similar for different materials whether they are solution processed or vacuum deposited.

2.2.1 Diode characteristics

The most straightforward structure of an organic diode is a thin organic film sandwiched between two electrodes. In principle, OLED converts the electrical energy directly into the light, when the external voltage is applied.

The standard current rectification versus voltage characteristic is created by the difference in work function of the electrodes [31]. Diode refers to the current flow only in one direction under applied forward bias. It has (ideally infinite) resistance when biased in reverse direction as depicted in figure 2.2.

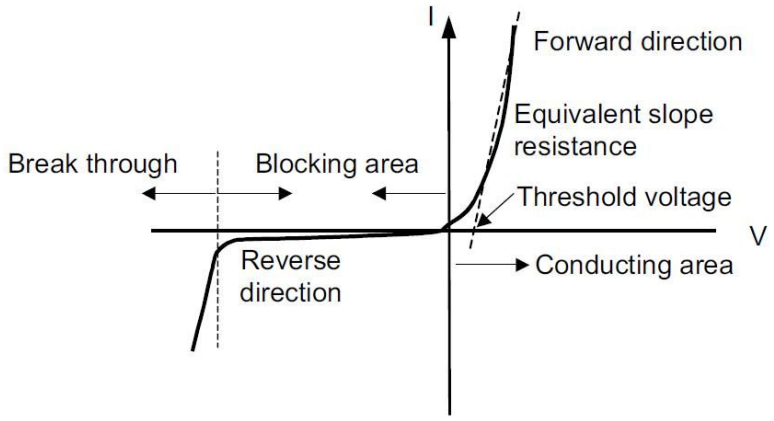

Figure 2.2 Typical current-voltage characteristic of a semiconductor diode.

When forward bias increases, there is a point that diffusion current overcomes drift current which is known as the threshold voltage. After this point, a small increase in voltage leads to an exponential rise in current. If the diode is subjected to reverse bias, a minimal current flows through the device due to low recombination. In excess of applied reverse bias, it breaks down. The forward and reverse I-V characteristics of organic diodes are similar to amorphous silicon p-n junction diodes[32]. However, the p-n junction concept is different with donor-accepter transitions as being the dominant mechanism at the junctions in organics. The device physics of organic rectifying diode will be explained in the following section.

2.2.2 Device operating principles of OLEDs

In an OLED, the light emission results from the radiative relaxation of excited states generated by the recombination of charge carriers[33]. These carriers are injected into the thin film through the electrodes upon applying an external electric field. One of the electrodes has to be transparent for efficient light extraction. The minimum voltage required for the injection is equal to the difference in the work function of electrodes. Ideally, EL should turn on at this threshold voltage (V_t). However, V_t is affected by series resistance arising from the device stack, as well as the energetic disorder and impurities in OSCs.

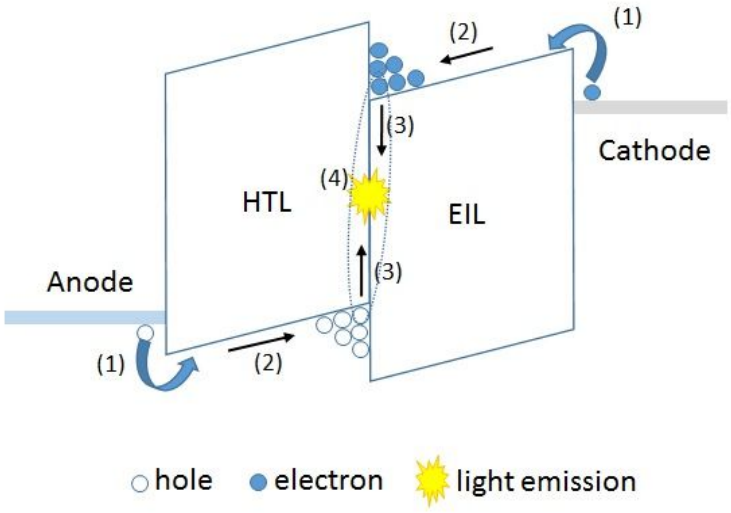

Figure 2.3 A generalized bilayer OLED with organic heterojunction. The schematic energy level diagram illustrating the accumulation of charge carriers at the interface of HTL/ETL.

The device operation is determined by four main steps: Charge carrier injection (1) and transport (2), exciton formation (3) and radiative exciton decay (4) resulting in light emission. All of these processes play a critical role in the device performance, and they will be detailed in the following subsections. Figure 2.3 schematically shows the relevant processes in a bilayer OLED under operation.

2.2.2.1 Charge carrier injection and transport

The charge injection is the first step for diode operation and affects the device performance. We presented a simple bilayer OLED structure and the corresponding energy level diagram in figure 2.3. Electrons are injected into the electron transport layer (ETL) via top metal contact and holes are injected into the hole transport layer (HTL) through the transparent conducting oxide.

The charge carriers are injected by thermionic emission (I) or tunneling (II) mechanisms as shown in figure 2.4a[34]. Injection is dominated by the injection barrier between the Fermi level (E_F) of electrodes and the energy levels of OSC, in which the charge carriers are injected. For the electron injection, the mismatch between the E_F of the electrode and the LUMO of OSCs results in a high rectifying resistance, as named Schottky barrier, Φ_B[35]. The barrier thickness decreases as the applied voltage increases and carriers can tunnel through OSC by Fowler-Nordheim field emission tunneling[33]. Since a strong electric field determines Fowler-Nordheim tunneling, a thin organic layer is required for low operating voltages. Thermionic emission takes place which means that charges are injected over the barrier into OSC if the barriers are small and the temperature is relatively high. An ohmic contact is formed, in the case of the Schottky barrier height is zero or negative[36].

The second step is the charge transport as illustrated in figure 2.4b. The excess of charge carriers (holes and electrons) are produced by further injection. The current through the device is limited by low mobility, resulting in accumulation of carriers near the electrode. This creates a space charge zone which reduces the electric field and limits the current (space-charge-limited current, SCLC). The charge carriers are transported by hopping mechanism (Section 1.1). The migration of charge carriers are field-dependent and affected by the mobility of electrons and holes in ETL, HTL, respectively. Two different SCLCS mechanisms were proposed to describe the charge transport through an organic thin film: (1) the trap-free SCLC[34] with field-dependent carrier mobility and (2) the trap-dependent or trap-limited SCLC[37]. The electron transport is usually considered trap-limited[38]. Bulk transport is dominated by hopping

conduction through an approximate Gaussian DOS in which deep sites act as traps. Electrons can get back its localized site from a trapped position via Poole-Frenkel emission[39]. We illustratively described the energy positions of the trap-free (I) and the trap-dependent (II) transport path in disordered OSCs figure 2.4b.

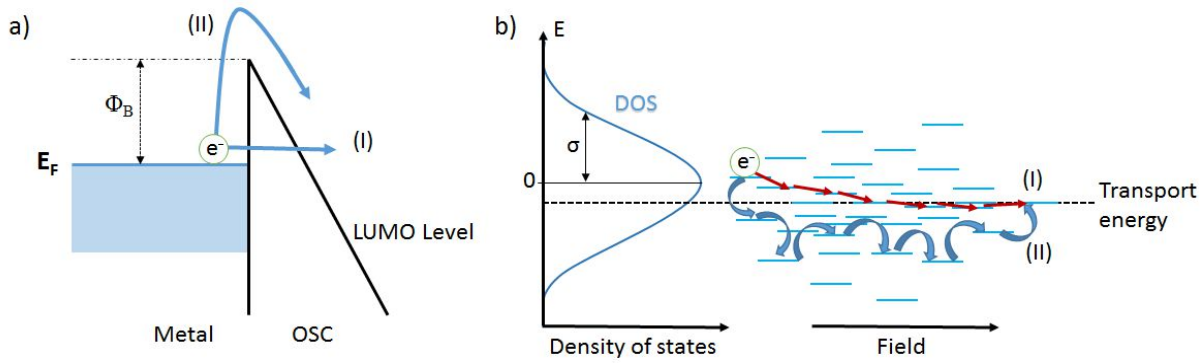

Figure 2.4 a) Schematic energy band diagram of Fowler-Nordheim tunneling (I) and thermionic emission (II) of an electron at the metal/OSC interface. b) Schematic diagram for the density-of-states (DOS) and charge transport mechanism based on free-of-trapping (I) and multiple trapping-and-releasing model (II), σ: DOS width.

The injection-dominated conduction is valid only for the barriers exceeding 0.3-0.4 eV[37]. In this case, charge backflow due to the low carrier mobility. For the lower injection barriers, I-V characteristics depend on bulk-limited transport. Both the injection-dominated (tunneling and thermionic emission) and bulk-dominated mechanism (ohmic and SCLC conduction) are proposed as rate limiting mechanisms for the current density-voltage (J-V) characteristic of OLEDs as explained in section 3.3.1.

2.2.2.2 Exciton formation and radiative exciton decay

In a diode operation, the third step is the exciton formation. At equilibrium, excess charge carriers accumulate at HTL/ETL interface due to the energy level offsets of the heterojunction.

Injected electrons and holes recombine to bound electron-hole pairs (exciton) due to Coulomb attraction when they meet within their Coulomb radius. Excitons with strong binding energy

(0.3-1 eV) localized on one molecule or adjacent molecules[21]. However, Langevin recombination and trap-assisted recombination, i.e., Shockley-Read-Hall (SRH) are present in disordered OSCs with low mobility[40]. In Langevin recombination, free charge carriers drift to each other to recombine. SRH recombination takes place between a trapped and a free charge carrier. The free charge carrier mobility governs both mechanisms.

The final step is the photon generation by a radiative exciton decay after completion of its lifetime period. There are three relaxation mechanisms (Figure 2.5) of the excited states: fluorescence and phosphorescence, and TADF that play a significant role in determining the device efficiency. Localized electron-hole pairs lead a strong electron-hole wave function overlap that induces considerable exchange energy (0.1-1 eV), which separates the singlet and the triplet state energies apart[21]. The relaxation mechanism of singlet and triplet excitons forms the basic principles of fluorescent and phosphorescent light emission.

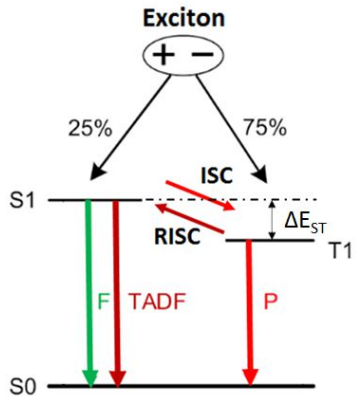

Figure 2.5 Modified Jablonski diagram depicting different transitions for an exciton decay: Fluorescence, phosphorescence and TADF. The ground singlet (S_0), the first excited singlet (S_1), and the first excited triplet (T_1) states.

Based on simple spin statistics, 25% of the formed excitons are singlets (antiparallel spins), and 75% are triplets (parallel spins), resulting in different radiative relaxation processes of fluorescence ($S_1 \rightarrow S_0$), and phosphorescence ($T_1 \rightarrow S_0$), respectively[41]. Fluorescence is formed for most luminescent materials and sets an upper limit to 25% of the internal quantum

efficiency (IQE) of an OLED[42]. Phosphorescent OLEDs (PHOLEDs) with rare-metal complexes were reported in 1998[41]. PHOLEDs enabled almost 100% internal quantum efficiency (IQE) by allowing all excited states recombined [43]. Strong spin-orbit coupling promoted by the heavy atom effect increases the possibility of fast and efficient intersystem crossing (ISC: $S_1 \rightarrow T_1$) and phosphorescence ($T_1 \rightarrow S_0$) at room temperature. In the triplet emitters, all four spin orientations of the excitons can be harvested through a rapid population of T_1 sates [44], [45]. However, their high cost, due to the use of precious metals, limits the applications of phosphorescent materials. In 2012, similar yields were obtained by using the metal-free aromatic molecules which exhibited a thermally activated delayed fluorescence (TADF)[46]. TADF relies on a reverse intersystem crossing (RISC: $T_1 \rightarrow S_1$) by thermal excitation and the delayed fluorescence ($S_1 \rightarrow S_0$) when the energy gap between S_1 and T_1 is sufficiently low (ΔE_{ST}<0.1 eV). Therefore, efficiencies similar to phosphorescence emitters with a maximum 100% IQE can be realized[47].

In most OLEDs, emission generally originates from the radiative decay of excited monomers. On the other hand, electroluminescence may also emerge from the radiative decay of excited state complexes (exciplex) formed between two different materials[48]. The emission refers to exciplex emission showing long wavelengths and a broad spectrum due to energetic conditions (the predicted exciplex energy level being below the exciton)[33]. Exciplex may form at organic heterojunctions of blends in a single layer[49] or bilayer OLEDs[50].

2.2.2.3 Nonradiative exciton decay

In contrast to the radiative decay pathways, the exciton may also recombine nonradiatively via an exciton quenching or phonon emission. The exciton quenching (exciton-exciton or exciton-polaron) occurs near the metallic injecting electrodes, more likely in case of a charge carrier imbalance and low transport properties[51]–[53]. It contributes significantly to a loss in the efficiency of OLEDs. Exciton may also transfer its energy from one molecule (donor) to another molecule (acceptor), forming a new exciton on the acceptor molecule. There are two

mechanisms for the energy transfer: Förster resonance energy transfer, FRET (dipole mediated)[54] and Dexter (electron tunneling mediated) energy transfer[55]. These energy transfers commonly play an active role in the efficiency of the host:guest (i.e., donor-acceptor) type OLEDs[56]–[59].

Phonon emission is another common process in semiconductor devices. Exciton nonradiatively recombines following the energy-gap law defining the rate of nonradiative decay which drops exponentially with increasing the energy gap[60]. For instance, extremely high nonradiative recombination of CT excitons was presented at the heterojunction of two materials with very similar energy levels[61]. So, the device behaved like an ideal ohmic contact, leading a very high rectifying ratio from the electrode/OSC contact. Therefore, the energy level alignment is a critical parameter while designing the device architecture.

2.2.3 Device design principles and state-of-the-art OLEDs

Device engineering focuses on the stability of excitons at the recombination center, besides minimizing losses due to nonradiative exciton decay. An enhancement in the electron-hole recombination results in more photon generation.

The first EL was observed from the monolayer of anthracene crystals at the high voltage of ~400 V [27]. The first practical OLED was operated below 10 V after utilizing two-layer structure resembling a p-n junction[8]. Heterojunction model enhanced the probability of exciton formation and recombination near the interface region. After that, EL was obtained from the single active layer PLEDs via direct charge injection into the polymer, leading a self-localized emitting excited state[30]. Nevertheless, they got low efficiencies as a result of imbalanced charge transport, and recombination processes at an applied bias 14 V. Efficient single layer PLEDs were designed by a different energy level alignment that allows ohmic injection for single carriers[62]. However, this is not always the case to find compatible electrodes for the mismatch between the energy levels of electrode/polymer. Therefore, bilayer PLEDs similar to molecular organic heterojunctions were suggested to increase the device efficiency[50], [63].

Adjusting polymer-polymer energy level offsets improves the charge recombination and brings a sufficient level of device performance.

Subsequently, multilayer OLEDs are designed for proper adjustment of the recombination position by implying different layers to achieve a better charge injection and high-performance OLEDs. Researchers produced multilayer OLEDs[64], and multi-stack OLEDs (tandem) comprising several individual EL units to gain the white light emission[65]–[67]. Today, the state-of-the-art OLEDs contain layers with different functionalities, e.g., hole injection layer (HIL), hole transport layer (HTL), electron blocking layer (EBL), emissive layer (EML), hole blocking layer (HBL), electron transport layer (ETL), and electron injection layer (EIL), etc. (Figure 2.6).

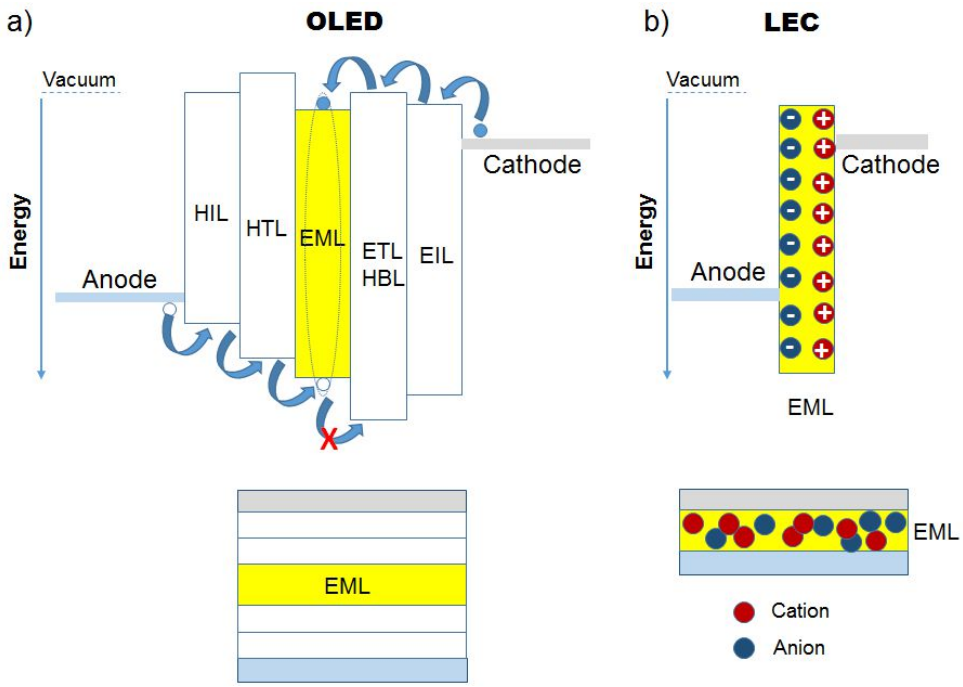

Figure 2.6Schematic illustration of a state-of-the-art OLED (a) and (b) typical LEC. OLEDs require multiple layers that are usually vacuum deposited for high device performance. LECs are usually single active layer devices.

The multilayer structure has some disadvantages. OLED requires a high electrical field to operate as previously explained in section 2.2.2.1. In the multilayer structure, voltage drops across the active region of OLEDs. Therefore, usually, a voltage level exceeding thermodynamic limit is typically required to drive an OLED at high luminance level (e.g., 2.4 eV for green EL)[68]. Scientists fabricated the p-i-n structure OLEDs based on the electrically doped transport layers (p-doped HTL and n-doped ETL) which perform at the low operating voltages[69], [70]. Nevertheless, the thickness of the monolayers has to be optimized, since the total width of the organic layers typically is adjusted to ~100 nm. The layer intermixing is another issue for the fabrication of solution-processed multilayer OLEDs[71]. Additionally, due to a high energy barrier at the cathode/OSC interface, the low work-function metals and alkali metals are vacuum processed for an efficient electron injection[19]. The low-function cathodes give rise to stability problems upon exposure to ambient conditions (oxygen and water). So, the devices are usually hermetically sealed. Different approaches have been made for effective electron injection from the air-stable cathodes[71]. Nevertheless, the encapsulation remains an obstacle in the manufacturing process of OLEDs[7].

2.3 Light-emitting electrochemical cells

OLEDs operate at high electric fields, due to a voltage drop across the active layer[33]. If the film is made more conductive (via electrochemical doping), the charge carriers generate the luminance quenching[72]. In 1994, electrogenerated chemiluminescence (ECL) was demonstrated from poly(5-(2'-ethyl- hexyloxy)-2-methoxy-1,4-phenylene vinylene) (MEH-PPV) film in contact with a liquid electrolyte[73]. ECL cells are not suitable for electronic applications such as displays since lifetime issues prevent commercial applications[74].

In 1995, Pei et al. demonstrated a similar effect from MEH-PPV mixed with a solid polymer electrolyte (SPE) in the single layer of a novel light-emitting device[15]. They sandwiched the polymer blend film between two electrodes. In this manner, the light-emitting electrochemical cell (LEC) was highlighted as an alternative device concept to OLED. Up to date, LECs have been considered as the simplest thin-film lighting device.

SPE providing counter ions is the primary source for the underlying mechanism in these materials and devices. A p-i-n can be formed in situ, due to electrochemical doping provided by ion transport[75], [76]. Thus, they can operate at low turn-on voltages by implying air-stable electrodes as oppose to OLEDs. The turn-on voltage of the cell is almost identical to the band gap of OSCs[77]. Since doped regions have relatively a low resistivity (under bias), symmetric electrodes can be applied. LECs can be fabricated in sandwiched (stacked, i.e., diode-like) or planar configuration[16].

LECs overcome the fabrication complexity of multilayer OLEDs. As compared to the multilayer OLEDs, LECs offers quite simple architecture with a single active layer (Figure 2.6). The emissive layer of LECs can be much thicker than OLEDs that operate according to tunneling barrier distance. For instance, LECs with 1 µm thick active layer were suited for a fault-tolerant fabrication[78]. The device efficiency can also be improved by adjusting the emissive layer thickness[79], [80]. Moreover, their simple structure with high tolerance to thickness variations makes them compatible with printing and coating processing methods[17].

2.3.1 LEC characteristics

Despite the simple device layout, many efforts have been made for understanding the complex device physics of LECs for 15 years[16]. LECs can operate in both reverse and forward bias conditions as a benefit of their dynamic character of mobile ions. I-V characteristics of LECs are antisymmetric (no rectification), regardless of the work-function of the electrodes. As shown in figure 2.7., they can emit light in both forward and reverse regions[15], [81]. They do not block the current in reverse bias, unlike OLEDs.

The device principles of polymer LECs differ from PLEDs. In PLEDs, ionic species are not involved in the device operation. In single layer PLEDs, low conduction through polymer chains and imbalanced charge mobility restrict the device performances as discussed previously in section 2.2.3. Furthermore, the thickness of the active layer affects the operational voltage[82]. When they sandwiched the salt-doped MEH-PPV between the ITO glass and an aluminum (Al)

cathode, it performed like an inefficient PLED, due to work-function of Al[83]. After adding a mixture of salt and ion conducting polymer into the single layer of PLEDs, the electrons could be effectively injected from stable metals such as Al, Ag [84]. They also reduced the driving voltage.

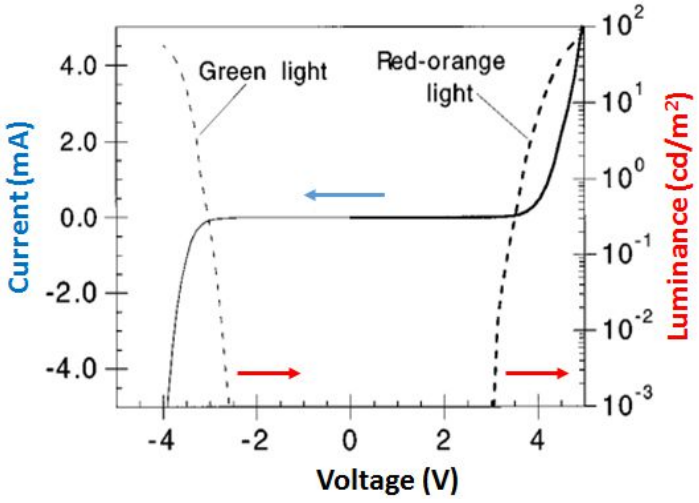

Figure 2.7 Typical current-voltage characteristics of LEC under applied forward and reverse bias. The bilayer LEC emits a red-orange light from MEH-PPV (forward bias) and a green light from PPV layer (reverse bias). Adapted from Ref.[81]. Copyright © 1996 American Institute of Physics

EL in LECs can be produced in a similar way to ECL, yet there are differences. In ECL, a redox-active luminescent film is deposited on a conducting working electrode, which then dipped into liquid electrolyte[73]. Ions are not mixed directly with the film, but existing in the electrolyte solution instead. The film tends to be highly doped by the counter ions, after sweeping the voltage periodically in between the reduction and oxidation potentials of OSC (Small potential window). The light is generated by the electrochemical redox reactions (electron transfer), so the mass transport dominates EL. In LECs, EL occurs via the electron-hole recombination following a charge injection into doped OSC, therewith does not require a mass transport[84]. In other words, there is no charge transfer between the ionic species and polymer. Ions are not directly involved in the light emission.

Different luminescent materials have been utilized for EL; such as conductive polymers (CP)[15], [75], [76], [81], [85]–[89], ionic transition-metal complexes (iTMC)[90]–[96], and so called the third generation materials (e.g., TADF molecules, quantum dots, and luminescent nanoparticles)[97]–[101]. However, the physical processes of device operation are explained under the cover of several studies focusing on CP-based (PLECs) and iTMC-based LECs.

2.3.2 Device operating principles of LECs

The single active layer of LEC is composed of a luminescent material (CP or iTMC) and an ion conducting polymer. The device physics of LEC is complex, due to coexisting of ionic/electronic species in ionically/electrically conductive materials. The unique device physics of LECs stem from ionic species that form the electric double layers.

The mobile ions migrate to the oppositely charged electrodes electrostatically, when a small voltage is applied. Ionic polarization at the interface narrows the injection barriers (Φ_B) and produce charge injection via tunneling.[102] Electrochemically doped interfacial double layers are formed accordingly. Transport of the charges in the layer is diffusive, and the current density of species depends on the charge density and electrostatic potential[16]. Therefore, there is no current flow through the device at a low operating voltage. When the applied voltage is almost identical to the band gap of OSC, a sufficient charge transfer occurs through the double layers. It triggers a rapid increase in the hole and electron densities in OSC. Upon further increase in voltage, the double layers extend through the center of the active layer to form the p-n junction. At the junction, the excess of the holes and electrons recombine to emit light[75].

The exciton formation and decay pathways have been extensively discussed previously in section 2.2.2 for OLEDs. Since the process is also valid in LEC operation, we will only focus on the device operation models and charge injection mechanism of LECs that are assisted by ion and potential distribution.

2.3.2.1 Proposed models for device operation

Alternate mechanisms have been suggested for the detailed device operation of LECs. Figure 2.8 schematically illustrates the two central model systems that are proposed for a coherent understanding of device physics: (1) Electrochemical doping model and (2) and electrodynamic model.

2.3.2.1.1 Electrochemical doping models

Pei et al. suggested the first model, namely the electrochemical doping model (ECDM)[76], which relies on the p-i-n structure in situ formed by electrochemical doping of OSC[95]. As shown in figure 2.8(a), upon injection of holes and electrons, the oxidation and the reduction of OSC takes place at the anode and cathode, respectively. The counter ions electrostatically compensate the oxidized and reduced OSC resulting in p-doped and n-doped regions in the active layer. The doped zones facilitate for efficient charge injection from the electrodes. The metal/OSC interface becomes highly conductive, i.e., ohmic contact, regardless of the considerably high injection barrier in between. After, the injected charges are transported through OSC until they meet at the intrinsic region to recombine. At intrinsic, relatively high electric field and accordingly low conductivity are present due to space charge in the junction. A significant potential decrease is observed in the bulk when there is no potential variance at the interfaces[103]. In the case of ohmic contact at the interfaces, the charge transport in disordered molecules limits the current, so that a bulk-limited, i.e., transport-limited transport dominates the process[104].

However, an injection barrier always resides at the metal/OSC interface, independent of the ion concentration. In the preferential electrochemical doping model (pECDM), only one type doping (either p- or n-type) occurs in the active layer[105]. In this case, charges recombine just close to one of the electrode interface recombine. For instance, the electron transfer rate limits the current density, if the width of the double layer is larger than the electron tunneling distance (for a low salt concentration).

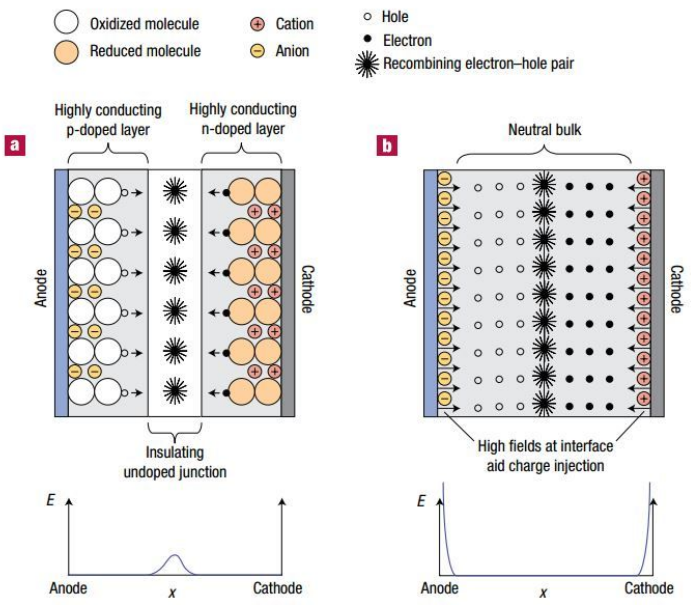

Figure 2.8 Two proposed models for the steady-state operation of LECs with an associated spatial distribution of the electric field underneath: (a) Electrochemical doping model and (b) Electrodynamic model. Reprinted with a permission from Ref.[106]*. Copyright © 2007 Nature Publishing Group*

2.3.2.1.2 Electrodynamic model

The electrodynamic model (EDM) predicts the formation of electric double layers at the interfaces[107]. As shown in figure 2.8(b), under applied bias, anion and cations redistribute at the interface of anode and cathode, respectively. The accumulation of ions at the interface results in a high electric field. Therefore, voltage drops at these interfacial layers, also bulk remains free of the electric field. The electrons and holes diffuse through the field-free bulk where they recombine. The potential reduction mainly locates at the electrode interfaces due to the formation of ionic space charge. Thus, researchers assigned EDM for the relatively poor charge carrier injection[108].

2.3.2.1.3 Unifying model

The unifying model has confirmed in the fact that two models as mentioned above can take place in LEC operation, depending on the injecting behavior at contacts[109], [110]. If there is no ohmic contact, LEC operates according to EDM. In the case of ohmic contacts, LEC follows ECDM. If only one contact is ohmic, the LEC follows pECDM. The unified model is verified for both CP and iTMC-based LECs[105].

However, the preferred operational mechanism of LECs is ECDM which does not limit the charge injection and therewith electrochemical doping of the active layer is not restricted. The electrochemical doping process rules the transients (such as turn-on time and lifetime) and steady-state properties (such as potential and charge distribution, charge recombination) of LECs. Steady-state properties are summarized above in the device operation section.

The transient behavior of LECs such as turn-on time, lifetime, etc., depends on the measurement time and driving conditions[111], [112]. Despite several advantages of LECs, questions concerning the transient behaviour and stability of LECs remain to be addressed. We will focus on them in the next sections.

2.3.3 The role of ion motion and ionic conductivity

The ionic conductivity plays a prominent role on the transients since they are responsible for dynamic properties. The ionic conductivity in the cell is favoured by the solid polymer electrolyte (SPE), i.e., solvent-free polyelectrolyte. Polymer electrolytes are usually composed of salt and polymer matrix, in which the salt ions can dissociate due to permanent dipoles along the chain. The dipoles hold partial negative (δ-) or positive charges (δ+) which can electrostatically interact with cations and anions of the salt, respectively. The counter ions do not integrate with the polymer chain and stay mobile. So, polymer electrolytes are so-called ion-solvating polymers. In first LEC, poly(ethylene oxide) (PEO) and a lithium salt were successfully employed as SPE[15]. The ionic motion of lithium ion in PEO host is illustratively

presented in figure 2.9. As reported in ref. [113], the fundamental mechanism of the ionic conduction is based on a long-range cation transport by the dissociative way, where cations move between polar coordinating sites. They also predicted that ions might form non-labile bonds with polar groups of the host.

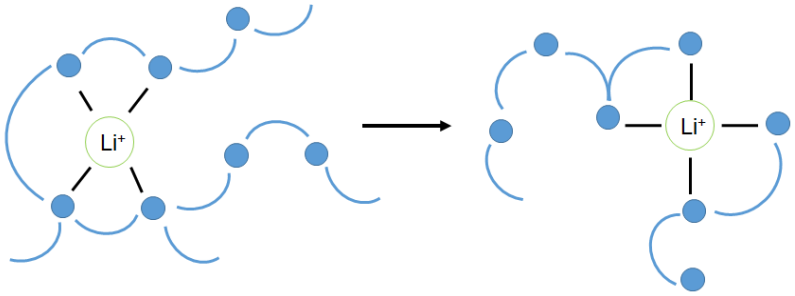

Figure 2.9 Cartoon of the ionic motion of lithium cation in PEO host with partial negative (δ-) oxygen atoms (blue dots). Redrawn from ref.[113]. *Copyright © 1995 Published by Elsevier Ltd.*

LECs have a relatively slow response in terms of turn-on time (T_{on}) in comparison to OLEDs. It is a consequence of the slow ionic movement in a solid-state material with a rapid electronic response[111]. Van Reenen et al. confirmed that T_{on} is strongly dependent on the ion conduction in both CP- and iTMC-based LECs[96]. When they normalized the time-dependent current, luminance, and efficacy, the transients followed a universal shape (see figure 2.10a). Turn-on times have been obtained from several seconds[15] to several hours[114] as a result of multidimensional parameters, besides the active layer thickness, and the applied voltage. Long turn-on times are not convenient for display applications.

Scientists improved T_{on} and the lifetime by utilizing different ion-solvating polymers with enhanced ionic conduction and better salt dissociation[115]–[117]. The concentration of ionic species in polymer electrolytes depends on the dielectric constant of the host polymer and the lattice energy of the salt[118]. The high dielectric constant and low lattice energy give rise to a high carrier concentration. Different ions[93], [119] and ionic liquids[120] have also improved T_{on} since ionic conduction also depends on the ion radius and type.

Additionally, the width of the electrical double layers and the emission zone position can be adjusted by altering the salt concentration[121]. LECs containing larger cations triggered the lower n-doping grade, resulted in more centred emission zone[122]. It exhibits faster doping progression and shorter T_{on}. The current density and light emission can also be improved by increasing the ion concentration [123]. They correlated the current enhancement with the ion distribution narrowing the recombination zone. However, the adverse effects such as electrochemical side reactions and doping-related luminescence quenching limit the process. We will discuss these restrictive factors on device durability in the next section.

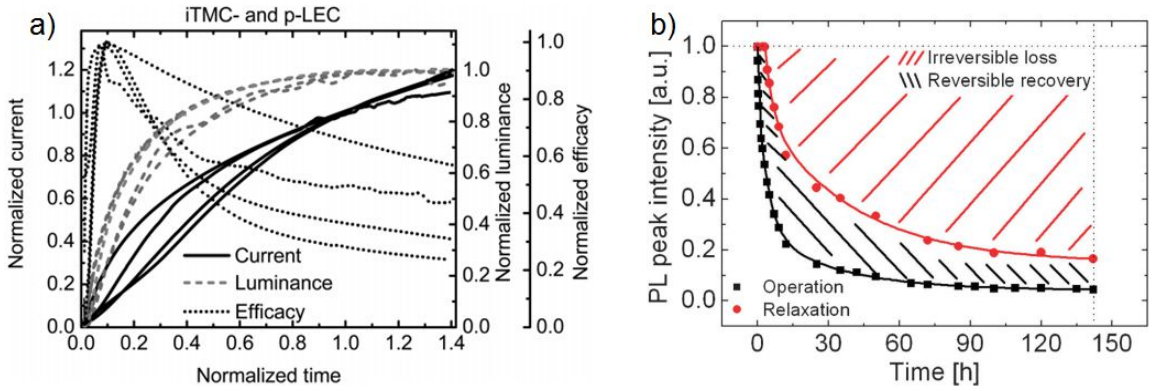

Figure 2.10 Normalized current, luminance, and efficacy transients of iTMC and polymer based LECs (a), reproduced from ref. [96]. Copyright © 2012 American Chemical Society. Reversible and irreversible PL loss of iTMC-LECs (b), reproduced from ref. [124]*. Copyright © 2012 Royal Society of Chemistry.*

2.3.4 Degradation and electrochemical stability

Turn-on and -off states are determinants for the characterization of device stability. The reversible and irreversible processes co-occur as depicted in figure 2.10b[124].

The hysteresis is a typical phenomenon for LECs as a relaxation period of electrochemical doping, due to the slow ion motion. This fact may arise from the reversible or irreversible side reactions during device operation. For instance, EL was reduced by the electrochemical doping after a long-time operation of LECs[112]. Still, they recovered the luminance mostly upon the storage for one or two months (relaxation period). However, the black spots, i.e., loss of

emitting area remained constant as evidence of irreversible reactions during operation. They predicted that the black-spot formation might arise from the chemical deformations at the cathode/polymer interface, due to heavily doping. Slinker et al. proposed that the degradation was a result of the generated emission quencher in iTMC-LEC[125]. They observed a quencher formed by the side reactions at the interface of the cathode, possibly due to moisture or oxygen. However, the exact reason for the formation of black spots generally remains unclear.

Another reason for irreversible reactions is possible side reactions with the polyelectrolyte at the cathode interface. If the reduction level of SPE is below LUMO of CP, electron injection can reduce SPE or CP[126]. Even though charge carrier transport is limited within the insulating polymer, still the effective electron injection may be hindered. In other words, an electrochemical side reaction other than n-doping of CP takes place at the cathode interface and partially limits n-doping. Moreover, a lower p-doping ratio is also detected, when the electrolyte goes under irreversible oxidation before the p-type doping of CP[127]. However, unipolar doping provokes imbalanced charge carriers in the active layer, which then results in the doping-induced micro shorts[128]. Utilizing ion-solvating polymers with more appropriate electrochemical stability windows have improved the lifetime[115]–[117]. The origin of degradation is still not very well understood. Nevertheless, the ion-solvating polymers with large electrochemical stability windows are usually considered as a probable solution for better performance.

2.4 Printed technology for organic electroluminescent devices

Back in 1990, the first PLED was obtained with a spin-casted layer of PPV on indium tin oxide (ITO) coated glass. This pioneering work opened up the possibility of low-cost manufacturing of OLEDs on flexible substrates due to mechanical properties of polymers. Soon afterward, in 1993, the flexible PLEDs on polyaniline coated poly(ethylene terephthalate) (PET) substrate was demonstrated[129]. The first vacuum deposited OLED on a flexible substrate was the preliminary work[130] for fully R2R vacuum processing of flexible OLEDs[131].

Printing and coating are the emerging technology for large-area R2R fabrication, which would dramatically reduce manufacturing costs. In the field of printing and coating, many of the same methods that are common in graphics and the coatings industry which are implemented to OLED technology. In the wide range of printing and coating methods; ink-jet[132], [133], screen printing[134], gravure[135], flexography and slot-die coating[136] have been utilized for OLEDs. For different purposes, layers can be deposited on varying substrates including rigid or flexible surfaces[137], paper[138], [139] and even textiles[140]. Each method has its strength and limitation regarding the requirements for resolution, device architecture, film thickness, etc. Thus, different layers are usually patterned by using a combination of different methods for complete device fabrication. Roll-to-roll manufacturing of PLEDs based on different printing techniques has been recently established[6]. Despite all the efforts including R2R lamination of plastic OLEDs[131], finding low-lost sealant materials or stretchable barrier films (for stretchable devices) are still a problem[7].

In this context, LECs bearing air-stable cathodes have drawn particular attention, since they are suited for wet-based continuous R2R process[17]. Sandström et al. demonstrated the ambient fabrication of flexible large-area LECs using slot-die coating[141]. Owing to a unique feature of planar EL, LECs can be applied on complex-shaped surfaces [142] and textile[143] via spray-sintering method. Fully solution processed PLECs were produced by ink-jet and spin-coating[144].

2.4.1 Comparison of printing techniques and an insight to gravure

We can classify the printing methods by two main factors: throughput and resolution (Figure 2.11). Generally, the resolution becomes a main issue in high-speed printing. However, the gravure can overcome this trade-off. Inkjet is one of the digital printing techniques for effortless patterning of small scale applications and prototyping[132]. Although inkjet is currently the most studied printing method for electronics, it cannot be easily adapted for a wide range of ink viscosities. Non-digital methods such as screen printing, offset, flexography and gravure are preferential for scaled-up high throughput fabrication. Among those, gravure is

the most promising method due to high printing speed and pattern resolution. It's also compatible with a wide range of solvents. Gravure is also capable of printing a relatively wide variety of ink viscosities and thickness variations of layers[145].

Despite the fact that a few examples have been made so far, gravure printed EL devices have the potential to become a major asset in the marketplace since it is a low-cost and continuous method for the mass production.

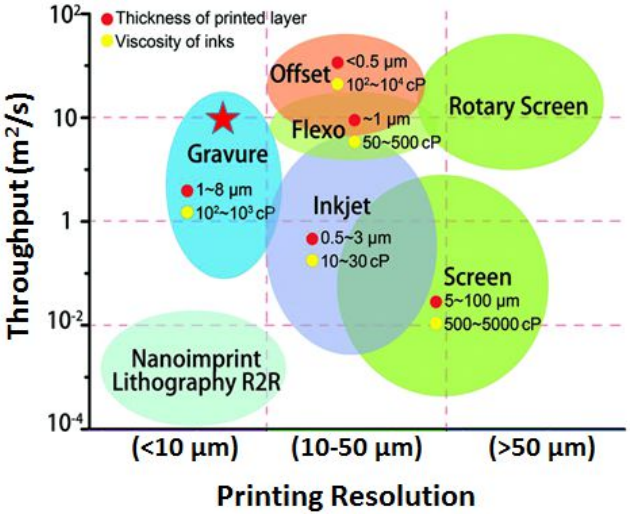

Figure 2.11 Printing resolution and speed for different printing techniques. Printing resolution represents the minimum dot size. Adapted from ref.[145]. *Copyright © 2017 Royal Society of Chemistry*

Chapter 3
Materials and experimental methods

The fabrication and design of the device, as well as the materials from which it is made of play a crucial role in achieving the required performance. Because of the differences in charge injection and working principles, the type of electroluminescent device has a significant effect on the electrical characteristics. The feasibility of solution processing methods for the device fabrication is affected by the physical properties of the material (e.g., viscosity, solubility, film forming) and the device architecture (stack, planar, multilayer).

In this chapter, chemical structures of polymers and polyelectrolytes are illustrated. The fundamentals of experimental methods will be explained for the appropriate understanding of the results. First, the experimental methods for device fabrication and characterization will be summarized. The spectroscopic methods to elucidate charge transfer emission are steady-state spectroscopic techniques such as photoluminescence and electroluminescence will be shown. The electrochemical methods (cyclic voltammetry, impedance spectrometry) will be detailed for extrapolating the data for the stability and ionic conductivity of solid polymer electrolytes. The surface analysis techniques engaged with morphology studies for electrochemical cells will be elaborated.

3.1 Materials

Up to date, so many different materials have been synthesized and tested in electroluminescent devices. Material types (e.g., hole-transport, electron-transport, emitting materials) used in different layers of OLEDs depending on their ionization potentials and electron affinities. In other words, the difference between n-type or p-type material implies the ease of charge injection from electrodes rather than the actual ability for charge transport. For instance, materials with electron-accepting properties (n-type) serve as electron injection and transport layers.

3.1.1 Luminescent materials

Electroluminescence occurs in the active layer of the electroluminescent device. The emitting layer is the recombination center of both electron and holes which then radiatively decay. Therefore, the emissive materials are usually designed in such a way that they can function as both electron-donating and electron-accepting (bipolarity). Organic semiconductors (OSCs) can form in low molecular materials, i.e., small molecules or conjugated polymers. Conjugated systems are explained in section 1.1 in detail.

Conductive polymers (CP) and their derivatives such as poly (para-phenylene vinylene) (PPV)[15], [30], [104], [105], polyfluorene (PFN)[119]), poly-(para-phenylene) (PPP)[81], and poly(3,4-ethylenedioxythiophene):poly(styrenesulfonate) (PEDOT:PSS)[144] have been widely utilized in OLEDs and LECs (Figure 3.1). They can be easily deposited via spin-coating, doctor-blading or printing techniques[6], [131].

The color of devices can be easily tuned by modifying the band gap of polymers via chemical synthesis[146]. New polymers can be designed by changing the repeating units, altering side chains or adding electron donating/accepting moieties. Usually, alkyl chains are attached to the backbone to improve their solubility[147].

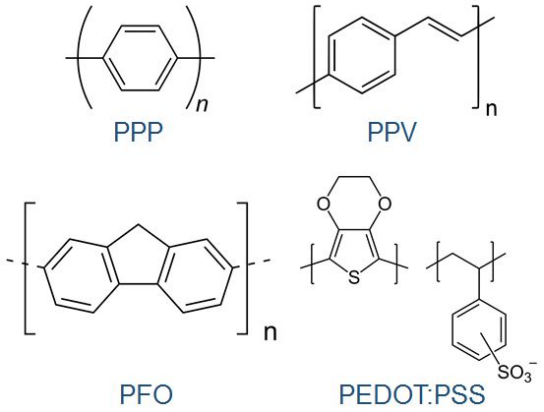

Figure 3.1. General chemical formulas of commonly used conjugated polymers and their abbreviations.

In our work, we utilized PPV and PPP derivatives, as well as a newly synthesized polyfluorene as luminaries. The molecular structures are depicted in figure 3.2. Super Yellow (SY) is a PPV copolymer (commercially sold as PDY-132), which was purchased from Merck KGaA. It can be dissolved in a wide range of organic solvents. In this thesis, it was dissolved in different solvents depending on the device type and processing method. A polyanionic blue emissive polymer, poly(2,5-bis(3-sulfonatopropoxy)-1,4-phenylene, disodium salt-alt-1,4-phenylene), (PPP) was purchased from Sigma Aldrich and dissolved in water to use as the emissive material for DNA based LECs.

PFNCl is an alcohol-soluble polycationic blue-light emitting polymer, that was synthesized via quaternization of *Poly*[2,7-(9,9-bis(2-ethylhexyl)-fluorene)-*alt*-2,7-(9,9-bis(3'-(*N*,*N*-dimethyl amino) propyl) fluorene] with 3,4,5-trimethoxybenzyl chloride by Dr. Martin Petzoldt in the group of Prof. Bunz at Heidelberg University. The synthetic route of PFNCl is exhibited in section 8.1 in the appendix, according to the dissertation of Dr. Petzoldt [148]. It was dissolved in 2-methoxy ethanol to perform as the electron injection layer (EIL) for OLEDs and as the active layer of single component LECs in Chapter 5.

A small molecule (so-called SM-GrünA), a green emissive triplet emitter, was supplied by Merck KGaA and dissolved in toluene or anisole for the printed small molecule based devices in Chapter 4. The chemical structure is confidential.

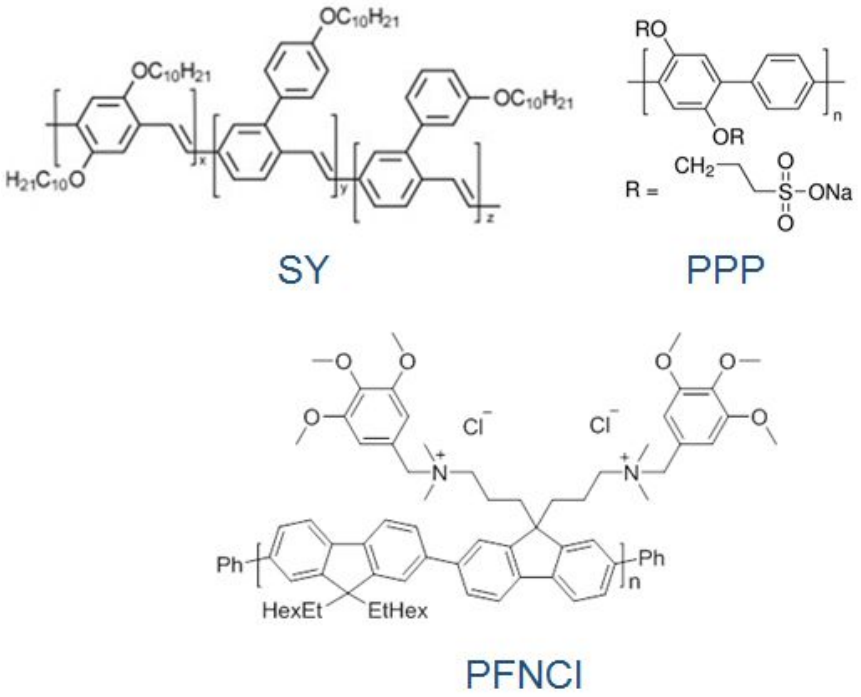

Figure 3.2 The general molecular formula of the Super Yellow [36] and chemical structure of other emissive materials and abbreviations used in thesis. (Ph: Benzyl, EtHex: Ethylhexyl)

3.1.2 Solid polymer electrolytes

The ionic conductivity in LECs is provided by the solid polymer electrolytes (SPE). Different SPE systems have been employed up to date[115]. In the first LEC[15], the ionic conductivity mechanism was based on a polar host polymer (insulator) with polar units and inorganic salt blend (Section 2.3.3). After that, ionic polymers bearing ionic moieties on their chain were designed. So that, polyanions and polycations were associated for the electron injection in polymer OLEDs[149], [150]. Electroluminescent polyanions and polycations were also synthesized and utilized for the single component LECs[119]. In our work, the emissive polymer, PFNCl (Figure 3.2) was also used as an ion-conducting polymer. However, we will mainly focus on the non-emissive polyelectrolytes such as deoxyribonucleic acid (DNA), gelatine, and poly (methyl methacrylate) (PMMA). The details for PMMA will be given in section 3.1.3.

3.1.2.1 Deoxyribonucleic acid and DNA -surfactant complex

In 1953, Rosalind Franklin confirmed the double helix structure of DNA with an x-ray crystallography image*, famously known as Photo 51*[151]. The image led the discovery of DNA structure by Watson and Crick at the same time[152]. Double helix structure consists of base pairs of molecules, namely, adenine with thymine and guanine with cytosine. The base pairs are kept together via strong hydrogen bonds. The helix backbone is made of sugar and phosphate groups. DNA macromolecule is a polyanion due to negatively charged phosphate groups compensated with sodium ions and their counter ions. Furthermore, other molecules/ions can bind to DNA by interacting with phosphate groups electrostatically for sensing applications[153], [154]. The electrical conductivity of DNA is still under debate and related information will be detailed in section 6.2.1.2.1.

In this thesis, DNA and its lipid complex were used as the ion-solvating polymers for LECs. DNA material (DNA sodium salt from salmon testes, Cat. No. D1626) was purchased from Sigma Aldrich and directly used without any further purification step. DNA is a water-soluble material with a molecular mass of 1.3 x 10^6 Da (~2000 bp)[155]. The G-C content of the substance is 41.2%, and melting temperature (T_m) is 87.5°C[156].

The DNA-lipid complex, DNA-hexadecyltrimethylammonium (DNA-CTMA) was prepared by replacing the sodium counter ions of DNA with the cationic amphiphilic lipid (CTMA) according to the procedure in ref.[156]. The process was carried out by Dr. Markus Bender in the group of Prof. Bunz at Heidelberg University. DNA-CTMA is soluble in alcohols and chloroform/alcohol mixture. We dissolved it in chloroform:butanol mixture.

3.1.2.2 Gelatin

Gelatin is a well-known additive commonly used as a stabilizer and thickener in the food industry. In our work, we utilized gelatin as the ion-solvating polymer for LECs. Gelatin from porcine skin with ~300 g bloom (Type A, Cat. No. G2500) was ordered from Sigma Aldrich. It is a mixture of peptides and proteins produced by partial hydrolysis of collagen extracted from the bones, skin,

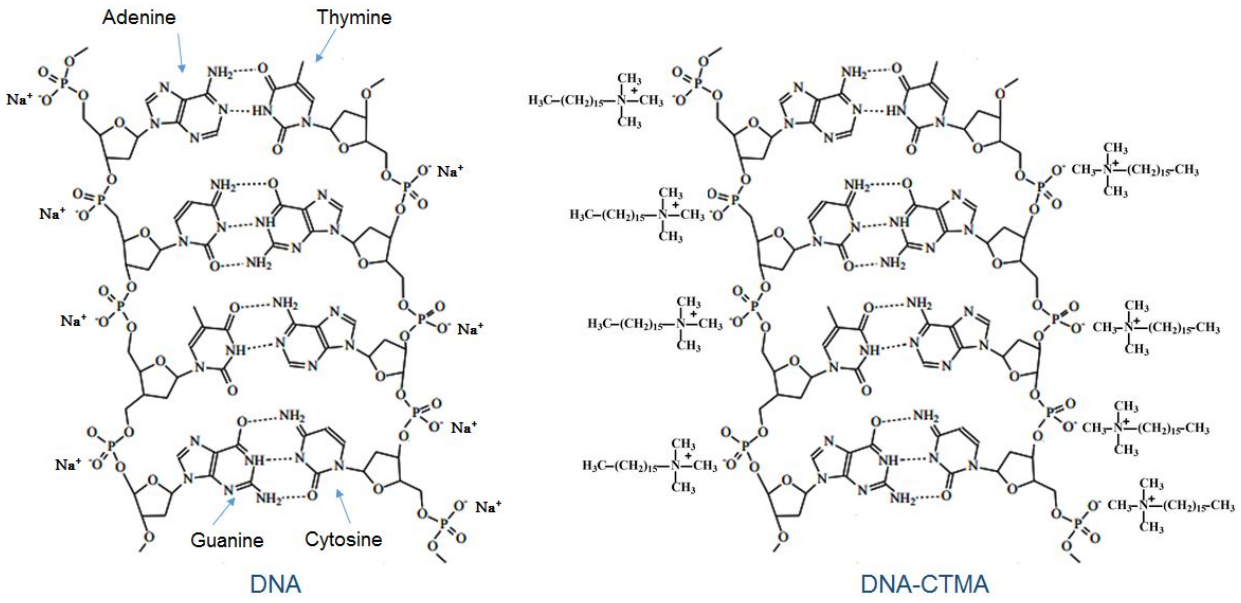

Figure 3.3 Molecular structure of DNA and DNA-CTMA.

and connective tissues of animals. In general, gelatin strand contains main amino acids of alanine (Ala), arginine (Arg), glycine (Gly), glutamine (Glu), 4-hydroxyproline (Hyp), and proline (Pro). The typical amino acid sequence of the type A gelatin chain was reported to be Ala-Gly-Pro-Arg-Gly-Glu-Hyp-Gly-Pro[157]. The bloom number is proportional to the average molecular mass (225-325 bloom = ~ M_w: 50,000–100,000)[158] and indicates the strength of gel formation. The product is soluble in hot than in cold water.

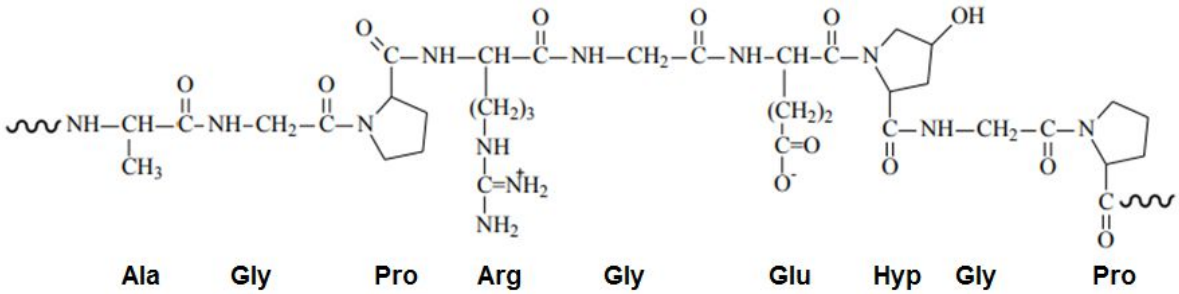

Figure 3.4 Typical molecular structure of gelatin and the abbreviations of amino acid units underneath.

3.1.2.3 Dopants

The organic and inorganic salts were used to improve the conductivity of SPEs. Potassium trifluoromethane sulfonate (KCF_3SO_3) and tetrabuthylammonium tetrafluoroborate ($TBABF_4$) were purchased from Sigma Aldrich. KCF_3SO_3 was dissolved in water, while $TBABF_4$ was dissolved in different organic solvents.

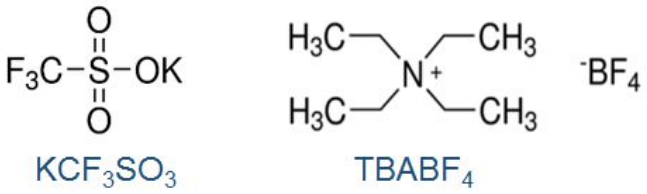

Figure 3.5 Chemical structure of salts utilized to dope solid polymer electrolytes in this thesis.

3.1.3 Binders and plasticizers

The binder and plasticizer are the electrically inert materials, which are usually utilized in solution-processing to change the physical properties such as viscosity[159] and film formation[160].

The functional ink parameters play a critical role in printing processes. The inks are the solution of the functional materials (small molecule and polymer in our study), and their viscosity level should be at a printable range of the printing technique[145]. The binder is added to the small molecule (SM) inks to adjust their rheological properties. In our work, the insulating polymers: polystyrene (PS) with different molecular weights (M_w) and PMMA were utilized as the polymeric host for SM inks to modify the viscosity and surface tension. Additionally, PMMA was accounted as the ion-solvating polymer for the salt additives in SMLECs. Ultra-high molecular weight PS (UHMW-PS) (M_w: ~30 x 10^6) and high molecular weight PS (HMW-PS) (M_w: ~1 x 10^6) were ordered from Polysciences Inc. and Sigma Aldrich, respectively. We dissolved them in toluene and anisole. PMMA (M_w: ~2 x 10^6) was purchased from Sigma Aldrich and dissolved in anisole.

Plasticizers were used to improve the mechanical properties of the biopolymers, as well as to enhance the ionic conductivity of bio-based SPEs. Glutaraldehyde and glycerin (i.e., glycerol) were purchased from Sigma Aldrich and used as the cross-linker agent for gelatin solutions. They are both water-soluble.

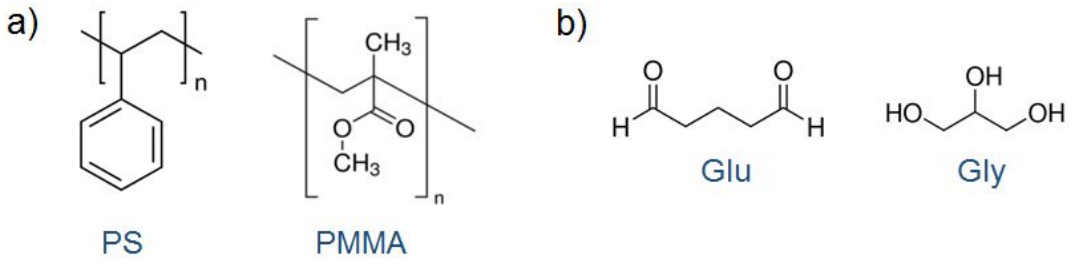

Figure 3.6 The chemical structure of insulating polymer hosts (a) and plasticizers (b) with their abbreviations used in thesis. Glu: Glutaraldehyde, Gly=Glycerol.

3.2 Device fabrication methods

The principle difference between polymeric and molecular materials is the method applied for the deposition of their thin films. Small molecules are usually fabricated layer by layer in a high-vacuum environment, while polymers are coated by wet-processing. In this thesis, we applied the solution processing techniques for both material types.

We fabricated multilayer device structures consisting of different organic layers. The bilayer device structure was composed of HTL and ETL to grant more balanced charge injection in SMLEDs. For color-tunable PLEDs, the device architecture was comprised of three layers: HTL, EML, and EIL. There are two LEC architectures are used in literature: stacked or diode-type, and planar[16]. In this thesis, we used the stack architecture, since the geometry of planar is not convenient for practical applications. Single layer and single component LECs were produced.

3.2.1 General device fabrication

Electroluminescent devices were fabricated on 2.5x2.5 cm substrates for the current-voltage-luminescence measurements and further electrical measurements. 120 nm thick ITO coated glass (0.7mm) with a sheet resistance value of 10 Ω/sq and 120 µm thick polyethylene terephthalate (PET) with a sheet resistivity of 50 Ω/sq were used as the transparent electrodes. ITO patterning was managed by acid wet etched by HCl (32%).

ITO was cleaned by ultrasonic treatment with acetone and isopropyl alcohol. Afterward, they were dried with nitrogen flush and treated by oxygen plasma for 10 min. A PEDOT: PSS (Al4083, Heraeus) solution diluted in isopropanol was either spin-casted or printed onto clean substrates to perform as HTL for all the device types. The spin-casted PEDOT: PSS layer was annealed for 15 min at 120°C to give 40-60 nm thick film (using different spin-rates). The gravure printed PEDOT:PSS was dried at 120°C for 1 h, resulting in thicknesses between 140 and 160 nm. In this thesis, all the thicknesses were determined with a Veeco Dektak 150 surface profilometer.

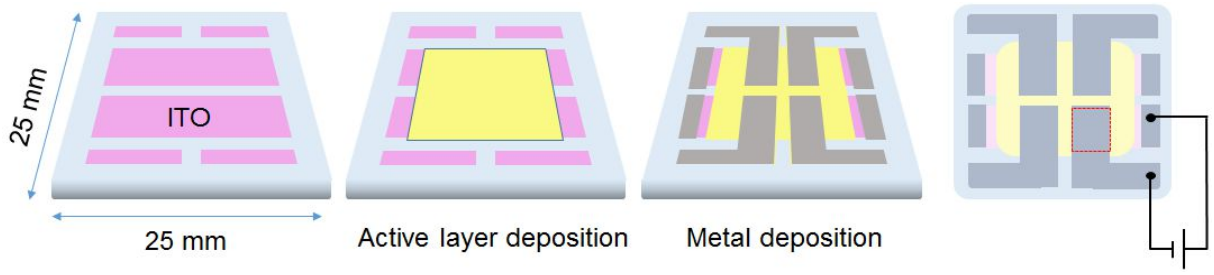

Figure 3.7 Device fabrication on ITO coated glass substrate, resulting in four pixels of 6 X 4 mm size (top view of the completed device, right image). Device structure is same for ITO coated PET substrates.

After the deposition of PEDOT: PSS, other organic layers were deposited by either spin-coating or gravure printing on HTL. Active layer solutions are prepared either in a N_2 glovebox or ambient atmosphere depending on the material type. Various polymer:polymer, small molecule:polymer blends were engaged at the different weight to weight (w/w) ratios and

concentrations depending on the ink formulation and the device type. The solutions were stirred on a hotplate overnight below the solvent boiling point.

For printed devices in section 4.2.1 and 4.2.2, SM:UHMW-PS blends at 20:3 and 20:4 w/w ratios were dissolved in toluene and anisole, giving a total solid concentration of 23.0 g/L and 24 g/L, respectively. As reference devices, pristine SM (20 g/L in anisole) and two SM:UHMW-PS blends were deposited by spin-coating, yielding thicknesses at 60 and ~120 nm, respectively. SM:UHMW-PS blends were also printed, resulting thicknesses ranged between 132-162 nm. The thickness of PEDOT:PSS layer was 60 nm. *For the printed SMLECs:* SM:PMMA:$TBABF_4$ at a w/w ratio of 10:1:0.2 with the concentration of ~22.4 g/L was deposited from anisole and resulted in the film thicknesses at 70-90 nm.

For polymer OLEDs in section 5.2.2 and 5.2.3, we prepared 5 g/L of Super Yellow (SY) of and 10 g/L of PFNCl solutions in toluene and 2-methoxy ethanol, respectively. The PFNCl solution was filtered through a 0.45 µm PTFE filter. A *single layer of PFNCl LEC* (65 nm) was spin cast on ITO glass or PEDOT:PSS covered ITO glass for the single component LECs. For *the hybrid device*, SY (50 nm) was coated on PEDOT:PSS layer. PFNCl was coated on top of SY layer by spin-coating using different spin-rates yielding thicknesses between 55-80 nm. The thickness of PEDOT:PSS layer was 40 nm.

For Bio-LECs in section 6.2.1, *DNA* and *PPP* were dissolved in water for several hours and then mixed at a ratio of 5:1:0.1 (PPP:DNA:KCF_3SO_3), resulting in a total solid concentration of 20 g/L. The ~95 nm thick films were dried on a hotplate at 55°C for 15 minutes in ambient air. *Gelatin* (7.5 and 15 g/L) was dispersed in water and then was heated over 35°C on a hotplate for several hours to dissolve. It was subsequently mixed with PPP solution at the w/w ratio of 1:1 and 1:2 (gelatin:PPP). KCF_3SO_3 and glycerin were added to improve the ionic conductivity. The layers were deposited from hot solution and then dried at 35°C for 24 hours to remove residual water. The active layer of LEC was composed of gelatin:PPP:KCF_3SO_3 with and without additional plasticizer. The thicknesses ranged between 45 and 130 nm. ***For DNA-CTMA based LECs*** in section 6.2.2, *SY*, *DNA-CTMA* and *$TBABF_4$* were dissolved separately in chloroform:butanol ($CHCl_3$:BuOH) mixture (2:1) and then mixed with w/w ratio of 5:1:X (X

describes various salt ratio in the blend) with a total solid concentration of 2.5 g/L. DNA-CTMA solution was filtered through a 0.45 µm pore sized PTFE filter to remove residual particles after the modification process. All solutions were mixed at varying w/w ratios with different total solid concentrations. Solutions were spin-casted on ITO glass, forming film thicknesses at the range of 70-75 nm. ***For reference SY LECs***, *SY* was dissolved with a concentration of 4 g/L in chloroform and mixed with $TBABF_4$ at varying w/w salt ratios (5:X). The active layers of LECs were spin-casted to give ~90 nm thick films.

All the active layers were deposited in ambient conditions and dried on a hotplate for 10-15 min. Only the printed layers on PET substrates were dried for several hours in vacuum. The principles of wet-processing techniques are explained in the following subsections.

As the final step, a silver Ag (100 nm) top electrode was evaporated onto the active layers through a mask in the vacuum (pressure < 10^{-6} mbar) for LECs and hybrid device architecture. Only for DNA-LECs, an aluminum Al (100 nm) was employed as the cathode. A calcium/silver Ca/Ag (~10/100 nm) electrode was deposited for the printed SMOLEDs. The overall electrode area was 6 X 4 mm (0.24 cm^2). An epoxy barrier foil supplied by 3 M adhered on top of printed SMOLEDs and DNA-LECs.

3.2.1.1 Spin-coating and doctor-blade technique

Spin-coating is very well established and commonly used solution processing technique for film deposition (Figure 3.8a). For the spin-on method, the substrate is mounted onto a rotating chuck. A drop of solution containing a dissolved material is placed onto the substrate. The rotating substrate with centripetal force spreading the drop radially results in forming a wet film of the material. Subsequent baking of the substrate helps to remove excess of solvent, leaving a thin uniform film (~ 100 nm). Since polymers are cast from solution subsequently for multilayer device structures, solvents used for the second layer should not dissolve the underlying polymer film.

Doctor-blade (figure 3.8b) is one of the widely used coating technique in forming large-area thin films. In this process, the solution is placed on a substrate along the blade. When a permanent

relative move sweeps the blade, the solution spreads on the substrate to form a thin sheet of liquid. It gives a thin-film upon drying.

For the printing tests, 175-µm-thick polyethylene terephthalate (PET) substrates were covered with (PEDOT:PSS, Clevios) with the help of a Zehnter ZAA 2300 film applicator.

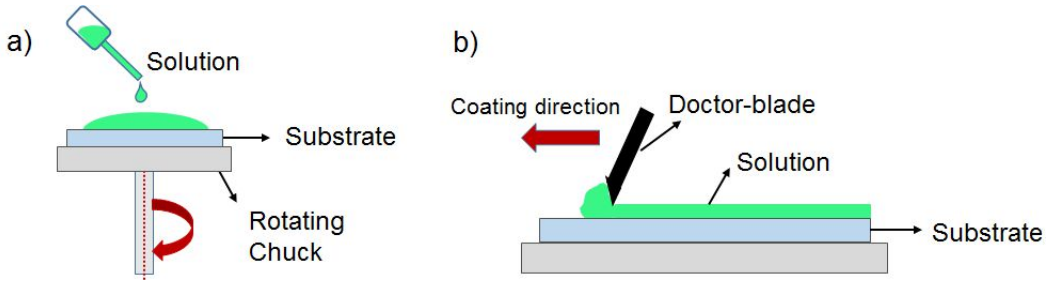

Figure 3.8 Schematic illustration for spin-coating (a) and doctor-blade (b).

3.2.1.2 Gravure printing technique

The gravure printing process allows uniform continuous film forming for large areas in a single printing step. It grants high resolution at high printing speeds[145]. The different ink formulations were printed using a RK gravure printing proofer at a speed of ~ 1 m/s (Figure 3.9a). RK gravure printing proofer is generally used for small scale patterning as a proof-of-concept and producing prototypes. Comparing to the sheet-fed gravure systems, it does not consume a large amount of ink volume (Fluid volume: ca. 1 ml). Thus, the instrument is quite advantageous for setting the process parameters and modifying the ink formulations by consuming less material.

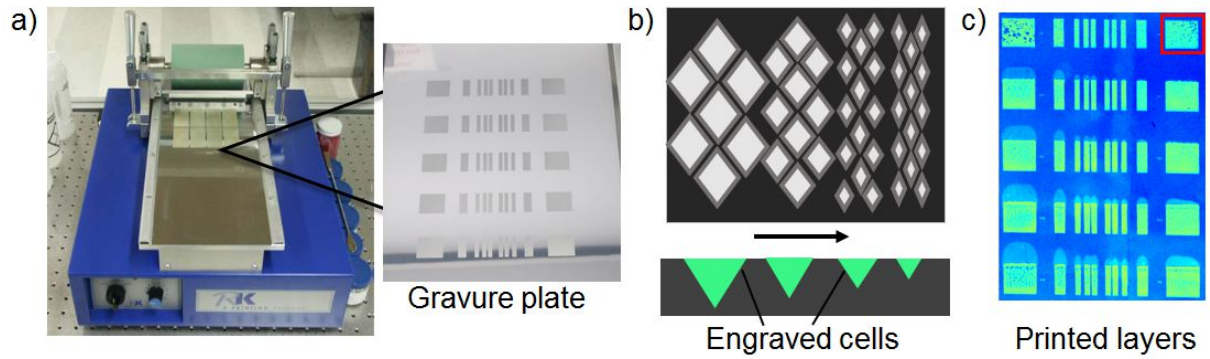

Figure 3.9 RK gravure printing proofer and the printing plate (a) Copyright @ InnovationLab GmbH. Illustration of lateral and top view of engraved cells differ in area and volume (b). The arrow indicates the increase in lines per cm (ln/cm) on the gravure plate. The photograph of printed fields with the size of 14 x 16 mm (c).

The engraved cells may form in variable depth and variable area, defining the overall ink transfer volume (Figure 3.9b). The ink transfer volumes directly affect the film thickness. We used different engraved plates having different cell geometry parameters to ensure a thin, continuous film of SM ink. *For SMOLEDs*, we used the gravure plate with the cell volume per area of 14 ml/m and 54 lines per cm (ln/cm). *For SMLECs***,** four gravure plates with different cell geometry parameters (60/54 ln/cm, 80/70 ln/cm and 100 ln/cm with 90% and 100% tone values) were implemented.

3.2.1.2.1 Process principles

The plate to roll gravure printing system based on ink transfer from an engraved plate to the substrate that is wrapped on a roll (Figure 3.10a). The flexible PET substrate is mounted onto the rotating printing cylinder moving on an engraved gravure plate. Gravure cell dimensions on the µm scale. A direct gravure printing process can be controlled in three main steps: a) gravure cell filling, b) ink transfer, and c) film drying.

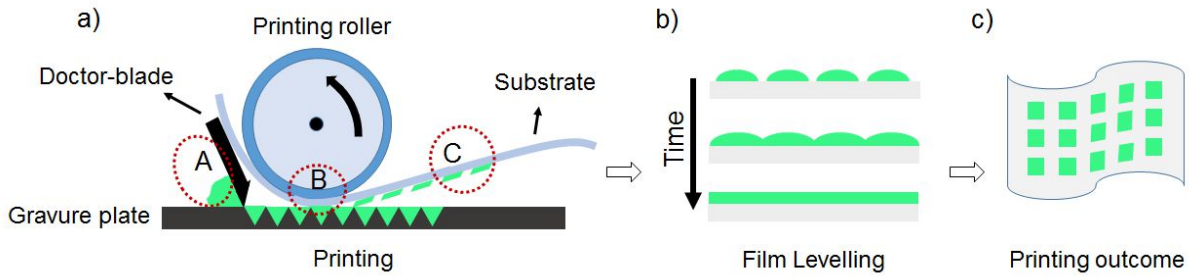

Figure 3.10 A sketch of the plate to roll gravure printing process (a). Illustrative description of dry continuous film forming by levelling (b) and printed patterns on PET substrate (c).

The first step is filling the engraved cells on the gravure plate with the functional ink. The excess ink is simultaneously removed by a blade mounted on the printing cylinder (A). The rheological behavior of ink at high shear rates affects the cell filling. Subsequently, the ink is transferred onto the substrate from filled cells (B). The step requires good wetting properties of the fluid on the substrate. De-wetting is the primary reason for hydrodynamic instabilities that cause film demodulation in the next step. The final step is drying of the transferred wet film (C). Due to the hydrodynamic instabilities (Figure 3.10b), the wet film usually presents inhomogeneous thicknesses arising from which form in a striped pattern along the printing direction, so-called viscous fingering[159]. The printing parameters, as well as the fluid properties, dominate the final stage.

3.2.1.2.2 Ink formulation (Rheometry)

The quality of printed layers is strongly influenced by the ink properties, such as surface tension and viscosity that should be at a printable range of the printing technique.

One of the most crucial ink properties is viscosity, which is solely defined by the fluid's resistance to flow. The ink viscosity dominates the gravure cell filling and the hydrodynamic processes. In our work, the shear viscosity of inks was measured at 23°C using 1 mL sample volume with Haake Mars rotational rheometer based on the cone-plate type rheometric technique. In this method, the fluid is replaced on a stationary flat plate, and a cone plate rotates on the sample. The angle between the surface and the cone is 1 degree (in our setup).

The cone plate rotates, and the torque on the cone is measured. A constant shear rate is applied throughout the sample and viscosity (η) is calculated using formulas below[161],

$$\text{Shear stress (dyne/cm}^2) = \frac{\tau}{\frac{2}{3}\pi r^3}$$

$$\text{Shear rate } (sec^{-1}) = \frac{\omega}{\sin\theta}$$

$$\eta\ (\text{mPa s}) = \frac{Shear\ stress\ x\ 100}{Shear\ rate}$$

,where τ: % full scale torque (dyne x cm), r: cone radius (cm), ω: cone speed (rad/sec), and θ: cone angle. The temperature is stabilized by controlling the plate temperature.

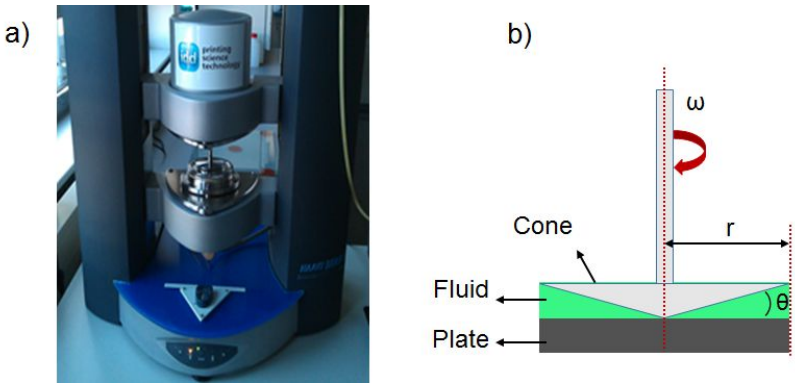

Figure 3.11 Haake Mars rotational rheometer (a) Copyright @ InnovationLab GmbH. A cross-sectional view of the cone and plate rheometer (b).

3.3 Device characterization methods

3.3.1 Optical and electrical characterization

Optoelectrical characterization is the first parameter to discuss for the electroluminescent device performance. The current-voltage (J-V) characteristic helps to understand the charge

injection and charge transport mechanism within the device, while the luminance-voltage (L-V) gives a measure of the brightness.

The current density-voltage-luminance (J-V-L) characteristic was measured using a BOTEST measuring system (Figure 3.12) composed of a source measure unit (SMU) as substrate holder which supplies the voltage and a photodiode cover that shields the ambient light while detecting light emission from the device. The system was controlled by software that allows simultaneous measurement of J-V-L characteristics. The photometry technique was used to measure the forward viewing luminance at the surface of the device. The system was calibrated for the wavelength-dependence to the sensitivity of the human eye.

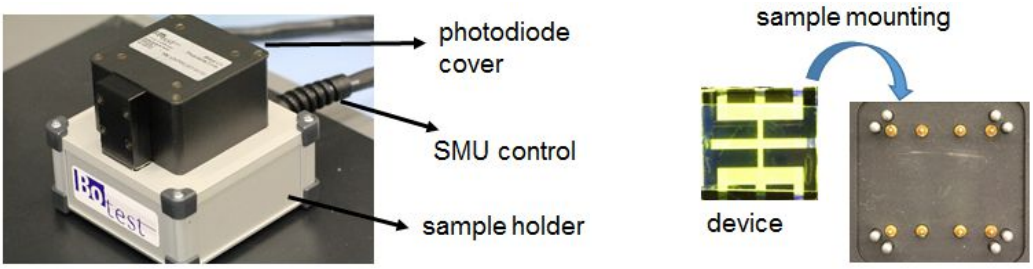

Figure 3.12 LIV BOTEST system, the substrate holder with electrical connections and the photodetector. Copyright @ InnovationLab GmbH.

3.3.1.1 Current-voltage characteristic of OLED

Figure 3.13a shows three main regimes of typical J-V characteristic of an OLED under applied bias: (I) the low-field ohmic conduction, (II) the space-charge-limited current (SCLC) in the presence of shallow traps, and (III) the trap free SCLC. The electrodes are selected in such a way that allows the charge injection preferably at low voltages. At the low electric field, the current density *J* remains almost constant at zero value with an applied bias *V*. In the presence of traps, the carriers can be trapped due to the energetic disorder or impurities. In this case, a portion of carriers is necessary to fill all the traps, and the remaining carriers can have a trap-free transport. In other words, a fraction of the carriers is used to populate the traps, which allows other carriers to be more mobile. After that, the device exhibits a linear regime, where the

transport is injection-limited, followed by exponential increase within a short range of applied bias. Finally, the free-trap conduction region is attained, where the number of injected charges reaches a maximum since their electrostatic potential prevents further charge injection. The maximum luminance and the turn-on voltage (V_{on}) characteristics are shown in the figure 3.13a.

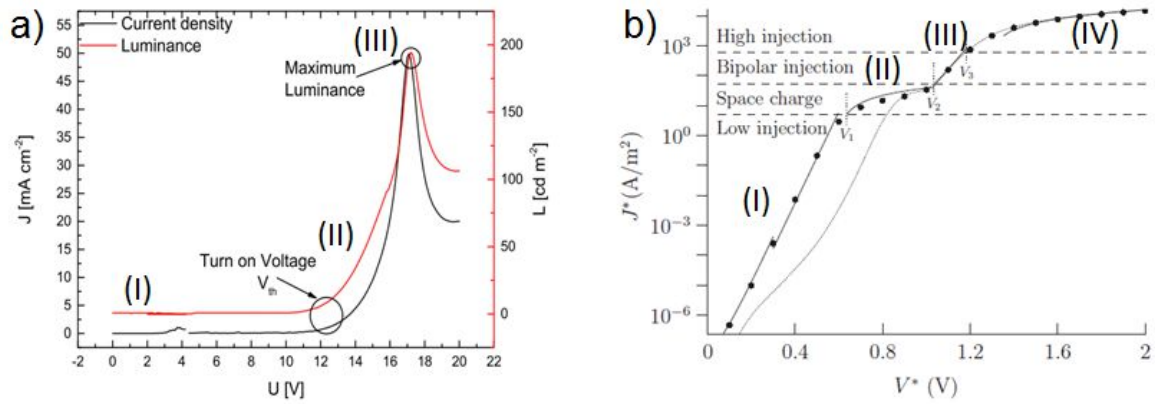

Figure 3.13. A typical J-V-L characteristic of an OLED measured by the BOTEST system (a). The current density (black curve) and luminance (red curve) are plotted vs voltage. A numerical model for J-V characteristic of LEC by Mills and Lonergan (b), adapted from ref. [102]*. Copyright © 2012 American Physical Society.*

3.3.1.2 Current-voltage characteristic of LEC

J-V characteristic of LECs is quite complicated due to the fact that it is affected by the driving conditions and side reactions[111], [112]. Mills and Lonergan proposed a numerical and analytical model for the bulk-limited transport in the low mobility and mixed ionic-electronic conduction systems[102]. Their model is valid for the description of device behavior of LECs, in which the electronic carrier mobility is generally low. The J-V behavior is divided into four distinct regimes to describe the transport-limited conduction of LECs (Figure 3.13b). The first regime is the low injection regime, which is dominated by the ionic species. Due to electric double layers (EDLs) that may start to form, the current intensity *J* increases exponentially by injected charges. The field-free bulk grants diffusive transport that follows EDM (see section 2.3.2.1.1). The second regime is the space-charge regime, which corresponds unipolar charge

injection related to pECDM. The space-charge of majority carrier restricts the further dosing, so *J* does not increase much. Increasing the voltage gives rise in the injection of minority carriers. The third region is the bipolar injection regime. *J* rises rapidly as a result of an efficient hole and electron injection. Therefore, by following ECDM (see section 2.3.2.1.2), EDLs extend through the center of the device. The bulk transport is a combination of drift and diffusion. The fourth region can be observed when the electronic carrier densities catch up the ionic densities. Once the intrinsic region is formed, the voltage enhancement does not assist any further doping of the layers, but only results in a weaker increase of *J*.

3.3.2 Figures of merit for device performance

The following figure of merits typically describes the optical property of electroluminescent devices:

The luminous intensity *(luminance)* is defined as the intensity of emission per unit area (candelas/m^2) from the emitting surface [33]. ***Turn-on voltage*** (V_{on}) is an essential parameter for device characterization. It is here defined as the applied voltage at the certain brightness with a minimum threshold level (specified 1 cd/m^2 in this thesis). ***Turn-on time*** (T_{on}) is defined by the time between switch-on of the cell by an applied voltage and the time which luminance reaches a predefined level (specified 1 cd/m^2 in this thesis).

The electroluminescence efficiency is given by either lm/W (power efficiency) or cd/A (efficacy), where 1 lm= 1 cd·sr [16]. The EL efficiency corresponds to the conversion efficiency of the electronic charge carriers into photons and corrected by the sensitivity of the curve of a human eye. In power efficiency (lm/W), voltage is also taken into account.

The internal quantum efficiency (IQE) of the devices can be estimated from the ratio of light generated within the device to light detected by the photodetector[33]. IQE is represented by η_{int} for the fluorescent materials and given by:

$$\eta_{int} = \gamma \cdot \eta_s \cdot \Phi_f$$

where γ: charge-balance factor, η_s: singlet exciton efficiency, and Φ_f: the fluorescence quantum efficiency. Due to spin statistics, the maximum theoretical IQE of 25% and 100% can be reached for the fluorescent and phosphorescent OLEDs, respectively[41], [43].

The external quantum efficiency (EQE) is stated as the ratio of the number of emitted photons outside the device to the number of charges injected into the device[33]. The device efficiency of an OLED can be determined by the external quantum efficiency (EQE), (η_{ext}), and can be described by the following equation:

$$\eta_{ext} = \eta_{int} \cdot \eta_p = \gamma \cdot \eta_r \cdot \Phi_p \cdot \eta_p$$

where γ, η_r, Φ_p, η_p are charge-balance factor, recombination efficiency, the fraction of radiative exciton decay (photoluminescence quantum yield), device out-coupling efficiency, respectively. Considering the light out-coupling efficiency of 20%, the classical estimate for the maximum EQE for a fluorescent OLED is only 25% of 20% = 5%. Today, TADF OLEDs have reached the maximum EQE at the range of 30% without optical out-coupling method and %40 by using an out-coupling sheet[47].

Color coordinates are designed by the Commission Internationale de l'Eclairage (CIE) in 1931 to compare the color of emission in a standardized manner[16]. Any color can be ascribed by the color coordinates *X, Y* on the CIE chromaticity diagram. All the colors in the visible spectrum exist within or on the boundary of the chart. The Planckian locus resides near the center of the graph. This curve is the plot for the coordinates of black body radiation at the temperature ranging from 1000 K to 20000 K, which is described as ***correlated*** **color** ***temperature*** (CCT).

CCT is a significant parameter for white emission OLEDs (WOLEDs). If the *x, y* coordinates are not on the blackbody locus, the color of the light is characterized according to CCT. It correlates to the temperature of a blackbody radiator which has a color that closely matches with the emission of a non-blackbody illuminator. For a high-quality white light, CCT should be between 2500K and 6500 K. For general illumination, the color coordinates (*x, y*) should be close to 0.33, 0.33.

Color rendering index (CRI) is used to quantify how different the colors appear under illumination of a light source, compared to when they are illuminated by standard illuminator with the same correlated color temperature. It is determined in 0-100 scales, and the highest CRI can be 100 if there is no difference in color rendering. A good quality white light generally requires a minimum CRI of 80.

The lifetime ($T_{1/2}$) is stated as the time for the luminance decay to its half-maximum.

3.3.3 Steady-state spectroscopy

The steady-state defines the condition of a process that does not change in time. The optical characterization of organic materials is the basis for their application in optoelectronic devices. Absorbance or transmittance, and photoluminescence properties of the emissive materials were investigated by implementing the absorption and steady-state fluorescence spectroscopy techniques. Additionally, the fluorescence microscopy was used as a surface imaging technique.

3.3.3.1 Absorption spectroscopy

The theoretical background of the technique is described by the Beer-Lambert-Law[162]. The absorbance is determined the intensity of light; I_t has passed through a sample and I_0 is the intensity of the incident light.

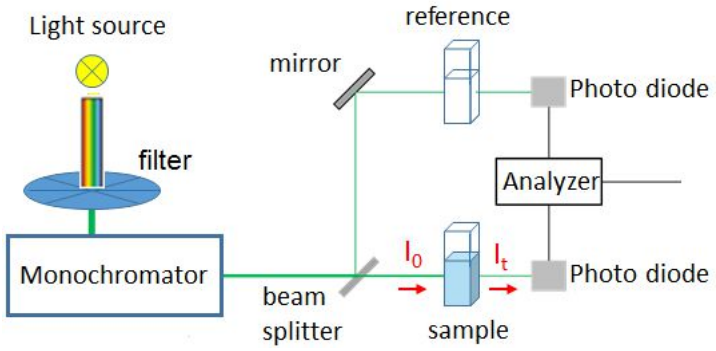

Figure 3.14 A simple sketch of UV-Vis spectrometer setup. Light passes through a specimen and transmitted light is detected by a photodetector. L is the light path in the cuvette.

The transmittance (*T*) and absorbance (*A*) of the sample can be calculated by the following equations:

$$T = I_t/I_0 \ = 10^{-\varepsilon cL} \ = 10^{-OD}$$

$$A = log_{10} \ (I_0/I_t) = \ \varepsilon cL = OD$$

, where ε is molar absorptivity, *L* is the length of the light path which is the diameter of a cuvette, and *c* is sample concentration (for solutions). When *A* is measured through a thin film of the material, it equals the optical density (OD). If the film consists of *x* stacks, the *OD* can be written as:

$$OD = \sum_{j=1}^{x} \varepsilon_j \cdot d_j$$

, where ε_j is the absorptivity of the film with a thickness of d_j. Absorption changes with an increase in the film thickness as an indication of packing of the molecules. The absorption spectroscopy measurements were carried out on a JASCO UV-VIS V-660 or JASCO UV-VIS V-670 either in solution or on a thin film of the materials. The spectrophotometers had a deuterium/halogen source with the wavelength range of 200-2500 nm.

3.3.3.2 Photoluminescence spectroscopy

Steady-state fluorescence spectroscopy is a contactless and non-destructive method to define the electronic transitions of materials. Photoluminescence (PL) is realized by a photon absorption of organic material, in which an electron is excited from its ground state (S_0) to a singlet excited states (Figure 3.15a). The relaxation mechanism follows an electron relaxation from the first singlet excited state (S_1) or the triplet excited state (T_1) to S_0 by emitting a photon. As a consequence of vibrational relaxation (IC) of the excited states, a red-shift is always observed between emission and absorption spectra, namely *Stokes' shift*[162].

The measurement setup shown in figure 3.15b is similar to the absorption setup unit. However, the detector is usually placed at 90° to the incident light to eliminate the risk of transmitted or reflected light reaching it. In a typical emission measurement, the excitation wavelength is selected by a monochromator, and detection wavelength varies. The excitation light coming from monochromator passes the sample. The sample absorbs a proportion of the incident light. The emitted light is collected through a second filter and reaches to the detector. In our work, we conducted PL measurements with a JASCO FP-6500 spectrometer.

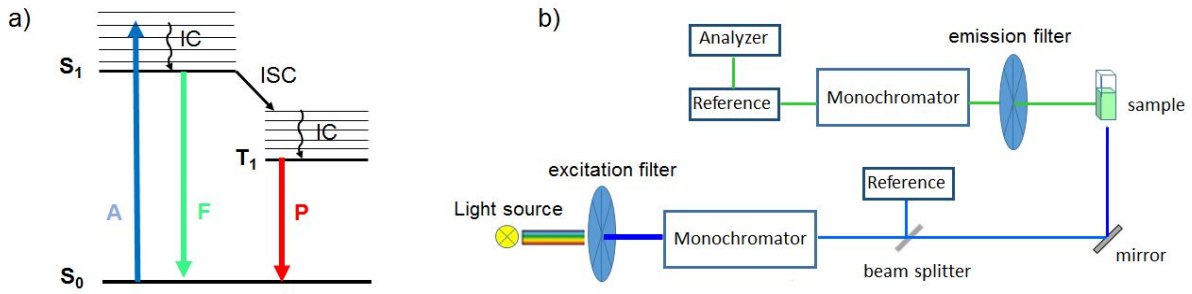

Figure 3.15 Jablonski diagram of fluorescence and phosphorescence mechanism (a), where A: absorption, F: fluorescence, P: phosphorescence, IC: internal conversion, ISC: Intersystem crossing. A sketch of fluorescence spectroscopy setup (b).

3.3.3.3 Fluorescence microscopy imaging

The fluorescence microscope is an optical microscope that can be used for imaging the surface domains with different photoluminescence behavior under illumination. We utilized the fluorescence microscopy imaging technique for visualization the morphological changes in the organic layer of LECs.

Figure 3.16a illustrates a schematic diagram of the reflected fluorescence microscope. The basic of fluorescence microscope relies on the irradiation of a sample with specific wavelengths and then detection of the emitted light from a sample that passes through another filter. Different emission response of various fields on the surface allows the investigation of surface

morphology. The emissive regions contrast with the weak or non-emissive parts that appear as a dark background. In our study, we observed the phase separation behavior of the polymer mixture since one of the polymers was a non-emissive material. In this thesis, a Nikon fluorescence microscope was employed to obtain the microscope images. We accompanied a halogen lamp with a blue bandpass filter (465-495 nm) as an excitation source in the system. We detected the emitted light through a green bandpass filter (515-555 nm).

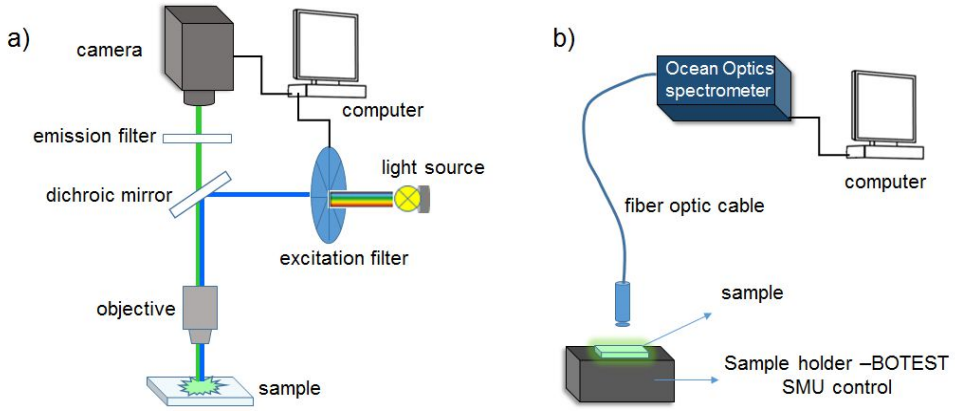

Figure 3.16 A sketch of fluorescence microscope (a) and electroluminescence measuring setup (b).

3.3.3.4 Electroluminescence

Electroluminescence (EL) is the optical response of a material under the applied electric field or current. We previously demonstrated the energy levels and radiative recombination pathways in OSCs in figure 2.5 (section 2.2). In a single layer OLED, the charge carriers recombine from HOMO-LUMO energy levels of the OSCs. In this case, PL and EL are expected to be identical. However, while PL depends on the optical properties of a material, EL is determined by several other factors such as the optical properties, physical structures, and charge transport characteristics of the optically active layers. Also, the electrical properties of the contacts and other related layers effect on the current injection and recombination. Therefore, it is well-known that EL is usually not equivalent to PL.

The electroluminescence spectra were recorded using an Ocean Optics spectrophotometer. As depicted in figure 3.16b, the sample (OLED or LEC) was mounted on the SMU unit of the BOTEST system and aligned to the optical path of the spectrometer. The EL was measured by applying a constant current density of 100 mA/cm^2 through the devices with an active area of 0.24 cm^2. Subsequently, we recorded the spectrum and subtracted the dark image spectrum from the saved spectrum. The CIE chromaticity coordinates were calculated using EL data with the help of a software program, named SpectrAsis (http://spectrasis.lti.kit.edu).

3.3.4 Electrochemical characterization techniques

Physical understanding of SPEs is inevitable for interpreting the performance and lifetime data of the LECs. In this section, we will explain the fundamentals of the electroanalytical techniques that were utilized to characterize the redox behavior of the materials.

3.3.4.1 Cyclic voltammetry

Cyclic voltammetry (CV) is generally used for defining the energy levels of OSCs[163]. In this thesis, we specifically applied this method to investigate general electrochemical behavior of SPE systems which is crucial for the device stability. The electrochemical stability window of SPEs is usually determined for appropriate selection of conductive polymer (CP) and electrolyte combinations. The oxidation and reduction onsets of CP should not exceed the oxidation and reduction potentials of electrolyte to eliminate irreversible electrochemical side reactions [126], [127]. Additionally, we also estimated HOMO and LUMO levels of the emissive materials from the oxidation and reduction onsets by using CV.

A classic three-electrode setup[164], which is composed of a working electrode, a counter electrode and a reference electrode in a cell, is usually employed for CV (Figure 3.17). A supporting electrolyte is engaged with the system to grant an efficient electron transfer between the redox species and electrodes. CV is a voltage-controlled system. While the voltage is cycled between the working electrode and a reference electrode, the resulting current is measured simultaneously. The obtained current vs. voltage data is plotted as voltammogram.

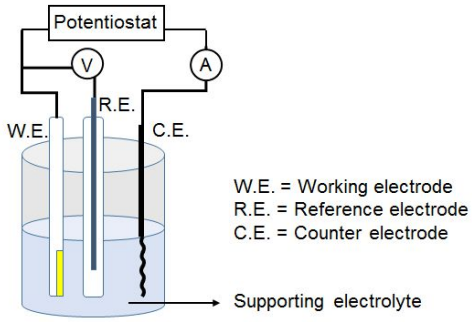

Figure 3.17. Schematic representation of a cyclic voltammetry with three-electrode setup.

In this thesis, we performed CV experiments by using a VERSASTAT 3 potentiostat (Princeton Applied Research). We placed a three-electrode system combining a Pt working electrode, a Pt/Ti counter electrode, and an Ag wire pseudo-reference electrode in a glass vessel. We used 0.1 M tetrabutylammonium hexafluorophosphate (>99%, Sigma–Aldrich) dissolved in an anhydrous DMSO or acetonitrile as the supporting electrolyte depending on the material solubility. We calibrated the system with ferrocene (Di(cyclopentadienyl)iron) (>98%, Sigma–Aldrich) as an internal reference redox system before each scan. The scan rate was 0.1 V/s. All the CV measurements were performed under an *argon* atmosphere to eliminate the oxygen reduction peaks on the data.

3.3.4.2 Electrical impedance spectroscopy

Electrochemical impedance spectroscopy (EIS) is a non-destructive technique and usually employed to determine ionic mobility and density for the transients of LECs[114]. In this thesis, EIS was implemented to elucidate the ionic conductivity of SPEs.

In the measurement, a small amplitude AC signal, (i.e., 50 mV), is applied to perturb the system and frequency response is recorded as impedance and phase angle[164]. The applied potential is given by

$$V = V_0 \exp(j\omega t)$$

The output current of the system is also an AC signal and it is represented by,

$$I = I_0 \exp(j\omega t + \varphi)$$

According to Ohm's law, impedance (Z) of the circuit at any frequency (ω) can be represented by

$$Z^* = V/I = (V_0/I_0)\exp(-j\varphi)$$

$$Z^* = Z_0\exp(-j\varphi)$$

$$Z^* = Z\ \cos\varphi - jZ\ \sin\varphi$$

$$Z^* = Z' - jZ''$$

The phase difference (φ) is represented by

$$\varphi = \tan(Z''/Z')$$

EIS measures the dielectric properties of the layer as a function of frequency. However, the overall conductance and capacitance of the layer is a complex combination of several processes during device operation. Hence, EIS is usually accompanied by a suggested equivalent circuit model[126]. The impedance is used to define the electrical behavior of the sample in terms of bulk resistance (R_b) and its equivalent circuits. The bulk resistance is at the point where the imaginary impedance becomes zero; therefore the real part of the impedance is equal to the overall impedance. The ionic conductivity can be extracted from the Nyquist plot, as shown in figure 3.18b, where the R_b refers to the bulk resistance.

We conducted the impedance measurements by using Autolab PGSTAT302N impedance analyzer at the frequency range between 0.04 and 100000 Hz with an amplitude of 10 mV.

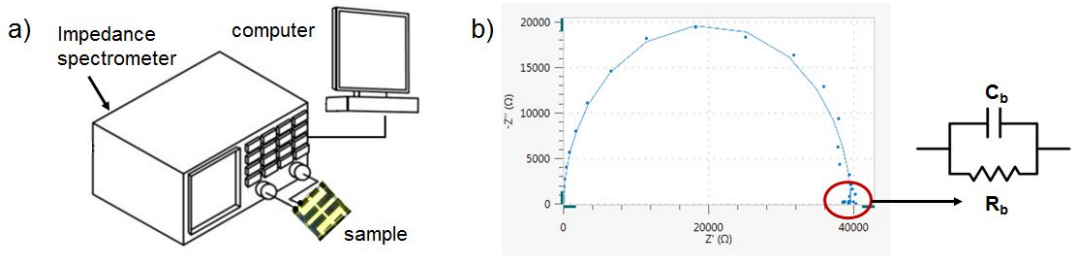

Figure 3.18 Impedance spectrometry setup (a), Nyquist plot of AC impedance data and related equivalent Debye circuit (b) with R_b: bulk resistivity and C_b: bulk capacitance.

3.3.5 Surface characterization techniques

3.3.5.1 Polarized light microscopy

The polarized light microscopy technique was used to determine the aggregation tendency of the small molecule in the solid film phase (see section 4.2.1.1). In the setup, a microscope is equipped with an analyzer (a second polarizer), placed on the light path between the objective and the camera (Figure 3.19). The sample is exposed to the polarized light coming from the underlying light source and passes through the first polarizer. Usually, the polarizer and analyzer are in crossed order, so that the analyzer absorbs most of the light that passes through the specimen. The image of the sample looks mostly dark, except for the structures that are birefringent. In this thesis, we used an Olympus BX51 polarized light microscope with LMPLFLN 20x objective. We evaluated the data for both qualitative and quantitative investigation.

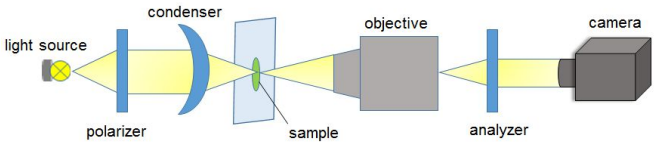

Figure 3.19 Schematic illustration for the optical path of polarized light microscope.

3.3.5.2 Atomic force microscopy

The atomic force microscopy (AFM) was used for the morphological investigation of the active layers in LECs. AFM is a high-resolution scanning probe microscope that can detect fractions in nanometer scale. In the measurement setup, a cantilever with a sharp probe scans the surface of the specimen (Figure 3.20). When the tip travels near to the surface of the sample, the forces between the tip and sample distort the cantilever according to Hooke's law[165]. The distortion on the cantilever affects the reflection of the laser beam to be displaced onto the photodiode. In principle, there two main modes of operation, namely contact mode and non-contact mode depending on the cantilever vibrations.

In this thesis, we operated a DME DS 95 Dualscope AFM instrument in ambient air. The AFM topography images were recorded at tapping mode, using a highly doped silicon cantilever from NanoWorld (Arrow NCR) with the resonance frequencies about 285 kHz and the tip radii of less than 10 nm.

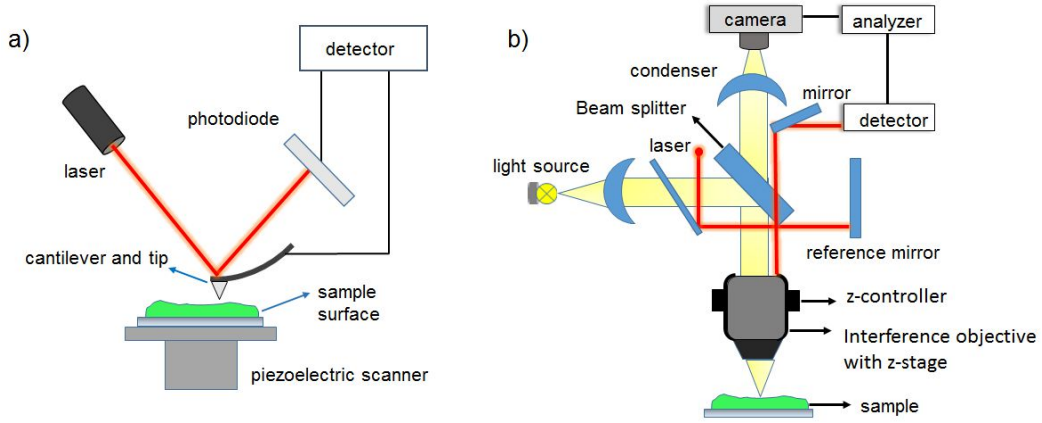

Figure 3.20 Schematic representation of atomic force microscope (a) and white light interferometry microscope (b).

3.3.5.3 White light interferometry

White light interferometry is a contactless optical method to measure a 3D surface topography and the roughness of a sample. Light interference occurs when there is a difference in distance traveled by the light (light path) from the surface of a sample to a certain point. The optical device divides the light coming from the light source into two beams and then recombines them to create an interference pattern. The combined pattern is analyzed to determine the difference in paths the two beams traveled. The interferometer is a standard optical microscope with an interference objective to visualize the microscopic structures.

In our work, we investigated the surface roughness and obtained the topography images by using a Sensofar PLu Neox White Light 3D interference microscope with a 50 times magnification objective. We carried out the experiments with the monochromatic illumination in the phase shifting interferometry (PSI) measurement mode. We preferred PSI mode for a better height resolution. The surface roughness of each sample was determined accordingly.

Chapter 4
Gravure printed small molecule organic light-emitting devices

In the following chapter, the gravure printing technique will be highlighted as an industrial relevant device processing method for the fabrication of small molecule based electroluminescent devices. The adaptation of the technique was provided with modifying the functional ink properties or setting up the gravure process parameters, resulting in continues and homogenous films of the small molecule. The printed layers are then implemented as the emissive layer of small molecule OLEDs (SMOLEDs) and small molecule LECs (SMLECs). The device characteristics regarding current density-voltage-luminance and efficiency are obtained. The results were compared to the device characteristics of respective spin-coated reference devices to define the effect of the printing process on the device performance.

The first part of this chapter related to SMOLEDs was published in the *Journal of Organic Electronics* in collaboration with Merck KGaA group in Darmstadt[166]. The second part of the chapter linked to small molecule LECs contributed in the book chapter of *Light-Emitting Electrochemical Cells: Concepts, Advances, and Challenges*, released by Springer in 2017[16].

4.1 Introduction and aim of the work

Today one of the prime concerns of the organic electronics field is to use high throughput, large scale R2R printing or coating methods to reduce the manufacturing costs in mass production. Additionally, these methods allow deposition on materials on different substrates, yielding flexible, and light-weight products.

Small molecules (SM) and conducting polymers (CPs) are two main classes of organic materials used for optoelectronics (Section 1.1). Low molecular weight materials are usually preferred due to their highly efficient devices, ease of synthesis and purification steps, as well as better charge transport properties comparing to CPs[44], [45]. Additionally, phosphorescent triplet emitters exhibited the higher EL efficiencies comparing to singlet emitters (Section 2.2.2.2). Small molecule based devices are generally fabricated by thermal evaporation in a vacuum. Printing methods are commonly applied for PLEDs, because of mechanical properties originating from their high molecular weight (M_W) feature. The solution of SMs shows low viscosity values of ~ 2 mPa s that is not the printable range of conventional printing techniques. Thus, SMs were typically deposited by inkjet that requires low viscosity inks[132], [133].

In comparison with inkjet, gravure takes over with the high throughput (1-10 m/s) and lateral resolution on the μm scale properties[135], [145]. Among other industrial methods, it is easy-to-handle and single step printing process with a few parameters to control and also resistant to the different type of solvents. In recent years, gravure has been implemented for the printing of active layers for polymer OLEDs[6], [135], [167], [168]. However, adapting this printing technique for the small molecular materials remain challenging, due to the fact that gravure requires high viscosity range of functional inks between 50-200 mPa s, yielding 1-10 micrometer thick films[169]. As previously discussed in section 2.2.2, the operational principle of OLEDs is thickness dependent with a total active layer thickness requirement of ~100 nm. Additional to that, layers should be uniform and pinhole-free to prevent shorts. However, the surface tension of the fluid plays a vital role on the printing nanometer thick layers, when the viscosities remain far below than graphical ink standards[170]. At this context, there is only limited research have been made for gravure printing of small molecules.

Recently, Bornemann et al. reported on the printability of small molecule (Spiro-MeOTAD) based inks on ITO coated glass by setting the printing process parameters[170]. They have adjusted the gravure cell volume, printing speed, and solution concentration to grant homogenous thin films with thicknesses of 10-20 nm, which would not be sufficient to employ as an active layer in a complete device stack. In order to achieve higher thicknesses for the active layers in OLEDs, an interesting strategy is dispersing small molecules into an appropriate polymer matrix (host) to modify the ink properties[171], [172]. Lee et al. fabricated gravure printed OLEDs using a hole transport polymer, poly-N-vinyl carbazole (PVK) as host and an iridium complex as the emitter[171]. The device showed maximum luminance of 300 cd/cm^2 at 20 V. Kim et al. obtained a maximum luminance of 280 cd/m^2 at 8 V using MEH:PPV-rubrene mixture as active layer[172]. These results motivated us for further investigation of gravure printing in terms of adapting this technique for SMOLEDs.

This chapter is divided into two main subsections: SMOLEDs and SMLECs. The obtained results will be discussed accordingly.

The first section describes the gravure printed flexible SMOLEDs, in which the active layer was composed of a green small-molecule triplet emitter (SM-GrünA) embedded in an ultra-high molecular weight polystyrene (UHMW-PS) host. The UHMW-PS was used to modify the rheological properties of the functional ink. Since UHMW-PS is an insulating polymer, it did not interact electrically or optically with the emitter. Additionally, we observed that embedding SM into a host suppressed the SM aggregation in the thin film[173]. Two different M_w of the host polymer and various SM:PS weight to weight (w/w) ratios in two different solvents were tested to control the ink parameters such as viscosity, surface tension, and solvent drying kinetics. Furthermore, the film leveling time and drying time were taken into account for quantitative analysis of printed layer demodulation. The modified rheological properties of the ink resulted in homogenous printed layers that were employed as the active layer of SMOLEDs. The results will be detailed in section 4.2.1.

In the second section, we will focus on the implementation of the gravure technique for printed flexible small molecule LECs (SMLECs) with air-stable cathodes. In this part of the work, some of

the process parameters such as transfer volume, tone, line screen were modified, while keeping the ink formulation constant. The active layer was composed of SM-GrünA and poly (methyl methacrylate) (PMMA). PMMA is an insulating polymer which was performed both as the binder and ion-solvating polymer for the ionic species. Tetrabuthylammonium tetrafluoroborate ($TBABF_4$) was utilized as a salt additive in the solid polymer electrolyte (SPE) to ensure the number of ionic species for efficient electrochemical doping in the active layer. Different printing plates were utilized for altering the layer thicknesses to adjust the junction zone, i.e., the emission zone for better device performance. The results will be comprehensively discussed in section 4.2.1.

4.2 Results and discussion

4.2.1 Small molecule organic light-emitting diodes (SMOLEDs)

4.2.1.1 Ink formulation and printing tests

Ink formulation is a complex process. The interplay between surface tension, viscosity and drying time should be carefully controlled in to order to produce homogenous films.

The viscosity behavior of the ink at different shear rates plays a significant role for the fluid dynamics at the different stages of the gravure-printing process as shown in section 3.2.1.2. The measured viscosity at high and low shear rates affect the ink transfer and film drying conditions, respectively. A low viscosity range of the fluid at high shear rates would be expected to reduce the hydrodynamic instabilities and assure proper patterning. At low shear rates, the viscosity should not rise substantially to provide sufficient time for film leveling of the printed lines, i.e., fingering patterns. In other words, Newtonian fluid behavior in shear flow (only small changes in shear thinning or thickening) produces on an excellent printing result. For instance, Hernandez-Sosa et al. added a high boiling point solvent into the ink solution to delay drying time and reduce high viscosity values at low shear rates for a non-Newtonian fluid[168].

In our work, we utilized two high molecular weight polystyrene polymers as the binder for altering the ink properties. While adjusting the rheological properties at printability range, the

ultimate functionality performance should not be dismissed when the polymeric host are insulating polymers. The low amount of polymer matrix generates printing issues and excess of it increase the amount of non-conductive parts in the active layer, in addition to that reduce the charge recombination. Thus, the binder was added with optimized quantities in our work. Two different molecular weights of PS binder, HMW-PS (Mw: ~1x10^6) and the UHMW-PS (Mw: ~30x10^6) were dissolved separately in toluene and anisole (Figure 4.1a). Since the viscosity of a polymer was proportional to its molecular weight, the viscosity of the 5 g/L UHMW-PS was at a comparable range of the 10 g/L HMW-PS (4-6 mPa s). This effect was found to be beneficial to reduce the amount of insulating polymer, as well as non-conductive paths in the active layer.

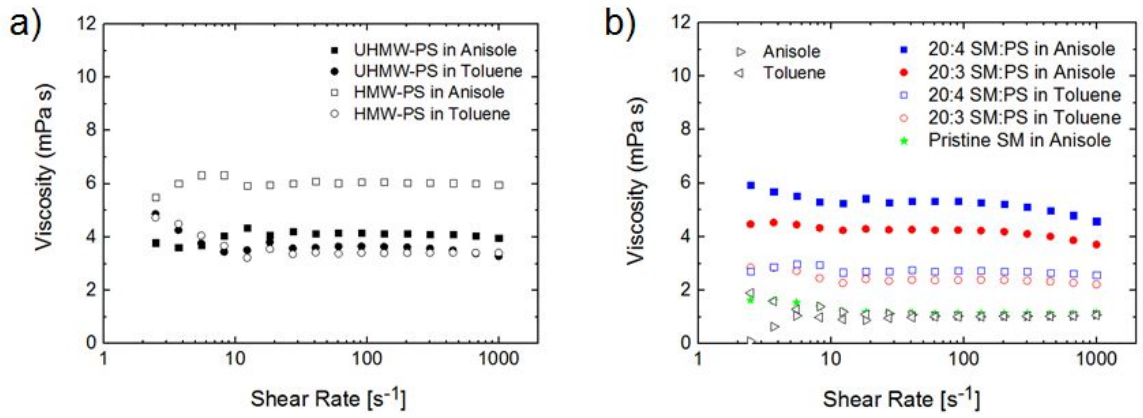

Figure 4.1Viscosity of inks as a function of shear rate for pristine HMW (10 g/L) and UHMW (5 g/L) polystyrenes (a), and SM:PS blends with reference pristine small molecule (b).

Figure 4.1b shows the viscosity measurements of SM:UHMW-PS formulations at different w/w ratios with a total concentration of 23 g/L and 24 g/L in toluene and anisole, respectively. A Newtonian behavior was observed for the viscosity over the whole range at regular shear rates. The SM:UHMW-PS blends with a w/w ratio of 20:3 and 20:4 were utilized to increase the amount of SM in the mixture while keeping the viscosity values at a printable range. All formulations had a higher viscosity value than the pristine SM (20 g/L in anisole) that had a viscosity less than 2 mPa s (no significant difference compared to the pure solvents).

The gravure printing technique is based on ink transferring from an engraved plate to the substrate surface. The details of the gravure printing process can be found in section 3.2.1.2.1. The organic electronic device performance is strongly dependent on the film quality of organic layers. As physical consistency of the printed films, pinhole-free and uniform thicknesses are required. So, we compared the outcome of several printing tests and assessed the suitability of the layers for further device fabrication. Different ink formulations of SM:UHMW-PS on figure 4.1b, were printed directly on PEDOT:PSS coated PET.

Contrast-enhanced photographs of the printed fields under UV light illumination are presented in figure 4.2a. The printed films from toluene based inks exhibited surface undulations.

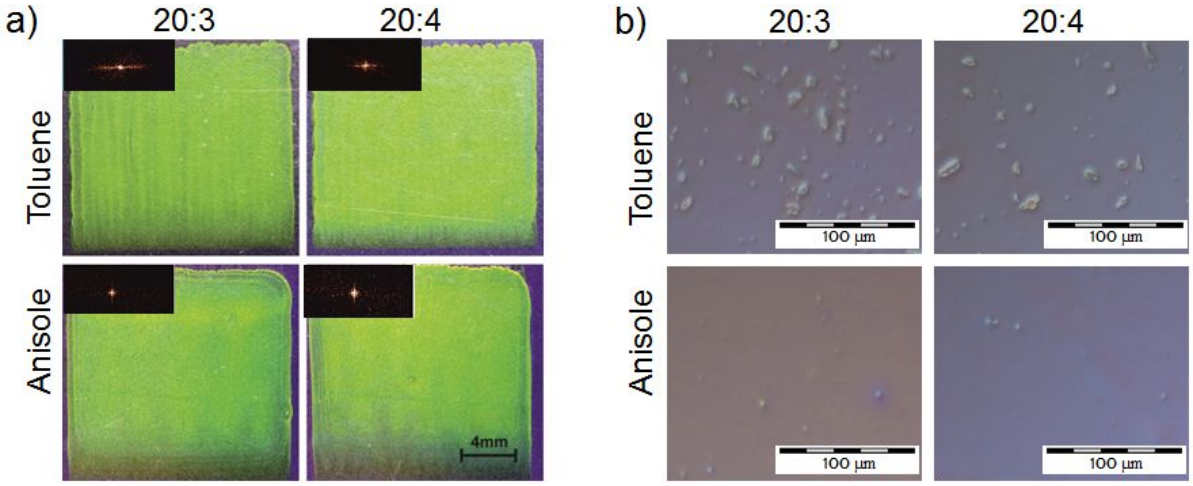

Figure 4.2 Contrast-enhanced images of the gravure printed films of SM:UHMW-PS blends with 20:3 and 20:4 w/w ratios in different solvents under UV irradiation (a). Inset: FFT diagrams of corresponding images. Polarized light microscope images of printed films (b).

Such thickness modulations, namely viscous fingering or Saffman-Taylor instability, is a common phenomenon in coating and printing applications, which originates from hydrodynamic instabilities during the ink splitting process[174]. Due to its low viscosity, the ink is not only deposited from cells but also wet walls of the cell. Forming continues meniscus when the roller is lifted. So, the lamella-like meniscus disturbs the fluid surface and results in a periodic modulation along the printing direction. In our work, the film homogeneity was improved by the printing of anisole based solutions. The slower drying time of anisole (boiling

point, T_B= 154°C) than toluene (T_B= 111°C) maintained adequate time for surface leveling and resulted in more homogeneous films.

As a quantitative representation of the printed layer undulations, the appropriate leveling time (τ_{lev}) of the patterns was calculated according to the equation in ref.[170]:

$$\tau_{lev} = \frac{3\eta\lambda^4}{16\pi^4\,\sigma_T h_0^3} \quad (1)$$

, where η, σ_T, h_0, and λ respectively, signs the viscosity, total surface tension, wet film thickness and the period of the thickness modulation. The estimated τ_{lev} was then compared to the experimentally obtained drying time (τ_d) and correlated with the printing results. In principle, leveling time should be higher than drying time to grant homogenous layers.

We summarized the leveling time and its parameters in Table 1. The wet film thickness, h_0, was estimated from the solid film thicknesses and the concentration of SM:PS inks. The average film thicknesses were measured as 132 ± 9 nm, 155 ± 10 nm, 130 ± 17 nm, 162 ± 13 nm for the ratios 20:3 (T), 20:4 (T), 20:3 (A), 20:4 (A), respectively. The modulation wavelength (λ) was determined from the profilometry measurements and optical microscopy images. The surface tension of functional inks was detected by using the pendant drop method (Figure 4.3) by Dr. Hernandez-Sosa. The viscosity values at a low shear rate (2.48 s^{-1}) were used for the calculation. All formulations exhibited similar τ_{lev} between 0.2 and 0.4 sec. The leveling time was lower than the drying time for all samples. However, the drying time of the anisole based formulations was much larger than the demodulation time of the film which ensures a more homogeneous surface.

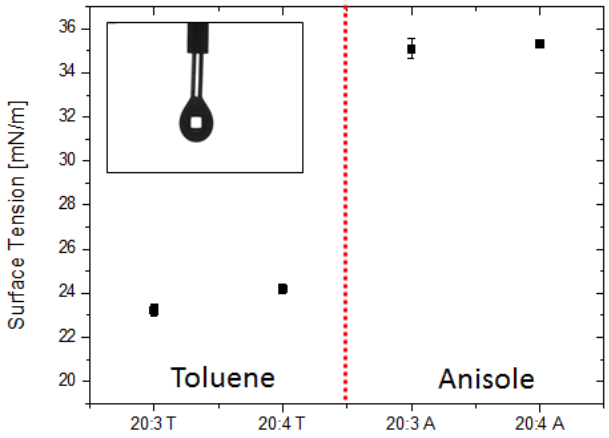

Figure 4.3 The surface tension values versus the formulation of functional inks. Inset image: The photograph of liquid drop on dosing needle during measurement, which was subsequently analyzed by using the inset formula.

Table 4.1 Parameters determined for printed layers:

Sample	**Modulation wavelength λ (mm)**	**Wet film thickness h_0 (µm)**	**Surface tension σ_T (mN/m)**	**Viscosity η (mPa s)**	**Leveling time τ_{lev} (s)**	**Drying time τ_d (s)**
20:3 Toluene	0.69± 0.03	0.51	23.23 ± 0.25	2.85	0.4±0.2	17
20:4 Toluene	0.72± 0.03	0.57	24.20 ± 0.06	2.71	0.3±0.1	17
20:3 Anisole	0.69± 0.03	0.57	35.10 ± 0.44	4.47	0.3±0.2	90
20:4 Anisole	0.72± 0.03	0.68	35.30 ± 0.15	5.94	0.2±0.2	90

The inset diagrams on figure 4.2a present the fast-Fourier transformation (FFT) of the corresponding printed fields to evaluate the homogeneity of the printed layers. The FFT diagram represents the distribution of the pixel intensity of the optical microscope image (i.e., an ideal homogenous layer would appear as a single dot in the center of the diagram). The horizontal pattern in the FFT image of toluene films referred to the undulations that were already visible in the photos. In contrast, the anisole samples exhibited a less extended FFT pattern as a result of improved layer homogeneity.

Figure 4.2b shows the polarized light microscope images of the corresponding printed fields in figure 4.2a. We defined the density and size of the aggregates from the contrast-enhanced microscope images. The increase of PS amount in the blend (from 20:3 to 20:4 w/w SM:PS ratio), reduced the density of the aggregates in ~ 50%, while anisole based solutions present ~ 80 % less number of clusters for each of the SM:PS ratios. The typical size of the aggregates ranged between 13-21 μm^2. SM aggregation in the OLED active layer is detrimental for the device performance since it promotes the luminescence quenching[175]. Therefore, Anisole based ink formulations improved the film formation and suppressed SM aggregation.

Before applying the printed layers as an emissive layer in SMOLED device stack, the mixture with a lower amount of PS was tested to reduce non-conducting pathways for more efficient charge transport. The SM:PS blend with a w/w ratio of 20:2 in anisole exhibited the viscosity ~2.5 mPa s, which was not so different from the value of pristine SM (Figure 4.4a). However, the functional inks at lower viscosity range accentuated the pattern reproducibility problems (e.g., round instead of sharp corners or overflowing from pattern field) as shown in figure 4.4b. The patterned cells were united because of overflow. In comparison with the other ratios, this effect was more likely due to the much lower viscosity of 20:2 rate. So after all, we adhered to the ink formulations with 20:3 and 20:4 ratios in anisole for the fabrication of OLEDs.

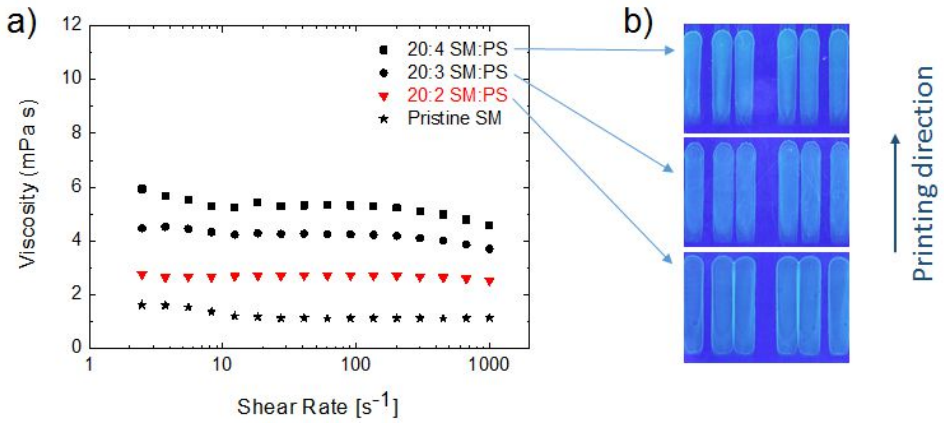

Figure 4.4 Viscosity of SM:UHMW-PS blends with varying UHMW-PS ratio in anisole (a) and corresponding contrast-enhanced images of the gravure printed blends under UV irradiation (b). The total solid concentration is 22 g/L, 23 g/L, and 24 g/L for 20:2, 20:3, 20:4 blends, respectively, and 20 g/L for pristine SM.

4.2.1.2 Device fabrication and characterization

4.2.1.2.1 Spin-coated OLEDs

To define the performance of the SM:UHMW-PS blends as emissive layer (EML) without any influence of the printing process, we first built the spin-coated OLEDs as a reference. Figure 4.5 exhibits the optoelectronic characteristics of the reference OLEDs with pristine SM and SM:PS mixtures. Comparing to the pristine SM based device, SM:PS OLEDs showed a lower current density and lower luminance concerning the amount of insulating polymer in the active layer (Figure 4.5a). The higher amount of UHMW-PS in the blend increased the non-conductive pathways in the emissive layer, therewith affected the efficient charge transport and recombination of charge carriers. Thus, the overall device performance dropped. However, the polymeric matrix was engaged for more efficient exciton transfer to the emitter by preventing exciton quenching, so that increased the device efficiency[176]. The turn-on voltages (V_{on}) was found to be 3.0, 4.5 and 8.0 V for the pristine, 20:3 and 20:4 devices, respectively. The difference in V_{on} was related to the variation of film thicknesses due to the increasing viscosity of the fluid by mixing SM with PS.

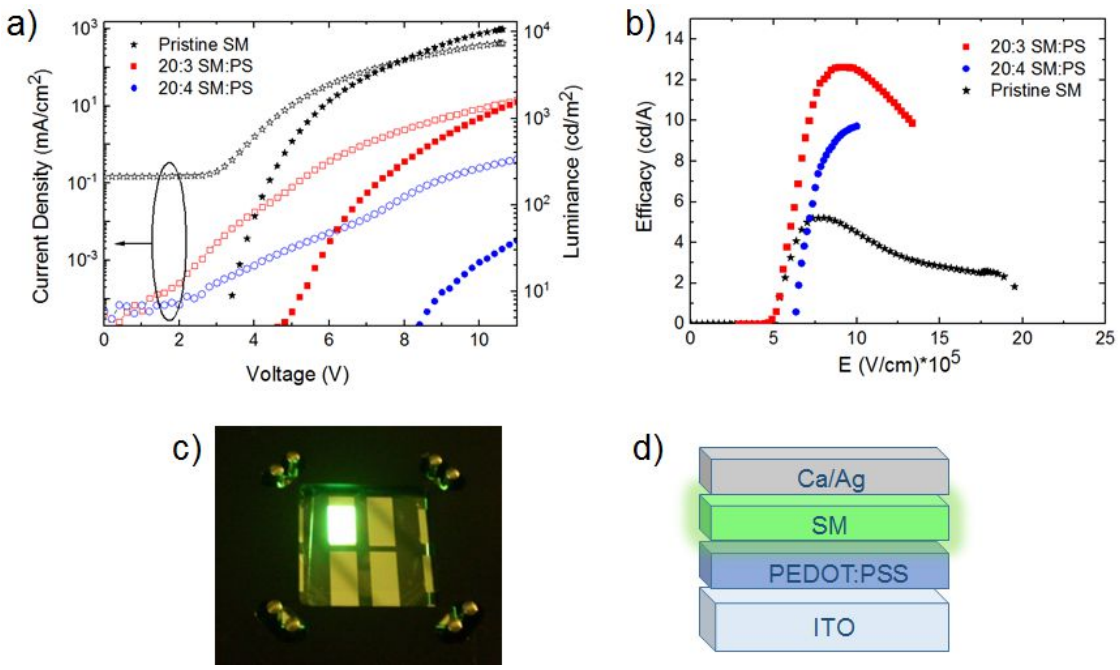

Figure 4.5 J-V-L characteristic (a), luminous efficiency vs electric field (b) of spin-coated SMOLEDs. A photograph of spin-coated SMOLED under operation (c) and corresponding device architecture (d).

Figure 4.5b shows the luminous efficiency (efficacy) as a function of the electric field. The turn-on voltage was comparable for all devices at the same electric field after eliminating the EML layer thickness effect. Both blends presented a higher efficacy than pristine SM OLED. We obtained the highest maximum electroluminescence efficiency 13 cd/A for the device based on SM:UHMW-PS with a w/w ratio of 20:3. An increase in the device efficiency was due to the fact that as a result of reduced SM aggregation and consequently less fluorescence self-quenching in the thin film. As recently reported by Kunz et al., diluting semiconductor with an insulating host such as polystyrene can reduce the charge trapping and result in enhanced luminous efficiency[176]. Additionally, merging SM in insulating polymer lowers pinhole density and reduces leakage current[177]. The luminescence of spin-coated SMOLED on the glass substrate and the related device architecture is shown figure 4.5 c and d, respectively.

4.2.1.2.2 Printed OLEDs

At the final step, the gravure printed blends were tested as EML of OLEDs to define the influence of the printing process on the device performance. The same device architecture (see Figure 4.5d) was applied for printing the diode on an ITO-coated PET substrate. In this part of the study, both PEDOT:PSS layer and EML were gravure printed consecutively. Figure 4.6a shows the optoelectrical properties of gravure printed SMOLEDs with SM:UHMW-PS at w/w ratio of 20:3 and 20:4. Both device types had an identical luminance-voltage behavior with a V_{on} of ~ 3.5 V. The 20:3 ratio exhibited a better device performance with the maximum luminance intensity of 850 cd/m^2 at 15 V. The highest luminous efficiencies were obtained 7.7 cd/A, and 4.6 cd/A for the 20:3 and 20:4 blends, respectively (Figure 4.6b). On the one hand, the unsmooth J-V and efficiency curves could be related to the inhomogeneous electric field throughout the organic layers. The thickness variations in the active layer were produced during the printing process. On the other hand, the shape of curves might be referred to the micro-morphological defects of the Polymer:SM blend. The printed mixtures presented a poor performance comparing to its respective spin-coated reference devices as a result of the printing process (e.g., broader thickness distribution). Nevertheless, the printed 20:3 ratio exhibited ~ 67% higher efficiency comparing to the spin-coated pristine SM OLEDs.

Figure 4.6c shows the normalized electroluminescence (EL) spectra of SM:PS mixtures and the normalized photoluminescence (PL) spectra of SM in solution. Both EL spectra were in a good agreement with the PL spectrum of SM. Optical electronic transition bands of EL were correlated with the photoluminescence energy peaks. The bathochromic shift in between EL and PL spectra of small molecules was reported as a well-known phenomenon due to molecular π-π packing in the thin film phase[178]. The increase in a lower energy band at 550 nm (i.e., low-energy shoulder) suggested that the higher content of PS in the blends reduced the SM aggregation and self-quenching. Considering the EL data, we concluded that the UHMW-PS did not interact optically or electrically with the emitter. The gravure printed flexible SMOLED on the plastic PET showed a uniform luminescence over the whole pixel area as you can see in

figure 4.6d. The devices bearing air-sensitive cathode (Ca/Ag) were subsequently encapsulated with barrier foil.

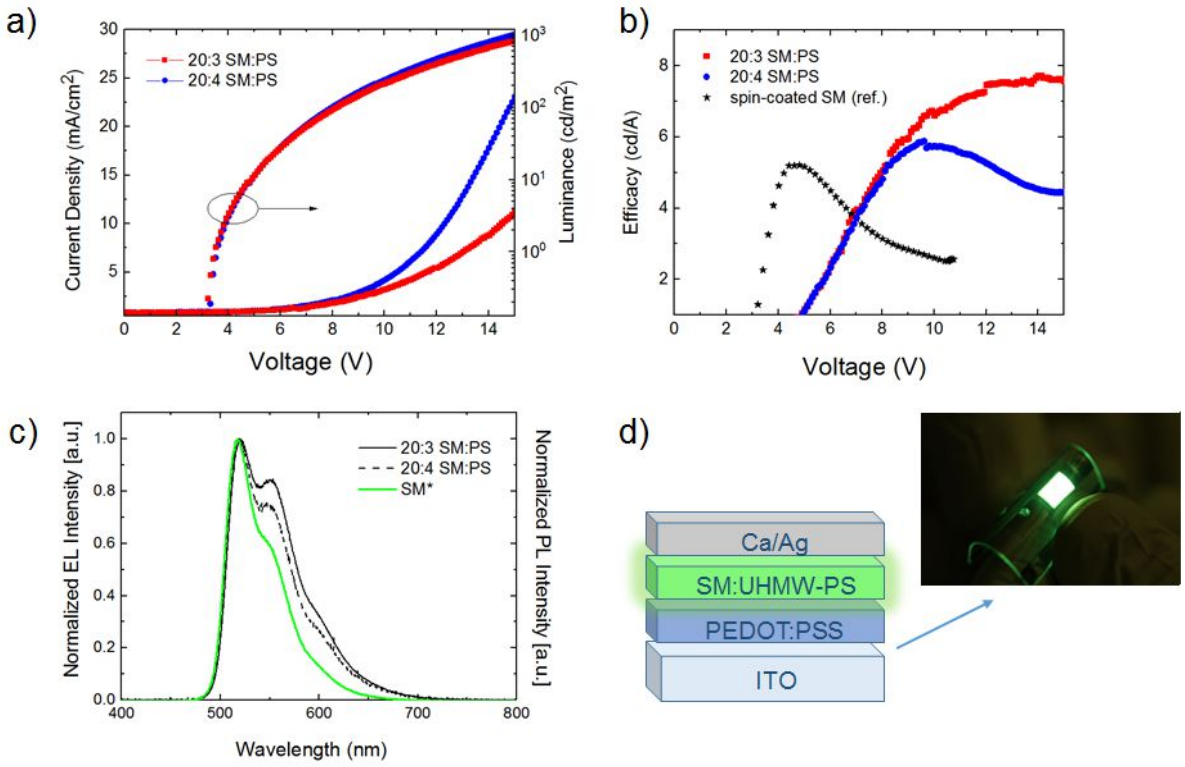

*Figure 4.6 J-V-L characteristic (a), luminous efficiency vs electrical field (b) and electroluminescence spectrum (c) of gravure printed SMOLEDs. A sketch of device configuration and a photograph of flexible SMOLED on PET under operation (d). *The PL spectra of SM is measured (0.01 g/L in toluene) at room temperature.*

As follow-up work, ink formulations of SM were modified for the scaling-up purposes of SMOLEDs. By using the similar formulations within a collaborative work, Raupp et al. recently demonstrated the slot-die coated and flexo-printed SMOLEDs with the active area of 0.24 and 1.96 cm² on the glass substrates[136]. Additionally, a demo SMOLED with an active area of 27 cm² was fabricated as a proof-of-concept for further scale-up development (Figure 4.7). We tested several batches in terms of J-V-L and efficacy characteristics to evaluate batch-to-batch device performance through the reliability and applicability of both techniques. Slot-die coated HTL and EML based SMOLEDs with LiF/Al cathode exhibited an average current efficiency of 30

cd/A at 12-13 V with low standard deviations. The maximum luminance intensity of ~ 5000 cd/m² with the turn-on voltage of ~ 4.5 V was obtained from the fabricated devices.

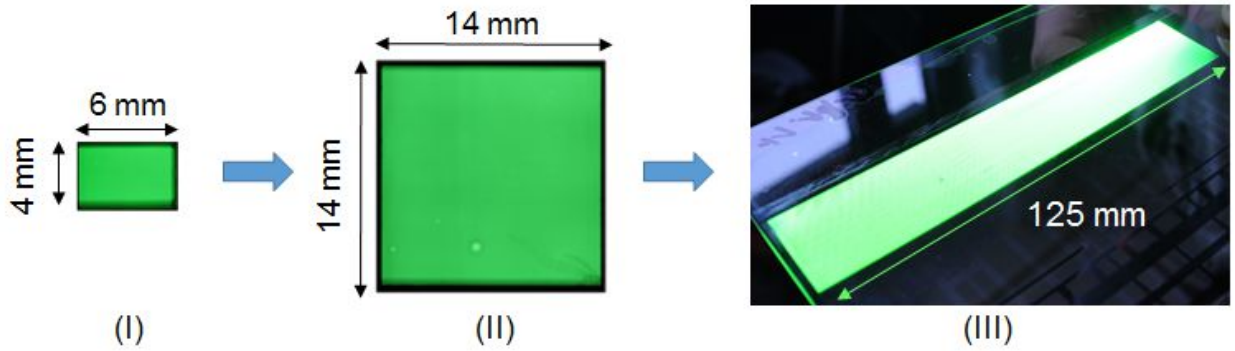

Figure 4.7 The photographs of slot-die coated SMOLED with different active area of 0.24 cm² (I), 1.96 cm² (II) and 27 cm² (III) under operation. Adapted from ref. [136]. *Copyrights @ 2016 WILEY-VCH Verlag.*

4.2.2 Small molecule light-emitting electrochemical cells (SMLECs)

Despite the fact that all the great efforts have been made up to date for printing and fully solution processed OLEDs, evaporating cathodes in inert conditions and encapsulation remain hurdles in the field[6]. In this context, LECs may allow the large area printing of air-stable cathodes. We will consider printability of LECs in the next section.

LECs are a new class of organic light-emitting devices representing several advantages comparing to OLEDs. Single-active-layer device architecture makes them attractive for easy fabrication using printing and coating techniques regardless of thickness variation limits and complex, multilayered architecture. Moreover, due to the unique working principle of the cells which is explained section 2.3.2, charge injection from electrodes into the active layer is independent to the work function of the electrodes (i.e., no low work function metal is needed as a cathode).

In this context, LECs bearing air-stable cathodes have drawn particular attention, since they are suited well for wet-based continuous R2R process [17]. Furthermore, its configuration allows

great flexibility in the device design, the applicability of different methods and various substrates. Different techniques have been applied for the deposition of the active layers, e.g., slot-die coating[141], spray-sintering method [142], [143], and direct-write patterning method[179].

LECs are typically classified based on the type of emitters involved in the active layer, which can be CPs [85]–[89], ionic transition-metal complex (iTMC) [90]–[95], organic small molecules[99], [100], and hybrid system [97], [98]. iTMCs are luminescent ionic materials with different organic ligands are arranged around a metal center. They are intrinsically ionic, so in principle, iMTC-LECs can perform as single layer LECs without additional ionic species. However, LECs can be based on small molecular-weight charge transporting and emitting molecules in the presence of an electrolyte[100]. Edman et al. reported on the in-situ electrochemical doping of non-ionic small molecule based LECs[180]. In this chapter and the following chapters, we will refer to polymer LECs (PLECs) when the light-emitting material is a polymer, and to SMLECs when it is based on a triplet small molecular-weight complex.

In our work, the chemical formula of the small molecule was confidential. So, regardless of whether ionic or non-ionic transition-metal complex, we blended it with an ion-conducting insulator polymer binder to modify the rheological parameters. In this thesis, the active layer of a typical small molecule based LEC (SMLEC) was composed of a triplet emitter and a solid polymer electrolyte (SPE). We utilized polymethyl methacrylate (PMMA) as SPE and a salt additive to ensure the number of ionic species for sufficient electrochemical doping of double layers.

4.2.2.1 Printing tests

A high molecular weight of PMMA was used as a binding polymer to improve the viscosity of SM ink. PMMA was engaged as inert polymer additive for spin-coated ionic SM-based LECs[181] and iTMC-LECs[182] to decrease the self-quenching for improved efficiency. It did not affect the optical properties of the emissive materials.

As previously reported by our group, we tested the different molecular weights of PMMA ranging from 3500 to 1.000.000 with the salt additive of $TBABF_4$ as SPE for CP-based LECs [183]. We obtained the highest ionic conductivity for the highest M_w of PMMA (~$1x10^6$). The device turn-on time and turn-on voltage were directly correlated with the ionic conductivity of SPE. Additional to that, PMMA with M_w of ~$2x10^6$ was used as the electrically inert binder for the gravure printed SMOLEDs during a bachelor thesis work of Mervin Seiberlich in our group[184]. He tested different concentration of PMMA ranging between 2-5 g/L in anisole for SMOLEDs. The viscosity values of ~ 2.5-4 mPa s for PMMA solution showed Newtonian behavior and was found to be comparable with 2-3 g/L of PS (M_w = ~$30x10^6$). However, the printing outcome of 3 and 5 g/L of PMMA with a relatively high line screen (70/80 ln/cm) and high tone values (90-100%) exhibited strong surface demodulation.

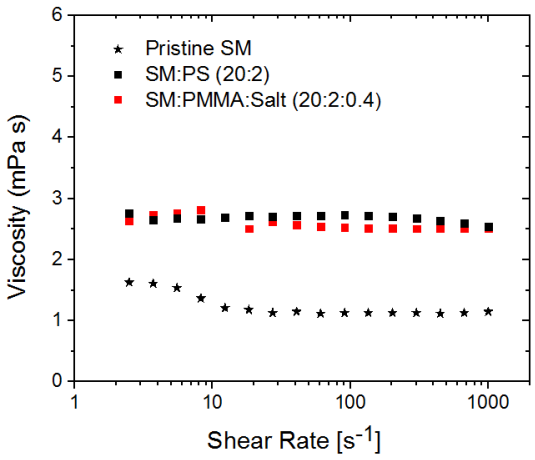

Figure 4.8 Viscosity of SM:PMMA:salt (22.4 g/L) blend comparing to SM:UHMW-PS (22 g/L) blend and pristine SM (20 g/L) in anisole.

In this thesis, we utilized the highest M_w of PMMA (~$2x10^6$) among those which were tested previously in our group. The solid concentration of PMMA was kept at 2 g/L in the blend. The ink formulation of SM:PMMA:salt (w/w ratio of 10:1:0.2) with a total solid concentration of 22.4 g/L was prepared in anisole to perform viscosity measurements and printing tests. $TBABF_4$

was used as an additional ionic source. Figure 4.8 exhibits the viscosity behavior of the functional ink. The Newtonian behavior of the ink was promising for further investigation. The viscosity range was almost identical with SM:UHMW-PS blend (20:2) and comparable with the optimized ink formulations in figure 4.4a. So, in this part of the study, we employed different engraved gravure plates to adjust the film morphology and thickness.

Cell parameters had a significant influence on the thickness and morphology of printed layers. Four different gravure plates with various line screens of 60/54 ln/cm, 80/70 ln/cm and 100 ln/cm with two tone values (90 and 100%) were used to ensure a thin, continuous film of SM ink (Figure 4.9). Relatively high line screen values (i.e., more cells/cm, and thus smaller in depth) and high tone values were chosen to give a continuous film without printing undulations. The change in the tone value from 90 to 100% resulted in film thickness from 60-90 nm, respectively. Afterward, the optimized films performed as an active layer of LECs.

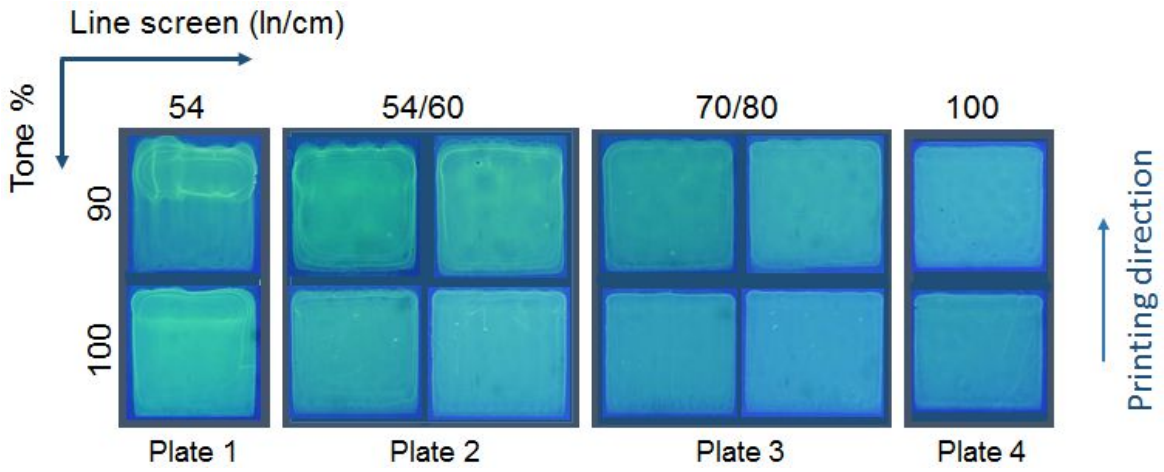

Figure 4.9 Contrast-enhanced images of the gravure printed films of SM:PMMA:Salt blend using four different gravure plates under UV irradiation.

4.2.2.2 Device fabrication and characterization

The active layer was printed on top of an ITO-coated glass or PEDOT:PSS coated ITO glass. The optoelectrical characterization of SMLECs is depicted in figure 4.10. We altered the active layer thickness while keeping the ratio of PMMA constant in the blend. The increase of the film

thickness resulted in lower current densities (Figure 4.10a). However, the maximum luminance intensity and the turn-on voltage of the printed layers on top of PEDOT:PSS (with the thickness of 60-75 nm) remained constant. The maximum luminance was detected ~ 8000 cd/m^2 with a turn-on voltage of ~ 5 V for the SMLECs implying HTL (Figure 4.10b). However, the shift between two maxima (from 14 V to 16 V) might be raised from the time-dependent operation mechanism of LECs. The initial formation and width of the recombination zone is due to the continuous electrochemical doping of the double layers and determined by the doping-dependent transport[75]. In CP-based LECs, the junction width depends on the applied voltage as reported elsewhere[185].

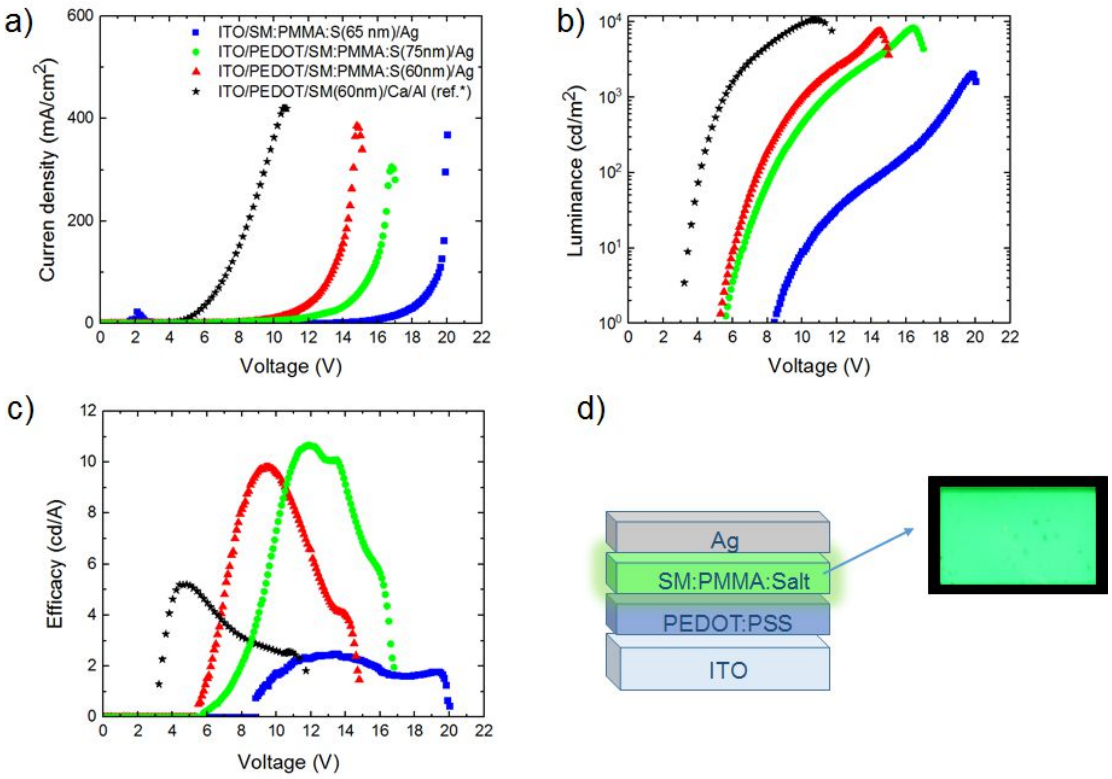

Figure 4.10 Current density-voltage (a) and luminance-voltage (b) characteristics and luminescence efficiency of SMLECs (c). Illustrative representation of device configuration and a photograph of SMLEC under operation.

The efficacy of the printed layers was improved comparing to the spin-coated pristine SM-based OLEDs (Figure 4.10c). Furthermore, the efficiencies were higher than printed SM:PS based OLEDs with the low work function cathode (Ca/Ag). As previously reported, intermixing inert polymers with SM improves the film quality, therefore, reduces the current leakage during device operation[181]. So that, the device efficiency can be tuned accordingly. The gravure printed SMLEC with air-stable cathode showed a uniform luminescence over the whole pixel area as seen in figure 4.10d.

4.3 Conclusion

In this chapter, we focused on the gravure printing technique as an alternative method for the deposition of the active layers of small molecule based devices for their potential R2R applications in the future. The main advantage of this approach was to combine the benefits of the low molecular materials with high quantum efficiencies and the process advantages of the gravure printing technique. Adapting gravure printing to fabricate a small molecule (SM) based organic light-emitting diodes (OLEDs) were quite challenging due to the low viscosity of the inks and the aggregation of the SM in the solid film. However, we opportunistically printed SM by embedding it into high molecular weight polymers.

In the first part, we focused on the gravure printing of flexible SMOLEDs on a plastic substrate by mainly modifying the ink formulations. The active layer was composed of the green triplet emitter in a host-guest structure and ultra-high molecular weight polystyrene (UHMW-PS) binder. The UHMW-PS improved the rheological properties of the functional ink to a printable range. Since polystyrene was an electrically inert polymer, it did not affect the electrical or optical properties of the emissive material. Additional to that, small molecule aggregation was suppressed in the thin film. Various SM:UHMW-PS ratios in two different solvents were tested to adjust the ink viscosity, surface tension, and drying conditions of the fluid. Furthermore, the surface leveling time and the drying time were obtained for quantitative considerations of printing demodulation. The 20:3 and 20:4 w/w ratio of SM:UHMW-PS in anisole granted homogenous printed layers which then suited as active layers in the device stack. The fabricated flexible SMOLEDs exhibited the maximum luminance over 850 cd/m^2 with a turn-on

voltage of ~ 3.5 V and the maximum efficiency of 7.7 cd/A at 13-14 V. However, encapsulation of air-sensitive cathodes remained an obstacle. So that, we further considered the applicability of this technique for another device concept, namely light-emitting electrochemical cell (LEC).

In the second part of this chapter, we checked on the feasibility of the gravure printing technique for small molecule based LECs. The active layer was composed of the same small molecule that was embedded into a high molecular weight polymethyl methacrylate (PMMA). PMMA performed as a polymer matrix, as well as an ion-solvating polymer for ionic species to form the solid polymer electrolyte (SPE) for LECs. $TBABF_4$ was engaged as the salt additive in SPE. We altered printing process parameters while keeping the ink formulation constant. Four different printing plates with varying gravure cell parameters, by the meaning of line screen and tone values, were implemented. We modified the active layer thickness and morphology of the films accordingly. Relatively high line screens with high tone values resulted in more homogenous and sufficiently thin layers to serve as the active layer of LECs. The printed SMLECs bearing air-stable cathodes showed the maximum luminance of ~ 8000 cd/m^2 with a turn-on voltage of ~ 5 V and the maximum efficiency of around 9.8 cd/A at ~9.5 V.

In brief, the gravure method was successfully adapted for the printing of thin layers of the small molecule by either controlling the process parameters or ink formulations. The results demonstrated the potential use of gravure printing for the fabrication of small molecule based electroluminescent devices.

Chapter 5
Hybrid device architecture for color-tuning in electroluminescent devices

This chapter focuses on understanding the working mechanism and optical-electrical behavior of a novel hybrid device that was suggested for color-tuning by our group. The hybrid architecture was composed of a single component LEC layer deposited on top of a conventional OLED. The LEC ensured a sufficient electron injection from an air-stable cathode into the emissive layer while serving as a second emissive layer. The dual color emission was detected as a result of simultaneous light output from two emissive layers. A straightforward color tuning was obtained by altering the thickness of LEC. The presented results showed that the proposed hybrid device structure herein could be potentially utilized to achieve white light emission from solution processed polymer electroluminescent devices with air-stable cathodes.

The findings of completed work in this section were published in the *Journal of the American Chemical Society (ACS) Applied Materials and Interfaces* in collaboration with Dr. Martin Petzoldt and Dr. Manuel Hamburger in the group of Prof. Uwe Bunz at Heidelberg University[186].

5.1 Introduction and aim of the work

Lighting consumes almost 1/5 of the worldwide electricity production and entails 1900 million ton of carbon footprint per year[13]. Hence, in recent years, there is a robust global momentum towards more energy efficient lighting by switching from halogen to LED bulbs. OLEDs are new energy saving and environmentally friendly form of solid-state lighting (SSL). In comparison to LED, OLED technology offers thin, flat, bendable, flexible properties for innovative design purposes. However, OLEDs still have lack of performances comparing to LEDs. Efficacy of the OLED luminaires usually ranges from 21 to 58 lm/W, and a new generation of OLED panels has appeared on the market in mid-2017, with panel efficacies of 60 lm/W[187]. Once the lifetime and performance issues are solved, OLEDs can compete with LED counterparts, due to the several advantages mentioned above.

Besides the energy consumption issues, artificial light sources play an essential role in our daily lives. Sunlight has a strong influence on the circadian rhythm of humans, which means that it regulates the sleeping hours and affects human psychology as a result[188]. For instance, in Nordic countries people suffer from lack of sunlight during the winter period, so that phototherapy lighting panels have been installed at bus-stops in Sweden to support metabolic rhythms and psychological conditions of people[189]. A high color quality light source play a decisive role in mental health and is desirable to ensure a high quality of life. The quantitative physical measures of the luminaire, e.g., horizontal or vertical illuminance, luminance ratio and correlated color temperature, CCT are considered[190]. For instance, CCT of the artificial light source is characterized by cooler light colors, and thus a minimum color temperature of 4000-5000 K [188]. OLEDs supply visual comfort by the soft almost horizontal light distribution along the panel, in comparing to LEDs that have sharp vertical illuminance[187].

White light-emitting diodes (WOLEDs) have gained particular attention due to their potential applications in display and SSL technology[28], [29]. WOLEDs can perform as a backlight with red-green-blue (RGB) color filters on top in display technology. Developments in display technology also benefit white SSL. However, as opposed to pixilated OLEDs designed for RGB

displays, OLEDs as luminaire source is meant to approximate a blackbody spectrum and a high emission intensity across the entire surface[187].

In the last decade, different approaches and techniques have been used to achieve white light and multicolor emission from OLEDs. Particularly, WOLEDs based on polymers (WPLEDs) allow solution processing methods such as screen and ink-jet printing to reduce manufacturing costs[134], [191]. However, the most efficient results have been obtained from OLEDs with complex, multilayer architecture by sequential deposition of the organic layers in vacuum[65]–[67]. Despite tremendous efforts in solution processed multilayer PLEDs by printing, the necessity of low work-function cathodes remains an obstacle[6]. Recently, solution-processed layers have been engaged as interlayers to enhance device efficiency of WOLEDs [192], [193]. The polymer interlayers reduced the work function of the metal cathode, leading more efficient charge injection of the carriers into the active layer of the device.

Searching for an alternative method in the direction of charge injection from stable cathodes led us designing a hybrid device architecture. In this chapter, an alcohol-soluble polycationic blue light-emitting polymer (PFNCl) was coated as the second emissive layer of the conventional polymer OLED. PFNCl acted as a single layer light-emitting electrochemical cell (LEC) to form electric double layers at the interfaces. Thus, the hybrid structure allowed charge injection from the air-stable cathode and additionally color tuning in the overall emission of the device. We investigated the photophysical and electrochemical properties of the newly synthesized polyfluorene derivative by using steady-state spectroscopy and cyclic voltammetry techniques. Furthermore, we tested PFNCl in a single component LEC device stack to characterize the electrochemical cell behavior and blue emission performance. After that, the bilayer devices were built by varying the thicknesses of PFNCl layer on top of Super Yellow (SY). The hybrid device comprising an Ag cathode exhibited operating voltages of ~ 6 V. And depending on the PFNCl thickness, different color emission ranging from yellow-green (x = 0.39, y = 0.47) to the edge of the white emission region (x = 0.29, y = 0.4), were obtained according to the Commission Internationale de l'Eclairage (CIE) 1931 chromaticity diagram.

5.2 Results

5.2.1 Photophysical and electrochemical properties

The optical characterization of the materials is crucial for better understanding and interpreting their optoelectronic devices. The absorption and fluorescence of PFNCl and Super Yellow (SY) were obtained in solution, and the spectra are presented in figure 5.1a. PFNCl exhibited a maximum absorption at 402 nm and an emission peak at 424 nm. The optical energy band gap, 2.92 eV was calculated from the onset wavelength of the absorption spectrum and using the following formula

$$\lambda_g\,(\mathrm{nm}) = \frac{hc}{E_g} = \frac{1241}{E_g(eV)}$$

, where *c* donates the free-space light velocity and the photon energy hv usually equals the band gap E_g (*h*, Planck's constant; and *v* light wave frequency). Correspondingly the maximum light wavelength λ = c/v is equal to the band gap wavelength.

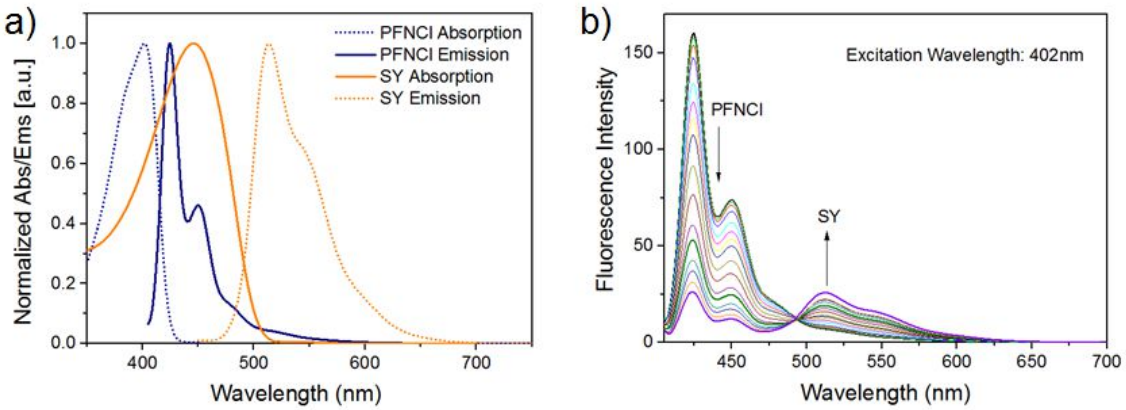

Figure 5.1 Normalized absorption and photoluminescence spectra of PFNCl and SY solutions (10^{-8} M) in chloroform (a). Förster resonance energy transfer (FRET) data for PFNCl-SY (b). The spectrum of PFNCl (1.0×10^{-6} M) was recorded at each time after adding of 50 µL SY solution of 2.0×10^{-8} M (at excitation wavelength of 402 nm, λ_{ex}=402 nm).

SY polymer showed maximum absorption at 446 nm and emission at 512 nm. The broad spectral overlap between the emission spectrum of PFNCl and the absorption spectrum of SY suggest that a probable energy transfer may take place between PFNCl (donor) and SY (acceptor), underpinning the color tuning in the emission of the bilayer device. Therefore, Förster-type energy transfer (FRET) between PFNCl and SY was investigated in solution by photoluminescence (PL), and the result is presented in figure 5.1b. The fluorescence quenching of PFNCl solution was observed when the SY concentration was increased in solution. An enhancement in PL intensity of SY at 512 nm and reduced intensity of PFNCl at 424 nm and 450 nm confirmed an efficient FRET. The PL data represents the non-radiative energy transfer from donor to acceptor molecules in solution. We will briefly touch on this subject in the device characterization of bilayer devices in section 5.2.3.

The electrochemical behavior of the materials is usually obtained to define their energy levels. Additional to that, for specific material compositions such as polyelectrolytes, the electrochemical stability at specific voltage rates is the key focus to eliminate undesired electrochemical side reactions during device operation. The electrochemical behavior of PFNCl was investigated in solution by cyclic voltammetry (CV) using ferrocene as the internal reference redox system (Figure 5.2a). The CV data were obtained to estimate the redox potentials and accordingly the energy levels of PFNCl. The energy of the highest occupied molecular orbital (E_{HOMO}) and the lowest unoccupied molecular orbital (E_{LUMO}) levels were calculated from the onset value of the oxidation and reduction potentials vs. ferrocene/ferrocenium (Fc/Fc^+) on the CV data, and assuming the energy level of Fc/Fc^+ to be 5.1 eV below the vacuum level following the empirical equations[163]. In this system, the potential value of ferrocene is 0.40 V versus SCE in ACN.

$$\mathbf{E_{HOMO}} = -[(E_{ox})_{on}+5.1]$$

$$\mathbf{E_{LUMO}} = -[(E_{red})_{on}+5.1]$$

The HOMO and LUMO energy levels and the electrochemical band gap of PFNCl were determined to be -5.56 eV, -2.85 eV, and 2.71 eV, respectively. The maximum peak potentials were recorded at 0.73 V for the oxidation and -2.44 V for reduction potentials. During the anodic scan, we detected irreversible oxidation with the onset potential at 0.46 V. At the cathodic region; we observed a reversible reduction process with an onset potential of -2.25 V.

A thin film of SY coated Pt working electrode (active area = 1 cm^2) was employed for CV measurement. Figure 5.2b shows the electrochemical reduction and oxidation of SY with the maximum peak potentials of +0.58 V and -2.5 V, respectively, versus Fc/Fc^+. The onset of the oxidation and reduction potentials were obtained as +0.35 V and -2.15 V, respectively. The nonreversible redox peaks arose from the quick dissolving of SY film in acetonitrile after doping. The HOMO and LUMO levels of SY were calculated using the above equations and found to be -5.45 eV and -2.95 eV, respectively and the band gap of SY was defined 2.5 eV.

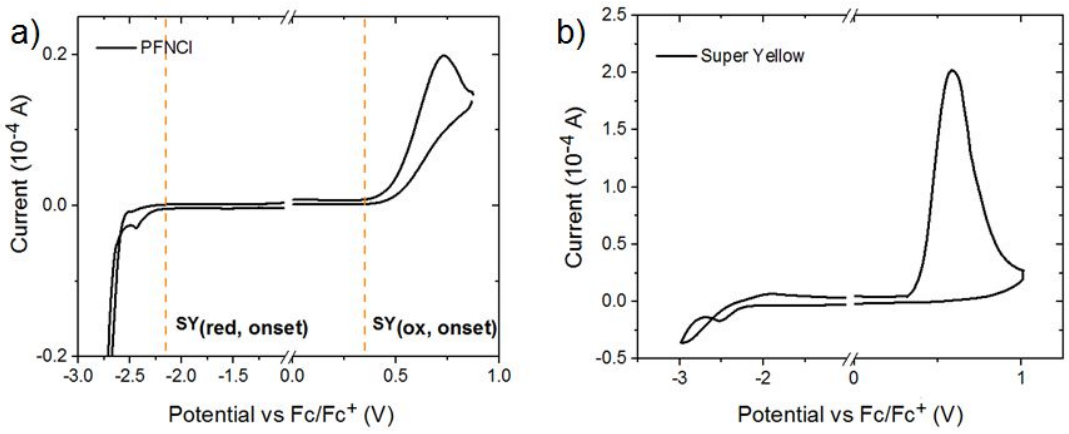

Figure 5.2 Cyclic voltammograms of PFNCl (a) and SY (b) in reduction and oxidation processes.The dashed lines (a) represent the p and n doping potentials of SY.

5.2.2 Single component LEC

Polyfluorenes (PFs) are the most extensively explored wide band gap materials in electroluminescent devices, due to their high photoluminescence (PL) quantum efficiency and

good chemical and thermal stability [191]. Amino-/ammonium-functionalized polyfluorenes (PFNs) have been successfully utilized as the electron injecting and transporting layers in OLEDs[192], [193]. They are usually soluble in polar solvents allowing wet-deposition on top of organo-soluble polymeric layers, resulting in the solution-processed multilayer device structure. PFNSs have been also performed in single active layer LECs[119], [194], [195]. The mobile ions within their structure are responsible for the electrical doping of the active layer, so that enables efficient charge injection from electrodes regardless of their work-function.

In our work, we first employed PFNCl in a single-component polymer light-emitting electrochemical cell (PLEC) to investigate its electrochemical doping and electroluminescence character. A single layer of PFNCl was deposited on the ITO glass or PEDOT:PSS coated ITO glass. The current density-voltage-luminance (J-V-L) characteristic of both devices is shown in figure 5.3a-b, where the inset images are attributed to their device architectures. The single active layer device showed a turn-on voltage of 7.1 V and the maximum luminance of 150 cd/m^2 at ~10 V. The device comprising PEDOT:PSS as HTL exhibited the higher luminance of ~550 cd/m^2 at 8 V with a turn-on voltage of 3.8 V, due to possibly more balanced charge transport of injected carriers. The inset image of figure 5.3b presents a photograph of the single component PLEC in operation.

The electroluminescence (EL) spectra and the time-dependent voltage behavior of the device bearing HTL are shown in figure 5.3c. **T**he device exhibited a maximum luminescence peak at 434 nm with the CIE color coordinates of x = 0.19 and y = 0.16. There are only a few examples in literature related to deep blue emissive LECs[194]–[196], due to the broad energy band gap of the blue emissive materials. The band broadening at longer wavelengths (also seen in PL spectrum, Figure 5.1) may attribute to the polymer aggregation due to the ionic moieties on the side chains[195]. The inset of figure 5.3c presents the time-dependent voltage characteristics of the device. We conducted the measurement during continuous device operation at an applied constant current density of 50 mA/cm^2. The device showed a typical LEC behavior with a slow response time that indicates the time required for slow ion motion towards the electrodes (see section 2.3.3). So a voltage drop according to suggested doping models (see section 2.3.2.1)

was likely associated with the formation of electrical double layers (EDL). A potential reduction is a typical phenomenon in LEC operation that may occur at the electrode interface[107] or in bulk [103] depending on the doping model. Since the electrochemical doping model is not relevant to our work, the position of the potential drop is not considered herein. The EDL reduce the injection barrier at the electrode interface, allowing sufficient charge carrier injection from electrodes regardless of their work-function.

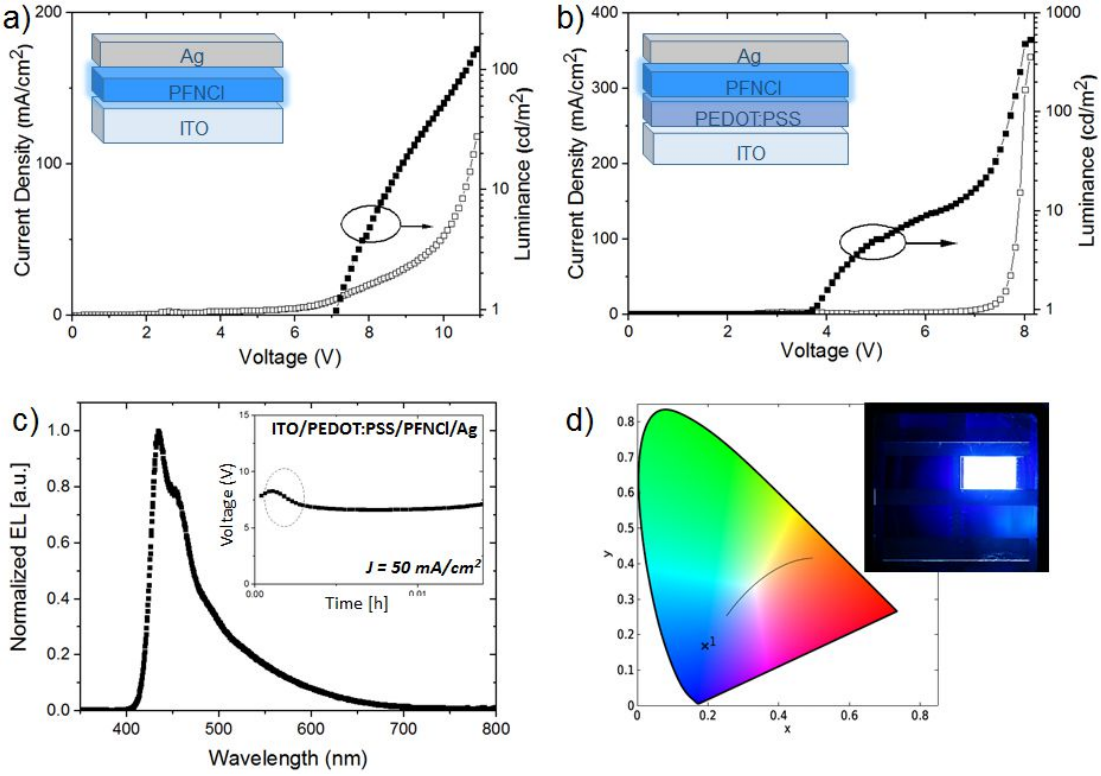

Figure 5.3 Current density-voltage-luminance characteristics of PFNCl single layer LEC (a) and PFNCl LEC comprising HTL layer (b). Inset images exhibits the corresponding device architectures. Electroluminescence, time-dependent voltage characteristics (inset, c), and CIE color chromaticity diagram of PFCNl LEC with HTL layer (d). A photograph of device under operation (d). (*at a constant current density of 50 mA/cm^2).*

5.2.3 Bilayer device concept

In contrast to inorganic counterparts, color tuning in OSC based electroluminescent devices is relatively easy and straightforward. Band gap tuning gives the opportunity to design a large number of OSC materials by chemical synthesis[89]. Device engineering also benefits from it for

developing novel device concepts by changing energy level alignment or energy transfer mechanisms[197].

Different approaches have been made to obtain white emission and color-tuning in polymer based electroluminescent devices. For instance, researchers detected white light from single copolymers that have simultaneous RGB emission[89], [119], and two-color radiation by varying the applied voltage[81]. In another example, color-tuning was achieved by optical doping in a host-guest system comprised of quantum dots and polymers[97]. In general concept, three primary colors RGB or two complementary colors should be applied to achieve the white light. A direct approach for WPLEDs is blending two or three polymers in the active layer[29]. However, in a blended system, intrinsic phase separation may lead the decrease of color stability and device lifetime which are essentials for display and SSL applications.

In our work, two emissive polymers were engaged in the separate layers of the bilayer device model. The second layer material was selected in such a way that allowed sequential deposition without dissolving the underlayer. So, a layer of alcohol-soluble PFNCl with various thicknesses was deposited on top of an SY layer to form double emissive layers (EMLs). PEDOT:PSS was coated on the ITO glass to employ as HTL. The device stack was completed with the evaporation of air-stable cathode. The optoelectrical and time-dependent voltage data of the bilayer hybrid devices are presented in Figure 5.4. Figure 5.4a-b presents the current density-luminance characteristic versus voltage. We obtained the turn-on voltages ranging between 4 and 8 V with a maximum luminance intensity in the range of 500-550 cd/m^2 for the bilayer device configurations. The increase in turn-on voltage was related to the thickness increase of the PFNCl layer. Detailed device characteristics for bilayer devices are presented in Table 5.1 and compared with the single layer of PFNCl and SY device results.

The time-dependent voltage characteristics were measured at a constant current density of 20 mA/cm^2 as shown in figure 5.4c. The observed initial decrease of the operational voltage for bilayer devices may attribute to the electrochemical doping of PFNCl layer during device operation. Voltage drop is a typical LEC phenomenon, which was also observed for single layer PFNCl device as detailed in the previous section. During galvanostatic operation at a set current,

a decrease in voltage by time is usually considered as a proof of in situ electrochemical doping in LECs[180]. The same drop was not realized for the single layer SY OLED on the graph, and we attributed this difference as distinguishing factor between two device types. Figure 5.4d illustratively shows the device configuration and corresponding energy level diagram of the hybrid architecture. The HOMO and LUMO energy levels of PNFCl and SY were determined as previously explained in section 5.2.1.

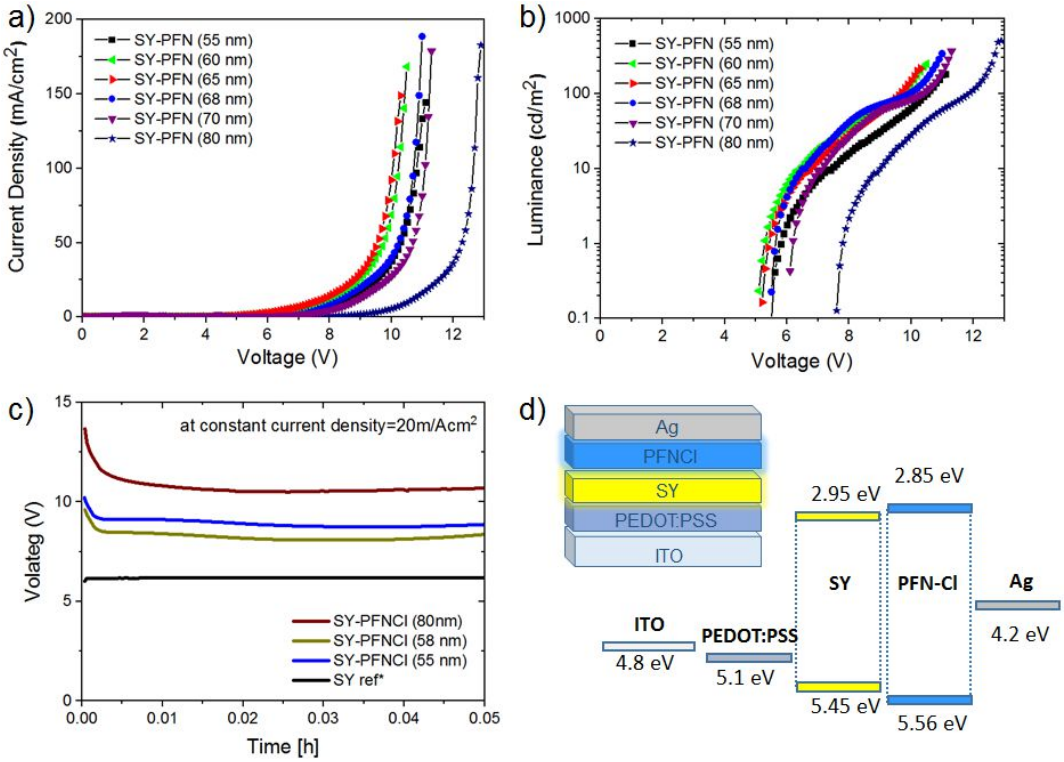

Figure 5.4 Current density-voltage (a) luminance-voltage characteristics (b), time-dependent voltage characteristics (c) of the bilayer devices. Schematic illustration of device architecture and corresponding energy level diagram (d). (*at a constant current density of 20 mA/cm²).*

Figure 5.5a presents the electroluminescence (EL) spectra of the hybrid devices and a single layer PFNCl LEC and SY OLED as the reference devices. The emission wavelengths of the hybrid devices were extended from 400 nm to 750 nm. The EL data proves the contribution from both

emitting polymers in total emission as a result of electron transport through the PFNCl into the SY layer. We suggested that only a partial input from FRET may assist the color-tuning within an overall device emission. The application of FRET for large macromolecules is restricted[162], due to an upper distance limit of ~10 nm. In our case, the minimum thickness of the PFNCl layer was ~55 nm that is far beyond the probable Förster radius. Thus, the blue emission band from PFNCl layer were visible for all hybrid devices and contributed to the total electroluminescence. An increase in the layer thickness of PFNCl resulted in a more significant blue emission band producing color-tuning.

A blue-shift between 500 and 550 nm was observed in the emission band of SY as seen on EL spectra of hybrid devices. Such shifts were reported before in the literature for the EL and PL spectra of SY in the bilayer device architectures[198]. In their system, the electroluminescence was blue-shifted from the bulk emission of super yellow, with the emission wavelengths depending on the SY concentration. In our study, layer intermixing might take place after depositing PFNCl layer from 2-methoxy ethanol on top of SY, leading to a similar spectral shift as reported in the literature.

The change in the emission color of bilayer devices can be seen more clearly in the CIE coordinates diagram in Figure 5.5b. The arrow on the graph indicates the increase of PFNCl layer thickness in hybrid device configuration. The color coordinates shifted from the yellow emission *(x:0.39, y:0.47)* towards yellow-green *(x:0.34, y:0.44)* with increasing the thickness of PFNCl. Finally, the emission reached to the edge of the white-light emission zone *(x:0.29, y:0.40)* when the thickness of the PFNCl was the maximum. Today, the artificial systems are generally designed to maximize their light output and energy efficiency according to the sensitivity of the photopic vision, which peaks in the yellow-green band (i.e., at 555 nm) [188].

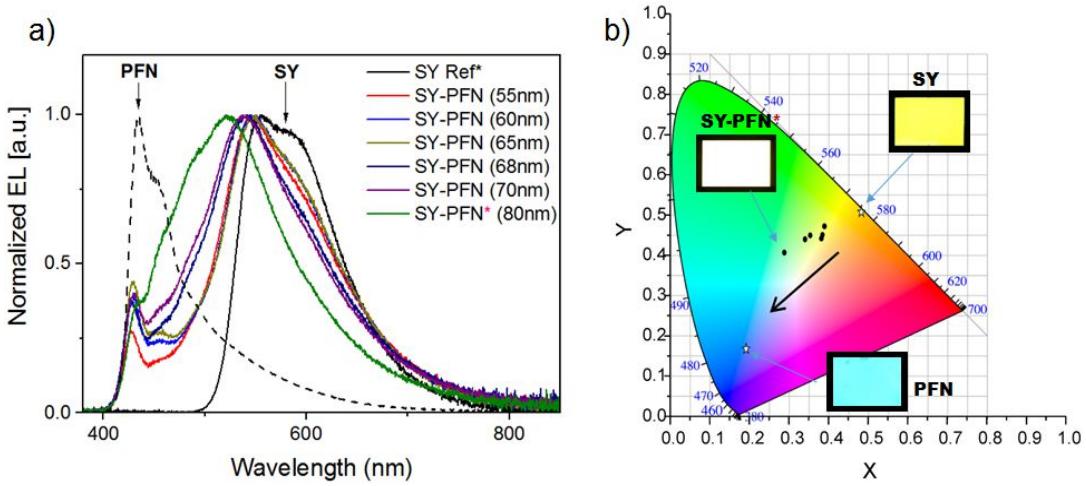

Figure 5.5 Electroluminescence spectra (a) and CIE color coordinates (b) of single and bilayer devices that was measured at a current density of 100 mA/cm^2. Inset images (b): photographs of different device pixels under operation.

A summary of CIE coordinates, color rendering index (CRI) and color chromaticity temperature (CCT) values, as well as the maximum EL wavelengths of all bilayer devices, are presented in Table 5.1. CCT levels were obtained at the range of 4300-6900 K with a CRI of ~ 70 for all hybrid devices. The minimum color temperature of 4000-5000 K is required for artificial lights, where the CRI is 70-90 the lowest[188]. Color temperatures over 5000 K are considered as *cool colors* (bluish), due to the higher proportion of blue emission in the light spectrum compared to sunlight which is defined *warm-white* light source (2500-5500 K)[190]. Therefore, the light emission of hybrid 1 device might be considered as cool-white light with the CCT level of 6980 K. The yellow-green emission of hybrid 4-5 devices shifted to yellowish-green color for hybrid 3-2 with thickness enhancement of the PFNCl layer. In figure 5.6, photographs of hybrid device pixels at low operating voltages ~7-8 V indicates the color change in the device emission.

Figure 5.6 Photographs of hybrid device pixels under operation.

Table 5.1 Summary of the device characteristics for single and bilayer devices:

Device	PFNCl Thickness (nm)	Turn on Voltage (V)	Max. Current Density (mA/cm^2)	Luminance* (cd/m^2)	Max. EL λ (nm)	CIE 1931* (x:y)	CRI	CCT [K]
Hybrid1	80	7.8	183	294	521	0.288 : 0.407	67.49	6980
Hybrid2	70	6.2	178	227	540	0.34 : 0.44	70.24	5316
Hybrid3	68	5.7	188	215	541	0.354 : 0.45	70.22	5008
Hybrid4	65	5.5	149	158	550	0.382 : 0.442	69.09	4343
Hybrid5	60	5.3	168	179	544	0.385 : 0.451	68.01	4322
Hybrid6	55	5.8	144	141	546	0.39 : 0.472	67.35	4310
PFNCl LEC	65	3.8	342	164	434	0.192 : 0.167	59.17	-
SY OLED	0	4.7	350	915	556	0.483 : 0.508	45.84	-

* at a current density of ~ 100 mA/cm^2

5.3 Conclusion

In this chapter, we focused on the color-tuning and white light-emission from the light-emitting devices bearing air-stable cathode. In this context, we demonstrated a hybrid device architecture by combining unique LEC and OLED features in a single unit cell configuration. A novel emissive polyfluorene derivative, PFNCl performed in a single component LEC layer on top of a conventional super yellow OLED stack. We considered the photophysical characterization of both emissive polymers for probable energy transfer at the interface of two emissive layers in the bilayer device stack. Electrochemical studies were carried out to define the energy level alignment which allowed sufficient charge transport at the donor-acceptor interface during device operation.

The bilayer devices had the maximum luminance intensity of 500-550 cd/m^2 with the turn-on voltages between 5-8 V depending on the layer thickness of PFNCl layer. Independent of the thickness variations and the applied voltage range, all devices exhibited a combined electroluminescence response under the influence of two emissive layers, where the yellow component from neutral polymer SY dominated the overall emission. However, by increasing the thickness of PFNCl, the blue component of the electroluminescence became more prominent, giving rise to a color change in total radiation. The CIE color coordinates shifted from the yellow-green region to the white-light region of the CIE diagram. We obtained high color temperatures spanning from 4300 to 6900 K for all hybrid devices with a color rendering index of ~ 70.

In short, ionically functionalized PFNCl performed as both the electron injection layer and color conversion element. The presented hybrid device structure can be potentially used to achieve electron injection as well as color-tuning in solution processed electroluminescent devices bearing air-stable electrodes.

Chapter 6
Biodegradable polyelectrolytes for light-emitting electrochemical cells

Increasing environmental challenges and energy demand led us searching efficient, low-cost and sustainable electronics. One of the prospects is to use natural-based renewable materials, so-called “green” materials in sustainable technologies. In this context, biopolymers have potential applications in the field of organic electronics as a means to develop biodegradable and biocompatible optoelectronic products.

In this chapter, we utilized natural and naturally derived biopolymers as ion-solvating polymers in the emissive layer of light-emitting electrochemical cells. We tested different biopolymer based solid electrolyte systems (SPE) with various salt concentrations and obtained related ionic conductivities. The electrochemical stability window of SPEs was considered in to define the device stability of bio-based LECs. Additionally, we investigated the morphology effects of emissive layers on the device performance.

Parts of this work related with DNA-based LECs will be submitted for publication.

6.1 Introduction and aim of the work

Electronic waste (e-waste) is a global issue that contributes to environmental pollution and increases hazardous risks on public health, specifically in underdeveloped countries, where such waste is usually exported[10]. The minimum annual growth rate of e-waste is expected to be 4-5%, while only 15% of the total is actually being recycled[11]. Uncontrolled recycling procedures also give rise to harmful health effects, when workers are exposed to toxic elements in e-waste[12]. Existing policies and suggested makeshifts for reducing the e-waste hazards on public health[12] would not be sufficient to solve these problems in the long-term.

Today, one of the most important arguments in the field is to replace synthetic polymers with biopolymers in photonic and organic electronic applications[1] in the direction of using disposable electronics instead of existing electronic products in the future. Biocompatible electronics are considered to develop much faster than biocompatible photonics and have become more feasible, specifically in healthcare applications[199]. There is a limited number of research reports using conventional OLEDs in contact with biological matter. Gather et al. very recently obtained promising results by implementing OLED microarrays for optogenetics[200] However, as we pointed out in previous chapters, OLEDs are sensitive to water and humidity, and therefore, they are vigorously sealed. In the case of any leakage of nonbiocompatible components, the materials could be potentially toxic to the host. Further innovations through biocompatible and implantable photonic devices may offer biocompatible, bioresorbable products for healthcare monitoring, sensing, and light-activated therapies. Biodegradability and bioresorbability of the implemented device would eliminate the need for removal after use and would not harm the host tissues.

Over the last decade, biomaterials have been utilized particularly in organic light-emitting diodes as comprehensively reviewed by Costa et al.[201]. Recent activities involve the implementation of these materials in different device parts such as substrates, electrodes, and active layers with different functionalities (e.g., emissive, charge injection or transport layers). In 2000, You et al. conducted the first work in the field of bioinspired OLEDs by mimicking the

bioluminescence of jellyfish[202]. Different biomaterials have been engaged in the active layer of OLEDs, such as fluorophores[202], natural emitters[203], deoxyribonucleic acid (DNA)[204], [205], DNA nucleobases[206], proteins[207], vitamins[208], etc. Additionally, silk fibroin[209] and eumelanin[210] were tested as electrode materials in OLEDs. Chitin[211], cellulose[206] and cellulose-based paper[139] substrates have been utilized for OLEDs. However, an additional treatment is needed for rough substrates such as paper or silk fibroin due to the requirement of smooth surface and thin layers for an efficient light emission[139], [209]. In this context, LECs can be a good alternative device concept with their high tolerance for the substrate roughness and active layer thickness, which allow for different processing techniques. In 2015, spray-deposited flexible and light-weight LEC on-paper devices were demonstrated[212]. The device featured a uniform light-emission with a luminance intensity of 200 cd/m^2 and efficacy of 1.4 cd/A. Nevertheless, up to date, biodegradable and biocompatible materials have not been thoroughly investigated for LECs, except a few examples recently reported by our group. In this context, we tested a range of biodegradable polymers as solid polymer electrolytes (SPE). We will summarize them in the following section.

In this chapter, we will focus specifically on gelatin, DNA and DNA-cetyltrimethylammonium (DNA-CTMA) based SPE, which are soluble in aqueous or organic solvents. Different salts and plasticizers at varying ratios were added in the SPEs to enhance the ionic conductivity. The electrochemical stability windows of SPEs were determined to define the electrochemical side reactions during device operation. After optimizing the ionic conductivity of bio-based SPEs, we implemented them in the active layer of blue and yellow emissive LECs. We blended the SPEs with commercially available, a water-soluble blue emitter, poly(2,5-bis(3-sulfonatopropoxy)-1,4-phenylene, disodium salt-*alt*-1,4-phenylene) (PPP) and an organo-soluble yellow emitter, namely Super Yellow (SY). The optoelectrical and lifetime characteristics of the electrochemical cells were obtained. Furthermore, morphology studies were carried out to characterize the phase separation between the SPE and emissive polymers, as well as aggregation tendency in the solid film, which play a critical role on the device performance.

6.2 Results

A key component of LECs is polyelectrolytes that combine the properties of soft plastic materials and ionic conduction. The polymer chain serves as the scaffold medium and the compensating ion for the counter ions. The basic principle of ionic conduction and the role of ionic conductivity on LEC transients were summarized previously in section 2.3.3. Recently, Mindemark and Edman comprehensively reviewed the importance of polyelectrolytes on device performance[117].

Polyelectrolytes are generally divided into two groups, polyanions and polycations, each type selectively transports the cations and anions, respectively. Up to date, different polyanions and polycations have been implemented in the active layer of LECs as ion-solvating components[149], [150], [213]. The most commonly used electrolyte systems in LECs are alkali metal salts, which are dissolved in ether-based ion transporters[117]. By having a better understanding of the working principle of LECs, researchers can thus focus on designing new polyelectrolyte system. Identifying the solid polymer electrolyte parameters such as (i) ionic concentration, (ii) electrochemical stability window, and (iii) phase separation with the emissive materials will play a critical role in the device performance.

6.2.1 Water-soluble solid polymer electrolytes

6.2.1.1 Gelatin

As the first step of integration of biomaterials in LECs, we tested the natural biopolymer "gelatin" as an ion-conducting polymer in the active layer of LECs. Gelatin is abundant, inexpensive, and biodegradable, while it is also a non-toxic material that is widely used in the food industry. Gelatin-based edible films and coatings are found to be quite advantageous for degradable active packaging applications[214]. Since it is produced from leftovers in meat processing plants, therefore, it is sustainable a product.

As a biocompatible polymer, gelatin has been commonly utilized for drug delivery and tissue engineering applications[215]. In 2010, it was used for the first time in organic electronics as a

substrate through the fabrication of fully biodegradable OFETs on hard gelatin drug capsules[1]. In another example, solution processed gelatin was utilized as a gate dielectric in OFETs[157]. The layer thickness of a casted gelatin was ca. 1140 nm. Recently, Pawlicka and coworkers elaborated on gelatin gel polymer electrolytes (GPE) for their potential use in electrochromic devices (ECD) and lithium-ion (Li-ion) batteries. In their work, they poured a hot solution on a petri dish to form 0.01-0.5 mm thick membranes[160]. High ionic conductivity results combined with the transparency of the electrolyte, merited the further investigation of the material in optoelectronics. Despite the new attributes provided by gelatin and its ionic conductivity, thus far, gelatin has not been used in LECs.

6.2.1.1.1 The film formation and ionic conductivity of gelatin based solid polymer electrolytes

In our work, sufficiently thin gelatin SPE layers were employed in the active layer of LECs. Relatively more bulky layers were deposited in metal-insulator-metal (MIM) structure to prevent shunts while measuring the ionic conductivity.

The film-forming steps in the procedure are illustratively explained in figure 6.1. Gelatin is a hydrophilic material that swells in an aqueous phase. Water molecules form hydrogen bonding with its functional groups along the chain (e.g., *carbonyl:* C=O, *amine:* N-H, *hydroxyl:* O-H, see the molecular structure in section 3.1.2). In this way, water molecules create linkages between the gelatin strands by disturbing the interchain hydrogen bonds in gelatin. Below 35-40°C gelatin swells up and can absorb 5-10 times its weight of water to form a gel. Above these temperatures, gelatin is unable to form interchain hydrogen bonds. In this study, gelatin powder was first dispersed in water and subsequently heated at ~ 50°C. Gel strength and viscosity gradually weakened upon prolonged heating in solution above 40°C[158]. The gelatin layers were directly spin-coated onto substrates from the hot solution and left to cool down at room temperature (below 35°C). Cooling below 35°C favored the aggregated state (mainly due to hydrogen bonds). After that, the layers were dried at 35°C for 24 hours to remove any water residue to stabilize the structure in its solid state. Gelatin macromolecules assumed the conformation of thin layers.

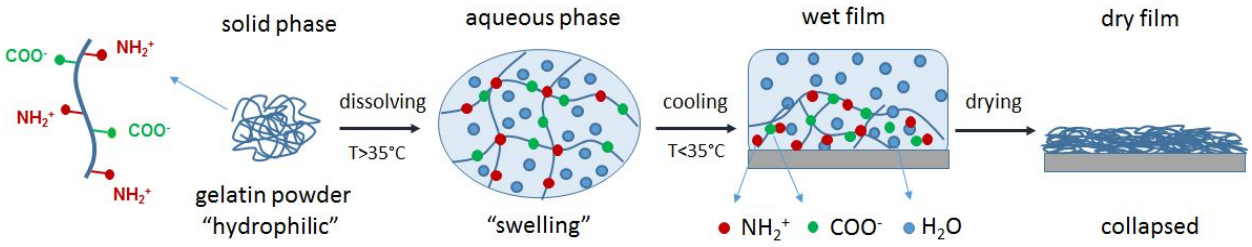

Figure 6.1 Illustrative representation for the preparation process of gelatin thin films.

Gelatin solutions were prepared with different total solid content. We utilized plasticizers, i.e., cross-linkers to control the thickness of the gelatin layers while tuning the ionic conductivity of the films. The solid concentration of solutions and their related film formations are summarized in table 8.1 in the appendix section. First, glutaraldehyde was added to the solution to change the mechanical strength of gelatin. Plasticizers are usually combined in gelatin to improve the flexibility and gel formation[160]. However, in our work, high solid concentrations with glutaraldehyde additive resulted in a hard gelatin or a viscous gel formation, which were insufficient for film casting. We used an 80 g/L of gelatin solution without cross-linker (produced in ~800 nm thick gelatin layers) and a 60 g/L gelatin solution doped with 3.3% wt with glutaraldehyde (~480 nm) to perform the ionic conductivity measurements. We previously reported the ionic conductivity of the layers that were doped with sodium chloride (NaCl) salt at varying ratios[216]. The ionic conductivities were obtained at the range of 10^{-8} S/cm for the gelatin:NaCl blends. However, partial aggregations were observed in solid films with a high ratio of dopant. Therefore, we utilized another salt for further research.

In this thesis, the pristine gelatin films were deposited from gelatin solutions with the concentration of 15 g/L and 30 g/L without cross-linker. The metal-insulator-metal (MIM) structure was utilized to determine the ionic conductivity of gelatin dielectric film by impedance spectrometry. Bohui Wang conducted the impedance measurements for gelatin based SPEs during her HiWi (Hilfwissenschaftler) work. The spin-coated gelatin SPEs were sandwiched

between a pre-structured ITO-glass and an Ag cathode. The thin layers of gelatin containing different amounts of salt dopant were prepared to improve the ionic conductivity. Potassium trifluoromethanesulfonate, (KCF_3SO_3) was engaged as a salt additive at various w/w ratios. The films with two maximum salt concentrations were further doped with another plasticizer, glycerin. Glycerin at varying weight ratios was utilized to improve the ionic conductivity of gelatin. It performed as a separating agent by crosslinking between gelatin strands and promoted higher mobility of ionic species through the polymer chain[160]. The Nyquist plots of impedance spectra are shown in figure 6.2. The bulk resistivity (R_b) was extracted from the related equivalent Debye circuits[126] of impedance data as explained in section 3.3.4.2. The ionic conductivity (σ_i) of the SPE was calculated using the following equation:

$$\sigma_i = d / (R_b A) \qquad (1)$$

, where *d* is the thickness between the electrodes, *A* is the area of the electrode and R_b is the bulk resistance. For each sample, the electrode area was 0.24 cm^2 (A), and film thickness differed (d).

The maximum ionic conductivity of gelatin based SPEs was obtained $5.51x10^{-8}$ S/cm for 1:1 w/w ratio of gelatin:salt without plasticizer and $8.31x10^{-9}$ S/cm for 1:0.75:0.35 w/w ratio of gelatin:salt:glycerin. The ionic conductivity was improved with the increased amount of salt in the blend. Furthermore, the glycerin amount was optimized at 1:0.35 w/w ratio of gelatin:glycerin mixture. Higher plasticizer amount above the optimized level of glycerin resulted in a reduced ionic conductivity. The summary of ionic conductivity and layer thicknesses for all blends can be found in table 6.1 and table 6.2.

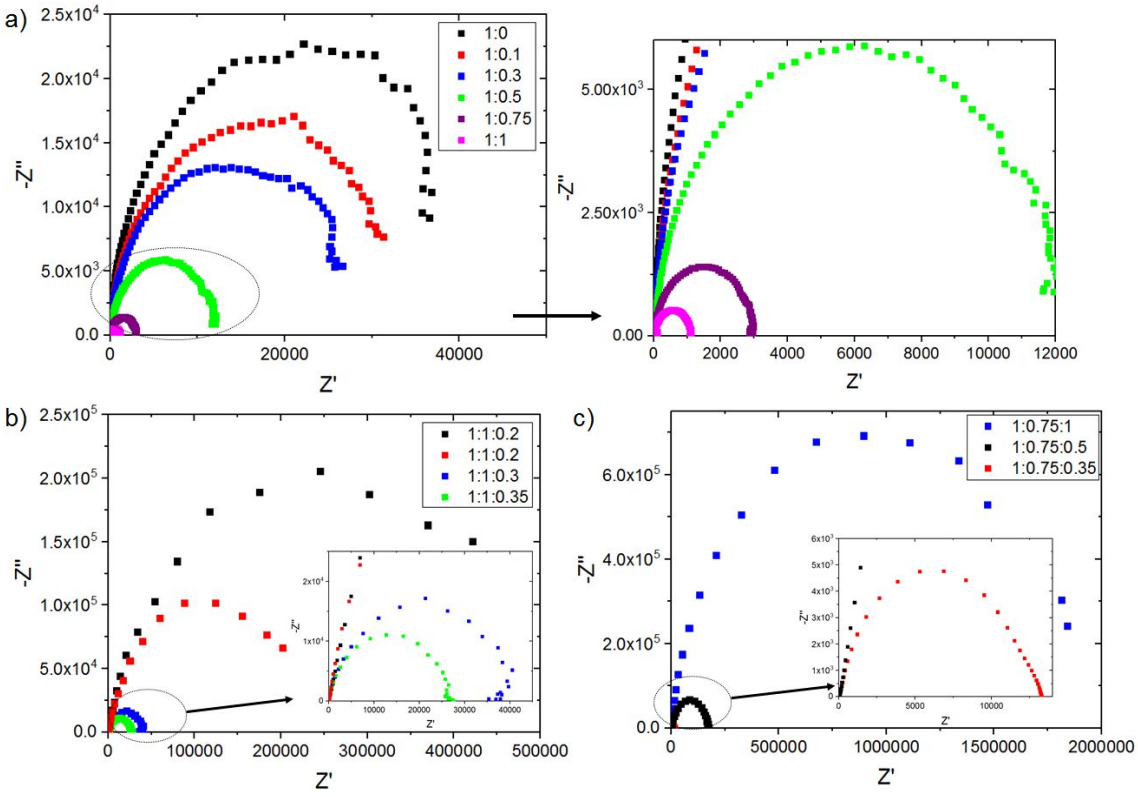

Figure 6.2 Nyquist plots of gelatin based SPE films with different salt ratio of Gelatin:KCF_3SO_3 [1:x] (a) and with varying plasticizer ratio of Gelatin: KCF_3SO_3:Glycerin [1:1:x](b) and [1:0.75:x](b). For all Nyquist plots, both the imaginary (-Z") and the real (Z') axis are expressed in ohm [Ω].

Table 6.1 The summary of ionic conductivity results for gelatin SPEs without plasticizer.

Gelatin:S[a)]	R_b [b)] [Ω]	Layer Thickness [nm]	σ [S/cm][c)]
[1:0]	36519	90	1.02×10^{-9}
[1:0.1]	33547	90	1.11×10^{-9}
[1:0.3]	26570	90	1.41×10^{-9}
[1:0.5]	11998	90	3.12×10^{-9}
	11943		3.13×10^{-9}
[1:0.75]	20493	100	1.82×10^{-9}
	9820		4.24×10^{-9}
	6446		6.46×10^{-9}
[1:1]	2954	100	1.41×10^{-8}
	756		5.51×10^{-8}
	1114		3.74×10^{-8}

[a)]S:KCF_3SO_3; [b)]R_b:bulk resistivity (ohm); [c)] σ=ionic conductivity

Table 6.2The summary of ionic conductivity results of gelatin SPEs with plasticizer additive.

Gelatin:S[a]:Gly[b]	R_b [c] [Ω]	Layer Thickness [nm]	σ [S/cm][d]
[1:0.75:0.35]	13286	265	8.31×10^{-9}
[1:0.75:0.5]	172735	265	6.39×10^{-10}
[1:0.75:1]	1840091	265	6×10^{-11}
[1:1:0.2]	459849	227.3	2.05×10^{-10}
	330355	227.3	2.86×10^{-10}
[1:1:0.3]	38189	227.3	2.47×10^{-9}
[1:1:0.35]	27563	227.3	3.43×10^{-9}

[a]S:KCF_3SO_3; [b]Gly:glycerin; [c]R_b:bulk resistivity (ohm); [d] σ=ionic conductivity

6.2.1.1.2 Gelatin based light-emitting electrochemical cells

Gelatin based SPEs were subsequently mixed with an electrically conducting emissive polymer at different ratios to form the active layer of LECs. A water-soluble blue emitter, poly(2,5-bis(3-sulfonatopropoxy)-1,4-phenylene, disodium salt-*alt*-1,4-phenylene), PPP was employed as the emissive component in the blend. The absorption and fluorescence spectra of PPP are shown in figure 8.2a in the appendix. PPP exhibited the maximum absorption at 340 nm and an emission peak at 409 nm.

The SPE:gelatin blends were sandwiched between the ITO-coated glass and an Ag cathode. The single layer of LEC was composed of gelatin:PPP:KCF_3SO_3 with and without plasticizer additive. The film thicknesses changed depending on the total solid concentrations. The optoelectrical characterization of gelatin based LECs is shown in figure 6.3. The light output was not detected for the reduced salt ratios, which were lower than 0.75 in the blends. The maximum luminance intensity of 1.2 cd/m^2 was obtained at ~8.5 V for the PPP:gelatin:salt:glycerin blend with a w/w ratio of 2:1:0.75:0.35. A non-uniform light emission over the pixel area was observed with a short lifetime of ten seconds (See the inset images of figure 6.3). All device results and thickness variations can be found in table 6.3.

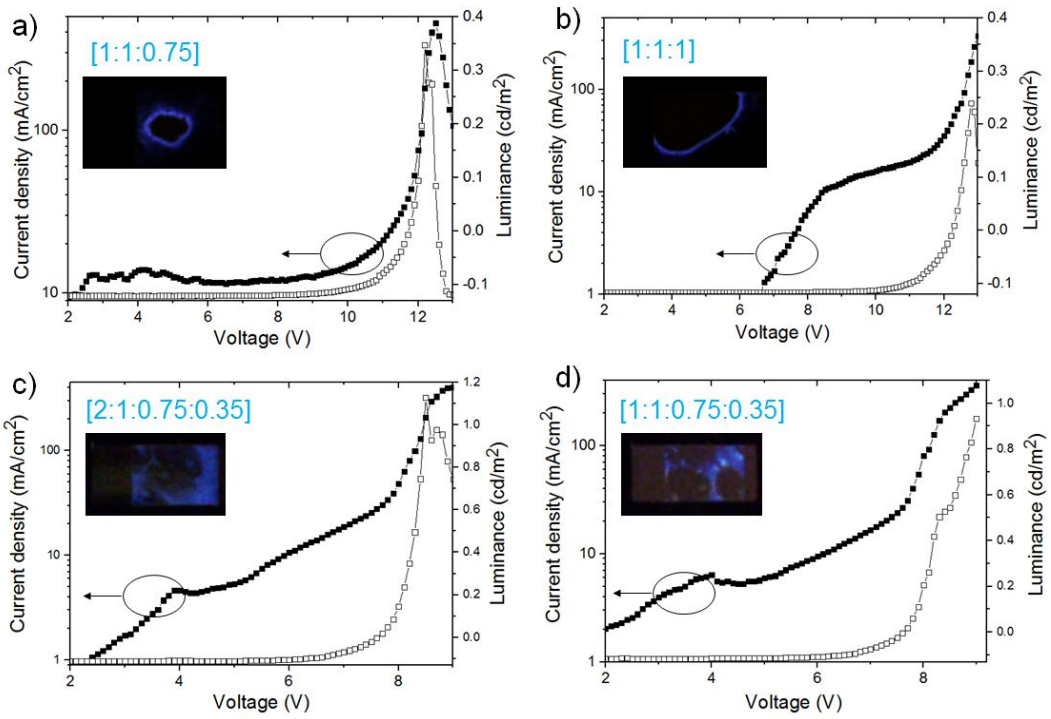

Figure 6.3 J-V-L characteristic of gelatin based LECs at varying w/w ratios of PPP:gelatin:salt, 1:1:0.75 (a), 1:1:1 (b),and PPP:gelatin:salt:glycerin, 2:1:0.75:0.35 (c), 1:1:0.75:0.35 (d). Insets: Photographs of corresponding LECs under operation.

Table 6.3 The device characteristics of gelatin based LECs.

PPP:Gelatin:S[a]:Gly[b]	V[c] [V]	L_{max} [d] [mcd/m²]	J [e] [mA/cm²]	C [f] [g/L]	Layer Thickness [nm]
[1:1:0.75:0]	12	350	500	41.25	120
[1:1:1:0]	12.7	240	400	45	130
[2:1:0.75:0.35]	8.5	1200	400	30.75	66
[1:1:0.75:0.35]	9	900	400	23.25	45

[a]S:KCF3SO3; [b]Gly:glycerin; [c]voltage at L_{max}; [d]max. luminance; [e]max. current density; [f]solid concentration.

Among many possible reasons that may account for the poor device performance, one could be that the absorption of water into the gelatin layer. The water inside the gelatin layer could be only partially removed in our work when considering the drying conditions (layers were dried at

35°C). The capacitance, i.e., the dielectric constant of the gelatin layer in MIM structure was found to be increasing in the case of high humidity and restricted the device operation in ambient air [157]. Therefore, the gelatin films were usually subject to a time-consuming annealing process. In our study, we postulated that unfavorable side chemical reactions, which affect the overall device performance, would be correlated with water residue in gelatin. Additional to that, the mechanical properties of gelatin were strongly temperature dependent. So that, difficulties in controlling the layer thicknesses of gelatin films resulted in batch to batch variations. Since the layer thickness was the bottleneck concerning device reproducibility, we decided to focus on different materials using the same device concept.

6.2.1.2 Deoxyribonucleic acid (DNA)

Among natural biodegradable materials, the science community has shown a great interest to DNA. It has drawn quite an attention specifically in the field of photonics and electronics, due to its high transparency, thin film processability, high thermal stability, and optical properties[217]. DNA is abundantly existing and renewable material. For instance, that can be easily isolated from the marine waste product by salmon processing[218].

As the pioneering work in optoelectronics, Grote et al. utilized marine-based DNA in non-linear optics[218]. Since DNA is soluble only in water, it was modified to its lipid complex (DNA-CTMA) via ionic exchange reaction to dissolve in alcohols[156]. After that, DNA has become very popular as a building-block material in the field of organic electronics over the last decade. DNA-CTMA was utilized as a thin film gate dielectric in OFETs and memory elements[219], [220]. DNA was also investigated in different layers with different functionalities in the active layer of OLEDs. For instance, it performed an electron blocking layer (EBL), or a combination of the hole transport layer (HTL) and EBL[221]. It was also used as an electron injection layer (EIL) in PLEDs[222]. Additionally, DNA was engaged in the emissive layer (EML) of OLEDs by intermixing DNA with fluorophores[204].

Water-soluble DNA and DNA-based polymers have been investigated as bulk materials in GPE and ion-conducting membranes for potential applications in electrochromic devices and Li-ion

batteries[160], [223]. As follow-up contribution, DNA-based layers have been utilized as HTM in dye-sensitized solar cells[224]. Recently, Kobayashi et al. demonstrated electrogenerated chemiluminescence (ECL) cell using an electrode that was modified with a DNA/$Ru(bpy)_3^{2+}$ hybrid film[225]. An orange-color ECL was observed from only the aggregated structures in the small area film. Although numerous applications of DNA have been demonstrated in optoelectronics, there is no report on the investigation of DNA as a polymer electrolyte in LECs up to date.

6.2.1.2.1 The conductivity of DNA

DNA has excellent potential for applications in organic electronic devices so that its conductivity has been extensively studied in the last two decades. The results have shown a dramatic change in the conduction behavior, such as an insulator, semiconductor, conductor, induced-superconductor depending on the DNA length, base sequence, temperature, and environment[226]. Understanding the conductivity of DNA is essential to interpret the data herein; therefore, we first take a close look on DNA structure first (See Figure 6.4).

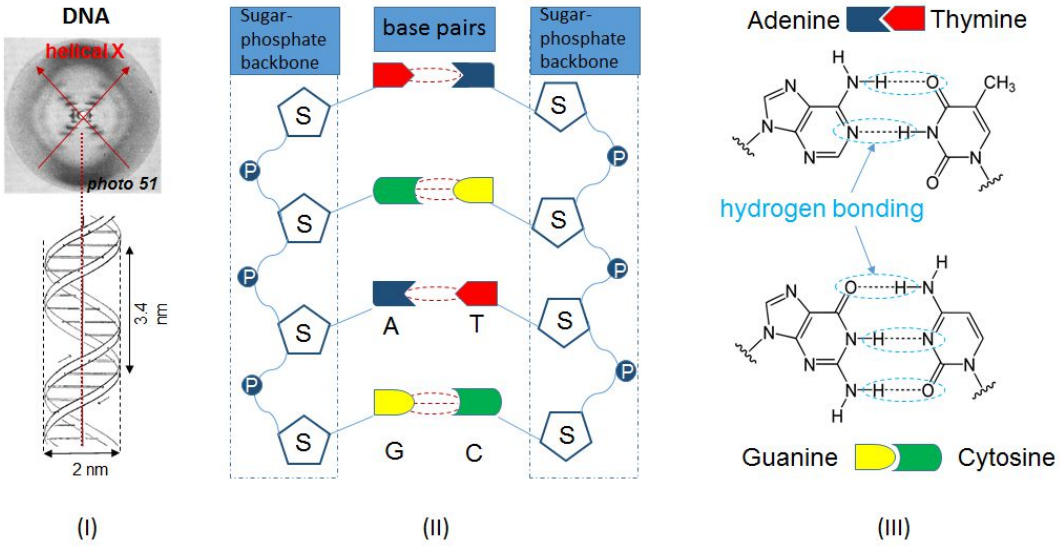

Figure 6.4 The X-ray crystallography image (Photo 51)[151] *of DNA indicates the helix structure of Watson-Crick DNA model*[152] *underneath (I): Illustrative scheme of base pairs and sugar-phosphate backbone in the helix structure (II). Schematic exhibition of hydrogen bonding between the base pairs (III), Adenine-Thymine (A-T) and Guanine-Cytosine (G-C).*

The natural DNA polymer is only ~ 2 nm wide helix structure and composed of nucleotide chains that can be thousands of base pairs (bp) long[152]. The length of the DNA molecule depends on the number of base pairs (1 bp is ~ 0.34 nm). The original model proposed that there are ten base pairs or 3.4 nm per turn of the helix. The double helix is kept together via hydrogen bonds between base pairs, Adenine-Thymine (A-T) and Guanine-Cytosine (G-C). The phosphate backbone is negatively charged with H^+ or Na^+ to balance the neutrality. So that, DNA is an anionic polyelectrolyte, in which sodium ions Na^+ counter ions can move freely along the macromolecule backbone[227].

The electrical conductivity of DNA remains debatable. In biological systems and biomaterials, the role of H-bonds is ubiquitous as previously discussed for gelatin. In DNA structure, the base pairs are kept together by highly specific H-bonding between amine (-NH or $-NH_2$) and carbonyl (C=O) groups. This bonding results in π-π stacking between the nearest base pairs with a distance of 3.4 A°. The first theoretical suggestion by Eley and Spivey assumed that the delocalization of electrons through π-coupled orbitals of nucleobases might lead to an efficient electron transport along the DNA molecule[228]. An overview related to the complex nature of DNA charge transport has been published by Genereux and Barton[229]. They suggested DNA can conduct in semiconducting range through its sequence. As several researchers agreed on that conduction proceeds by hole hopping from guanine to guanine through stacked G-C pairs, where guanine has the highest ionization energy (HOMO) among DNA bases[230]. Recently, electron tunneling through DNA where tunneling is observed at shorter distances, while hole hopping dominates at longer distances[230], [231]. However, bulk material transport of DNA is different from single-stranded DNA. Direct contact techniques have indicated that DNA is an electrical insulator at length scales greater than 40 nm[232]. So, the electrical conductivity along the π-π stacked backbone is still intriguing and remains controversial.

6.2.1.2.2 The ionic conductivity of DNA solid polymer electrolytes

The natural DNA sodium salt (DNA^--Na^+) was used as SPE in the active layer of LECs. Beforehand, the ionic conductivity of DNA was obtained using impedance spectroscopy. KCF_3SO_3 was utilized to increase the number of ionic species in the blend. The films were

deposited using aqueous solutions with a solid concentration of 4 g/L DNA and dried at 55°C for 15 min in ambient air. The Nyquist plots of impedance spectra for pristine DNA films are shown in figure 6.5a. The ionic conductivity (σ_i) of the SPE was defined using *equation 1*. The bulk resistivity (R_b) was extracted from the related equivalent Debye circuits of impedance data.

The data for DNA:KCF_3SO_3 blends were reported in the master's thesis of Guan Ni Yeo, who was nominally supervised by me during his studies[233]. Furthermore, the effect of drying conditions, plasticizer and different salt additives on the ionic conductivity were investigated in his thesis. Drying period for 60 min or drying under vacuum overnight lead to lower ionic conductivity. Annealing gave rise to aggregations in the thin film. The highest ionic conductivity was obtained 5.85 x 10^{-7} S/cm for DNA:KCF_3SO_3 [1:0.1] and 2.1 x 10^{-6} S/cm for DNA:KCF_3SO_3:Gly [1:0.1:0.3]. The higher salt concentrations resulted in reduced conductivity, possibly due to the lower ionic dissociation along the polymer chain. Aggregation tendency increased with the excess of the salt additive. Glycerol as plasticizer separates the chains and create a channel for ionic flow, thereby increasing the ionic conductivity.

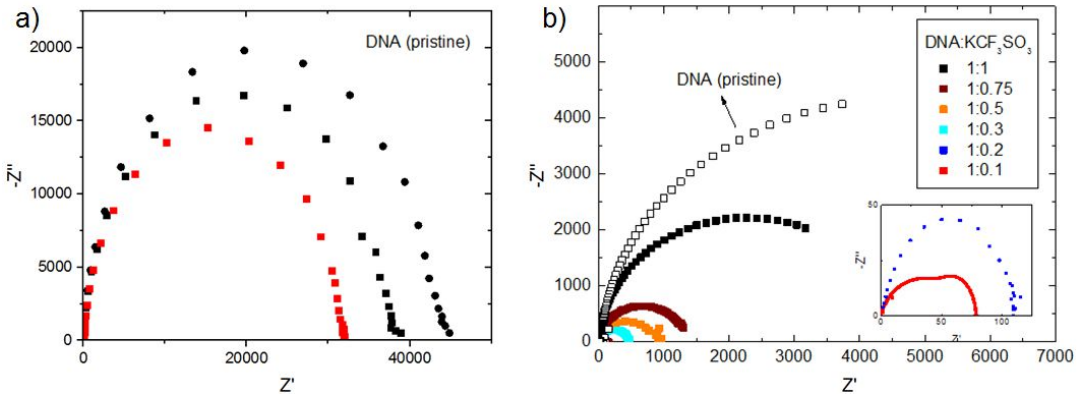

Figure 6.5 Nyquist plots of pristine DNA films (a) and DNA: KCF_3SO_3 SPE films (b). The data in (b) is adapted from the master's thesis of Guan Ni Yeo, ref.[233]. *For all Nyquist plots, both the imaginary (-Z") and the real (Z') axis are expressed in ohm [Ω].*

Annealing for more extended periods reduced the hydration of samples. The lower water content in thin films decreased the mobility of ionic species and their contribution to conductivity. Water content is crucial for determining DNA conformation and ionic conductivity.

In the solid phase, DNA is apt to be in the A-form, because H_2O molecules are not available to support the B-form[234]. The A-form is shorter and has a greater diameter than the B-form (see figure 6.6a). In the A form, the base pairs are closer to each other at a distance of ~0.25 nm, resulting in 11 base pairs per turn with ~2.8 nm rather than 3.4 nm. DNA shrinks when it dries and becomes 25% shorter than B-form. Similar to B-form, A-form double helix displayed distance dependency for charge transport; nevertheless, the hole transport of A-form was lower than B-form DNA duplexes[235].

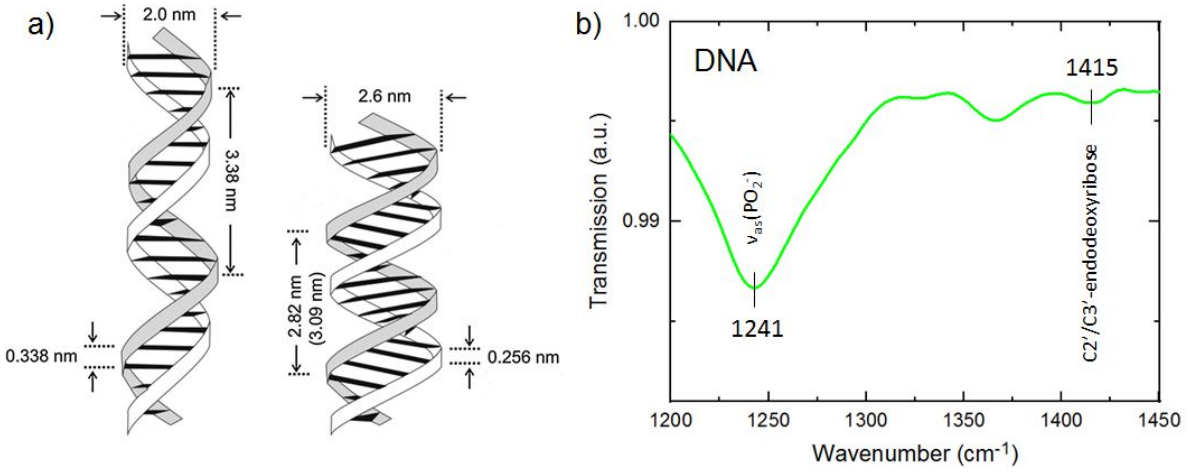

Figure 6.6 A-form and B-form of DNA, adapted from ref.[236]*. Copyright © 2014 The Royal Society of Chemistry (a). Fourier-transform infrared spectra of the DNA films (b).*

Figure 6.6b shows an expanded plot of the region between 1200 and 1450 cm^{-1} on Fourier-transform infrared spectra (FTIR) of DNA film (See Figure 8.3 in the appendix section). The two markers exhibit the antisymmetric stretching vibrations of phosphate ($\nu_{as}(PO_2^-)$) and the stretch vibrations of C2'-endo or C3'-endodeoxyribose of double-stranded DNA. The C–H deformation vibration arising from the C3'-endo deoxyribose was observed at 1417 cm^{-1}, indicating the A-form conformation of DNA strand[234]. According to the same report, $\nu_{as}(PO_2^-)$ for the A-form was observed at around 1240 cm^{-1}. The conductivity results were consistent with the theoretical predictions, which suggested that DNA has a better base pair (bp) stacking in wet conditions as it maintains B-DNA compared to that in dry conditions where it is in A-DNA form[226].

6.2.1.2.3 DNA based light-emitting electrochemical cells

DNA based SPEs were blended with water-soluble PPP polymer to deposit the active layer of LECs. The films were sandwiched between the ITO-glass and an Al cathode. Several w/w ratios of PPP:DNA at different solid concentration were tested to form the active layer of LECs. The current density-voltage-luminance characteristics and the device configuration are shown in figure 6.7. The first device exhibited the highest luminance of 1.2 cd/m^2 with a turn-on voltage of 13.5 V for PPP:DNA:KCF_3SO_3 at the ratio of 1:1:0.5 (See Figure 6.7a) and the total solid concentration of 37.5 g/L. We assumed that the high voltage range could be related to the layer thickness of ~ 500 nm and a high salt ratio in the blend. As previously discussed, the high salt ratio gives rise to lower ionic conduction and aggregation in the thin film. The light emission was not homogenous over the sample pixel area and the lifetime of the device was less than 10 seconds. After optimizing the PPP:DNA:salt ratio and the layer thickness, Guan Ni Yeo reported the highest luminance intensity 7 cd/m^2 with a turn-on voltage of 9.2 V for PPP:DNA:KCF_3SO_3 at w/w ratio of 5:1:0.1 in ref. [233] (See Figure 6.7b). The maximum luminance was recorded at 12 V. However, the lifetime of the device was improved from a few seconds to only several minutes. No light output was obtained from pristine PPP LECs (See Figure 8.2b in the appendix), which then can be considered as evidence that DNA performed as an ion-solvating polymer in the blend.

As previously reported by Kim et al., a low light emission (30 nW) was detected from the self-assembled PPP layers, where PPP derivative was substituted with biphenyl groups (meaning that with the less number of alkyl chains)[237]. They also pointed out that EL of PPP derivative was found to be similar to PL[237]. Therefore, in our work, the CIE color chromaticity diagram of PPP was evaluated using SpectrAsis software from the fluorescence spectrum, see figure 6.7c.

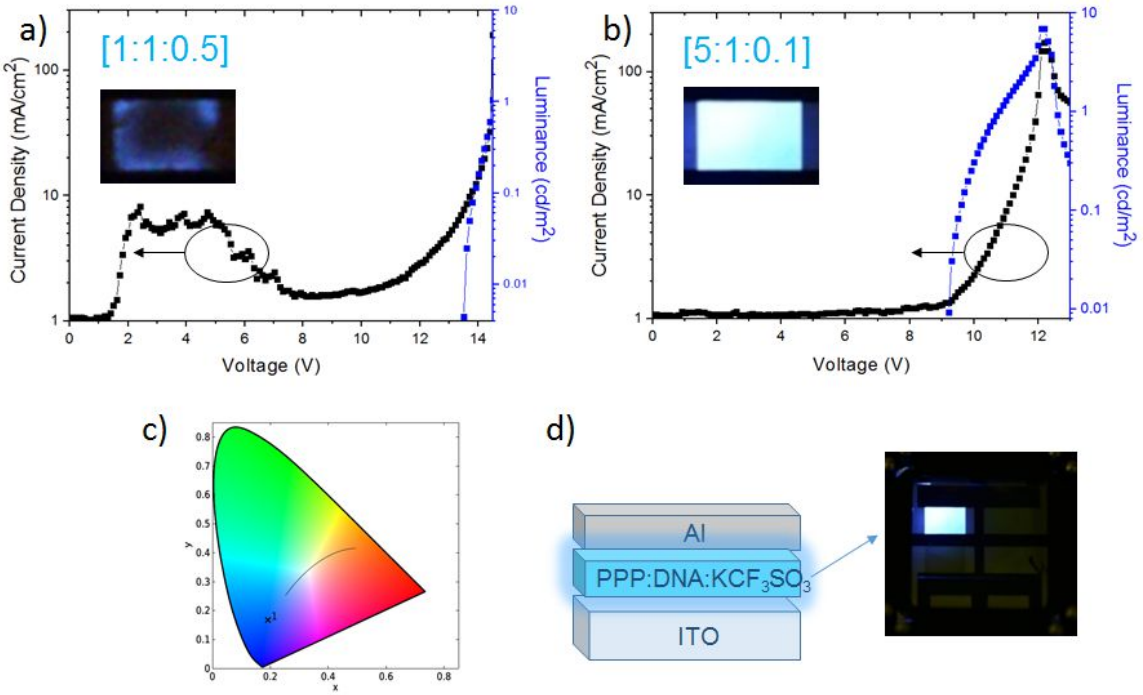

Figure 6.7 J-V-L characteristic of gelatin based LECs at varying w/w ratios of PPP:DNA:salt, 1:1:0.5 (a), 5:1:0.1 (b), insets: photographs of corresponding LECs under operation. CIE color chromaticity diagram of PPP was evaluated using SpectrAsis software from the fluorescence spectrum in appendix section (c). Illustrative representation of device configuration and top view of device under operation (d). The data in (b) is adapted from the master thesis of Guan Ni Yeo, ref.[233].

We determined the electrochemical stability window of DNA based SPEs by using cyclic voltammetry to control the possible side electrochemical reactions during device operation. The results are depicted in figure 6.8 and also compared to commonly used SPE systems. PEO: KCF_3SO_3 and PMMA:$TBABF_4$ exhibited a strong irreversible reduction peak with an onset at ca. −1.8 V and ca. -1.9 V, respectively. The cyclic voltammogram of DNA was stable in both anodic and cathodic regions between the sweeping potentials of ca. +1 V and ca. -2 V. However, with an increase of ionic species, DNA:salt [1:0.1] seemed to be slightly doping (reduced) with an onset at ca. -1.25 V in the cathodic region. We assumed that the reduction of DNA might play a significant role in the short lifetime of a device that comprises emissive materials with a large band gap. The optical energy band gap was calculated 3.1 eV from the onset wavelength of the absorption spectrum.

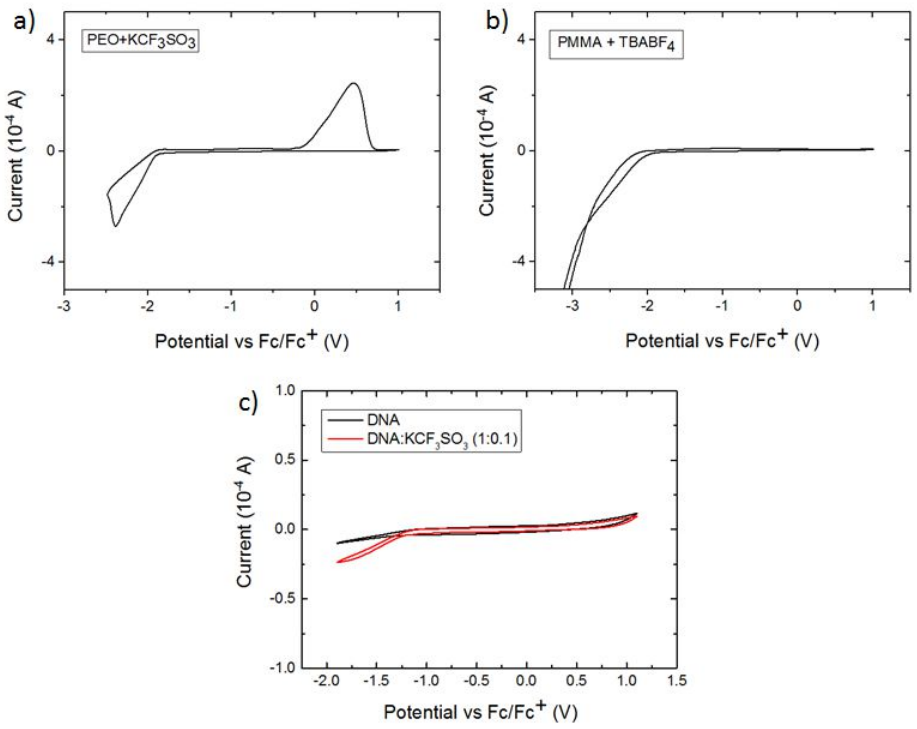

Figure 6.8 The cyclic voltammograms of previously reported SPE system: PEO: KCF_3SO_3 (a), PMMA:$TBABF_4$ (b) and DNA-based SPEs studied in this thesis (c).

One challenging aspect of DNA based SPEs was that we deposited from aqueous solution. In general, water residue and water absorption of the layers in humidity may result in stability problems for long-term device operations. Therefore, we annealed the active layers to eliminate the water residue in thin films. However, the ionic conductivity of DNA layers was directly proportional to the water content in the device. When we dried the films at high temperatures or over more extended drying periods, the ionic conductivity of SPEs showed the dropping tendency. In short, we found it difficult to improve the conductivity of the samples, while preventing the adverse effect of the residual water. Another challenge was finding an alternate commercially available water-soluble emissive material to optimize the charge transport properties and improve the device performance. Consequently, we investigated organo-soluble biomaterials as the next step.

6.2.2 Organo-soluble solid polymer electrolytes

6.2.2.1 DNA-lipid complex

The DNA-surfactant complex was tested as SPE in LECs. DNA-hexadecyltrimethyammonium (DNA-CTMA) was prepared by replacing Na^+ counter ions of DNA with a cationic surfactant group CTMA via ionic exchange. Dr. Markus Bender performed the procedure at Heidelberg University. The illustrative description is exhibited in figure 6.9. FTIR spectra of synthesized DNA-CTMA can be found in figure 8.3 (in the appendix). In FTIR spectrum, C-H stretch band at the wavelength number of ~ 2900 cm^{-1} corresponded to the aliphatic CTMA group in the structure.

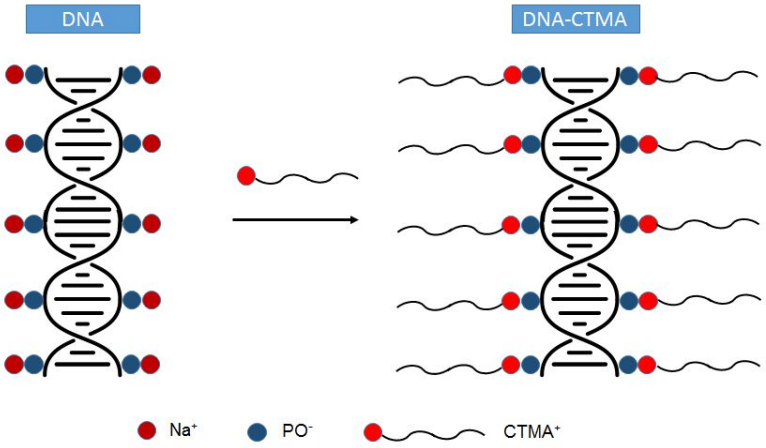

Figure 6.9 A schematic illustration of DNA-CTMA synthesis.

6.2.2.1.1 The ionic conductivity of DNA-CTMA solid polymer electrolytes

The ionic conductivity of DNA-CTMA and DNA-CTMA:salt with varying salt ratios was obtained by using impedance spectroscopy. Additionally, the ionic conductivity of SY:salt and SY:DNA-CTMA:salt were gathered for interpretation of the conductivity effect on the LEC performance. Tetrabuthylammonium tetrafluoroborate ($TBABF_4$) was utilized as a salt dopant in the mixture. The impedance measurements were analyzed and fitted with suitable equivalent circuits. The Debye circuit was applied for the data which did not show a grain boundary effect. When the

samples had grain boundaries or/and the data showed deviations from Debye semicircle, we used grain boundary model that was suggested by Huggins[238]. The models and Nyquist plots of the impedance spectra with fitting curves can be found in the appendix section.

The highest ionic conductivity of DNA-CTMA was obtained 9.41 $x10^{-8}$ S/cm which was almost two orders of magnitude higher than the DNA conductivity of $1.02x10^{-9}$ S/cm (figure 6.10a). The salt doped DNA-CTMA samples exhibited a reduced ionic conductivity. The highest conductivity was defined 4.6 $x10^{-9}$ S/cm for DNA-CTMA:salt [1:1]. The ionic conductivity of salt doped SY layers was at the lower range as expected (Figure 6.10b). SY:DNA-CTMA had the ionic conductivity of $1.54x10^{-10}$ S/cm which was higher than pristine SY conduction at the range of 10^{-12} S/cm. After adding DNA-CTMA into the SY:salt blends, the overall conductivity of SY:salt was improved significantly. The highest conductivity of SY:DNA-CTMA:salt blend was found to be $3.85x10^{-8}$ S/cm. All impedance results can be found in section 0 in the appendix.

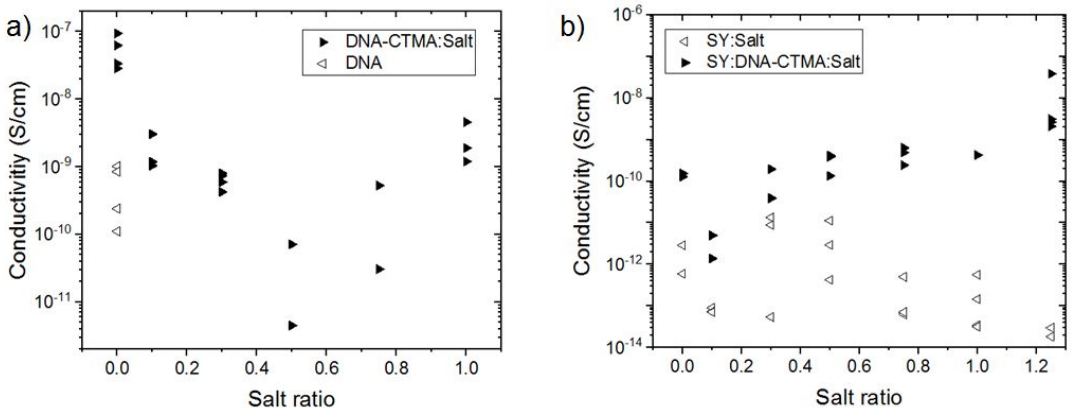

Figure 6.10 The conductivity results for DNA and DNA-CTMA based SPEs (a), SY:Salt and SY:DNA.CTMA:Salt (b).

For a better understanding of the impedance measurements, we characterized the surface topography and the aggregation tendency of films by atomic force microscopy (AFM) and white light interferometry.

The surface morphology of DNA and DNA-CTMA blends were analyzed by AFM using tapping mode. The AFM topographic images are shown in figure 6.11. We observed rod-like large aggregates on the topography image of DNA:PPP as seen in figure 6.11a. As we suggested, that might be due to the electrostatic interactions (electrostatic repulsion) between the polyanionic emissive polymer PPP and polyanionic DNA.

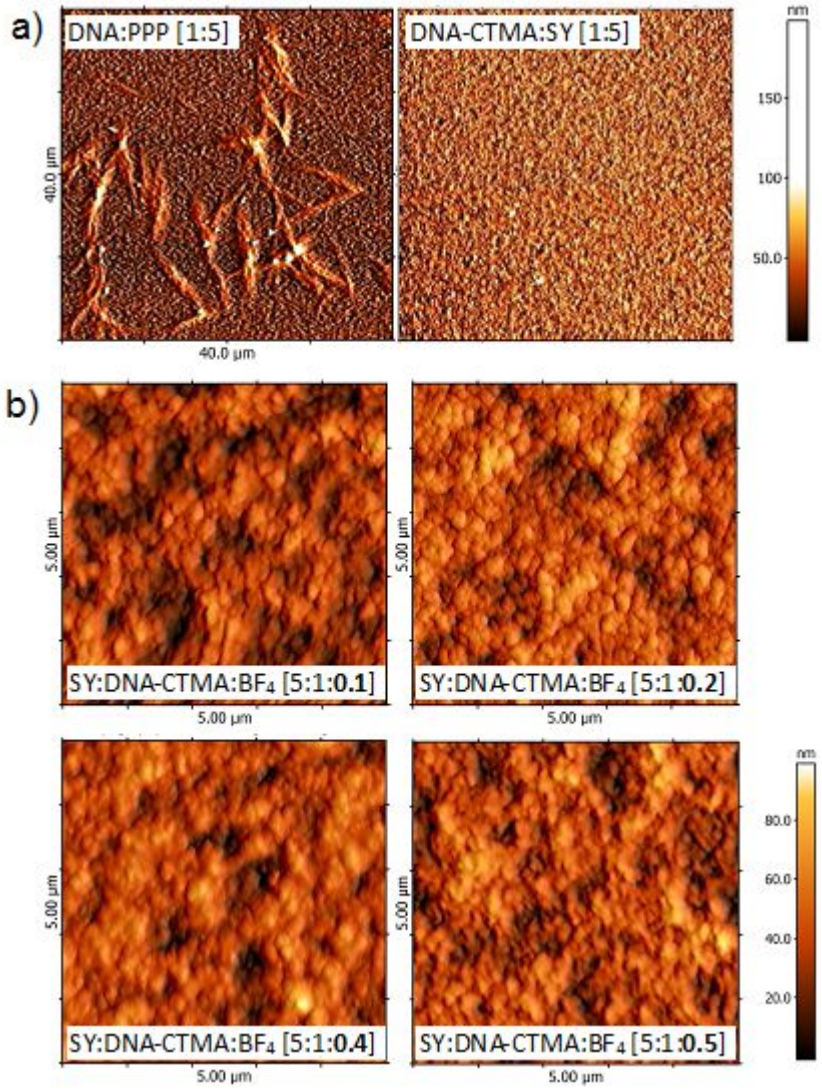

Figure 6.11 AFM topographic images of PPP:DNA and SY:DNA-CTMA blends with w/w ratio of [5:1] (a), SY:DNA-CTMA:TBABF$_4$ with different salt ratios (b). The colour scale bar in the right corner of (a) and (b) represents the height change of 0-200 nm and 0-100 nm, respectively.

Strong electrostatic repulsion between DNA strands and polyanion chains bearing sodium counter ions (Na^+) was reported elsewhere[239]. Since DNA is a highly negatively charged polymer, the high polyanion concentration stabilizes DNA duplex. Such chemical interactions between non-ionic polymers and biopolymers, e.g., DNA and proteins were relatively small[239]. Therefore, the morphology of the sample comprising an ionically conducting DNA-CTMA and a non-ionic polymer SY appeared to be more homogenous and smooth. On the other hand, as we discussed in the previous section, A-form conformation of DNA is valid in the thin film. Glassy (semi-crystalline) polymer behavior was reported for A-form of DNA in dry film conditions[234]. It was established that the ion transport principally occurs in the amorphous regions for polymer electrolytes consisting of both amorphous and crystalline fractions[118]. Surface morphology of SY:DNA-CTMA SPE with varying salt ratios are presented in figure 11.b. After introducing salt dopants into the film, the morphology remained unchanged in micrometric scale for DNA-CTMA:salt blend with different salt ratios.

Figure 6.12 exhibits the white-light interferometry topographic images of DNA-CTMA based SPE films. Each map covers the same dimensions, and the root-mean-square (rms) is shown in the bottom left corner of the corresponding image. DNA-CTMA film with various salt concentrations showed inhomogeneous morphology in micrometer scale. With the minimum amount of salt ratio (1:0.1), irregularly distributed large aggregates were present. The morphology consisted of grain boundaries for 1:0.3 ratio. In excess of salt dopant, the clusters became smaller and spread over the grains. The aggregation tendency and morphology change are schematically illustrated below interferometric maps. We proposed that the inhomogeneous morphology and the aggregation in the films affected the bulk ionic conductivity of the solid polymer electrolyte. The 1:0.5 ratio showed the lowest ionic conductivity. The conductivity of the film was found to be increasing with smaller aggregates. The similar effect was observed in the topography images for a lower salt amount in DNA-CTMA:Salt blend. SY:salt films (figure 8.10) showed a homogeneous distribution of surface morphology without any observable grain boundaries, probably due to the better intermixing. The white light interferometry images for SY:salt and DNA-CTMA-salt with reduced salt ratio can be found in section 8.6 in the appendix.

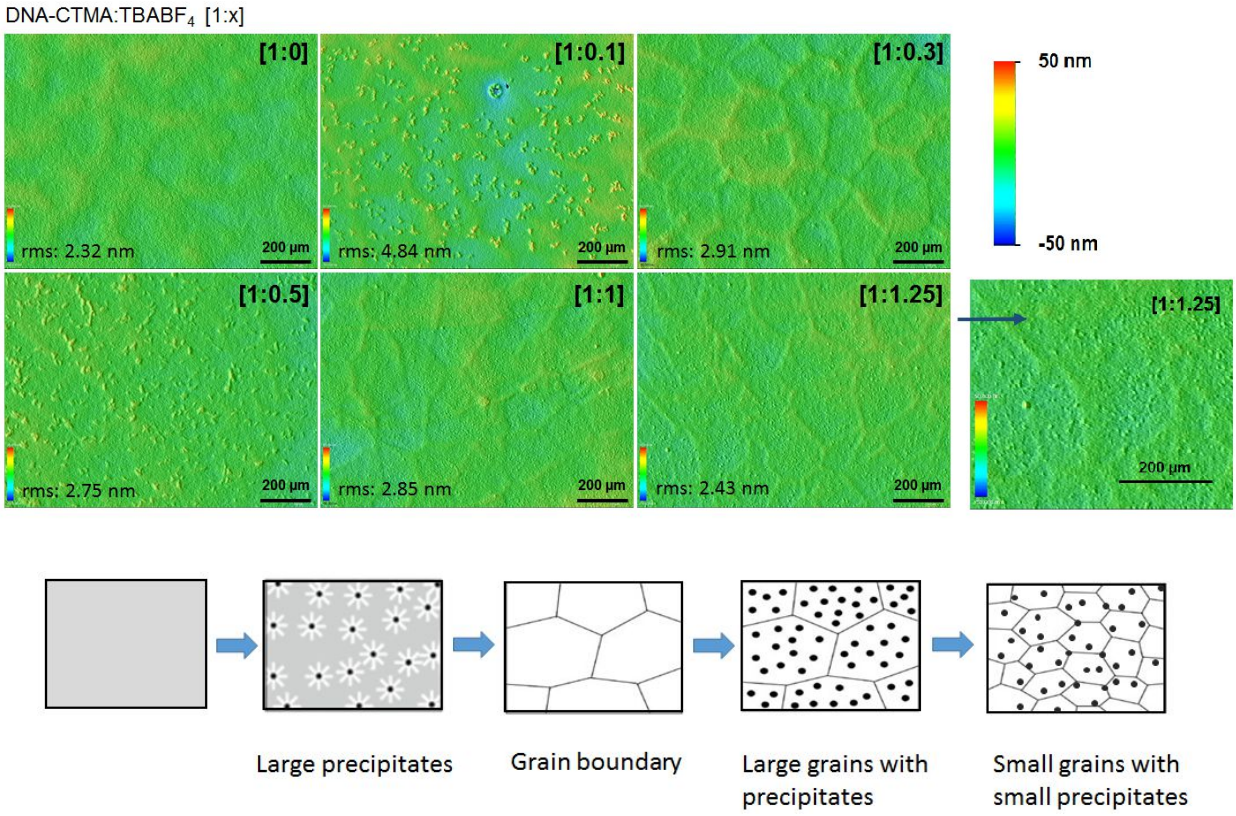

Figure 6.12 Interferometric topography images of DNACTMA:salt [1:X] films on glass. Each map covers the same dimensions: the color scale is presented in the upper right corner represents the height change. The root-mean-square (rms) of is shown in bottom left corner of the corresponding image. Underneath: Illustrative description of aggregation and grain formation in thin films (b).

As seen in figure 6.13, SY:DNA-CTMA:salt thin films formed more uniform layers compared to the results for DNA:CTMA:salt. The films showed a homogeneous distribution of surface morphology without any observable grain boundaries, yet the small aggregates were present. However, the impedance data exhibited depressed semicircles having centers lying below the real axis confirming the presence of the non-Debye type of relaxation phenomenon. The samples with high salt ratio showed two merged semicircles, which were attributed to two relaxation processes, as seen in section 0 in the appendix.

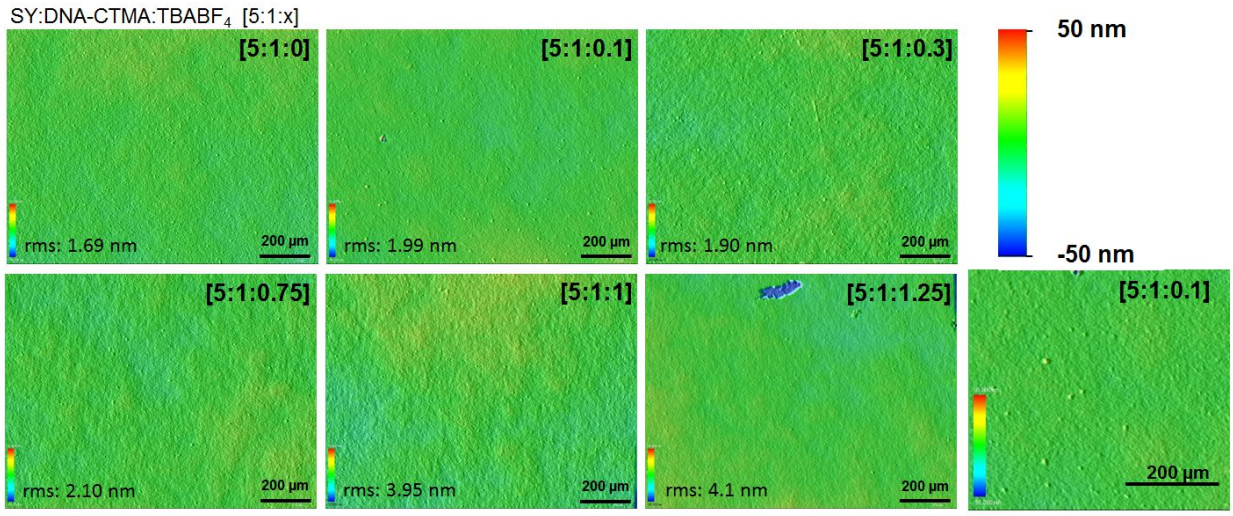

Figure 6.13 Interferometric topography images of SY:DNACTMA:salt [5:1:X] films on glass. Each map covers the same dimensions: the color scale is presented in the upper right corner represents the height change. The root-mean-square (rms) of is shown in bottom left corner of the corresponding image.

6.2.2.1.2 DNA-CTMA based light-emitting electrochemical cells

DNA-CTMA based SPEs were blended with yellow emissive polymer *Super Yellow (SY)* as the active layer of LECs. The films were sandwiched between the ITO-glass and an Ag cathode. The current density-voltage-luminance characteristics, electroluminescence, and the device configuration are shown in figure 6.14. The turn-on voltage of devices ranged between 3.5-10 V. An improved conductivity due to the higher number of ionic species in the blend resulted in lower turn-on voltages. The LECs showed a maximum luminance at the range of 1500-2000 cd/m^2. The highest luminance intensity was obtained 1544 cd/m^2 with the lowest turn-on voltages of 3.5 V for SY:DNA-CTMA:salt blend (5:1:1). Electroluminescence (EL) of SY OLED and SY LEC with DNA-CTMA based SPEs are shown in figure 6.14c. The identical EL data indicates that DNA-CTMA did not optically interact with SY. According to the CIE color chromaticity diagram, color emission (x=0.48, y=0.51) was similar to SY reference OLEDs. A sketch of device configuration and a photograph of DNA-CTMA based LEC under operation are shown in figure 6.14d. The sample exhibited homogenous light over the pixel area. The photos of the pixels of

DNA-CTMA based LEC with different salt content are presented in figure 6.15. Homogenous light output was observed for all the blends.

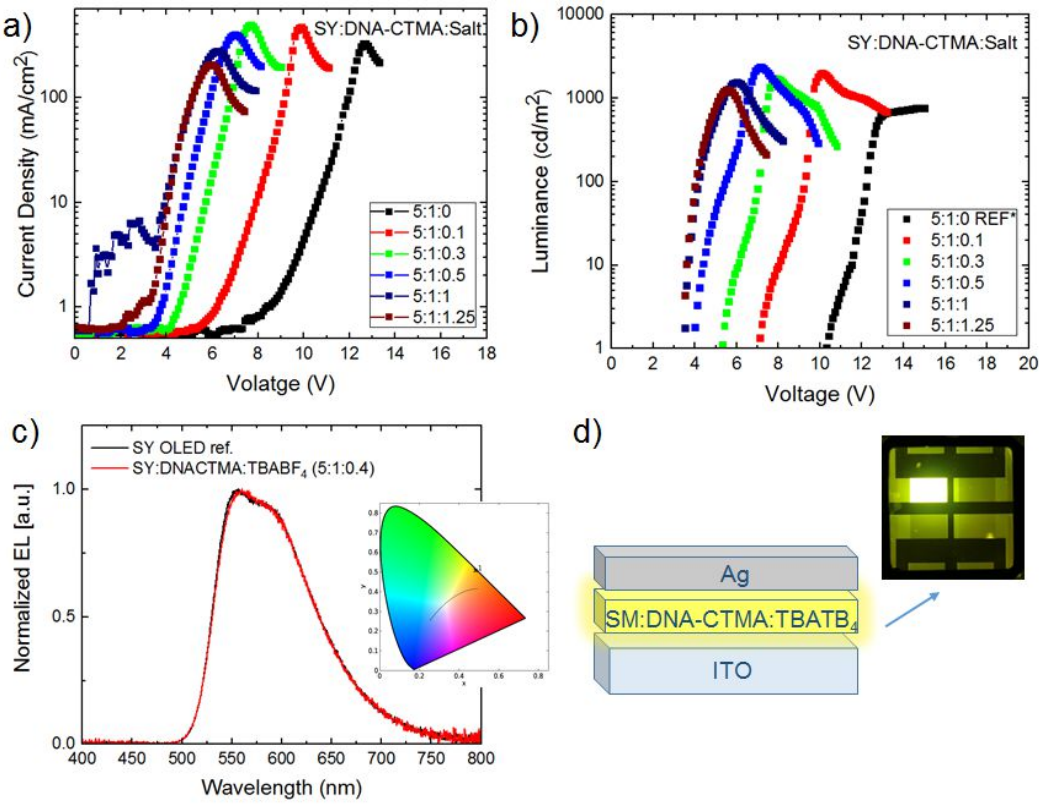

Figure 6.14 Current density voltage (a) and luminance-voltage characteristic (b) of DNA-CTMA based LECs. Electroluminescence spectrum of SY OLED (reference) and SY LEC (c), inset: CIE color coordinates of SY LEC. A sketch of device configuration and a photograph of DNA-CTMA based LEC under operation (d).

Figure 6.15 Photographs of DNA-CTMA based LEC under operation. Each pixel corresponds different salt content in the blend of SY:DNA-CTMA-TBABF$_4$ [5:1.:x].

SY:$TBABF_4$ LECs were built as the reference cells to investigate the influence of SPE on the device performance. The current-density-voltage-luminance results for SY LECs (reference) are depicted in figure 6.16. The maximum luminance intensity ranged between 1600-1800 cd/m^2 with the turn-on voltages of 6.2-11 V. The reference devices exhibited a lower luminance intensity comparing to SY LECs including DNA-CTMA based SPEs. Furthermore, the turn-on voltages were obtained about 2 V higher than SY:DNA-CTMA LECs. The highest luminance intensity was obtained 244 cd/m^2 at 8 V with the lowest a turn-on voltage of 6.2 V. Under same operational conditions, inhomogeneous light output was observed for the reference cells.

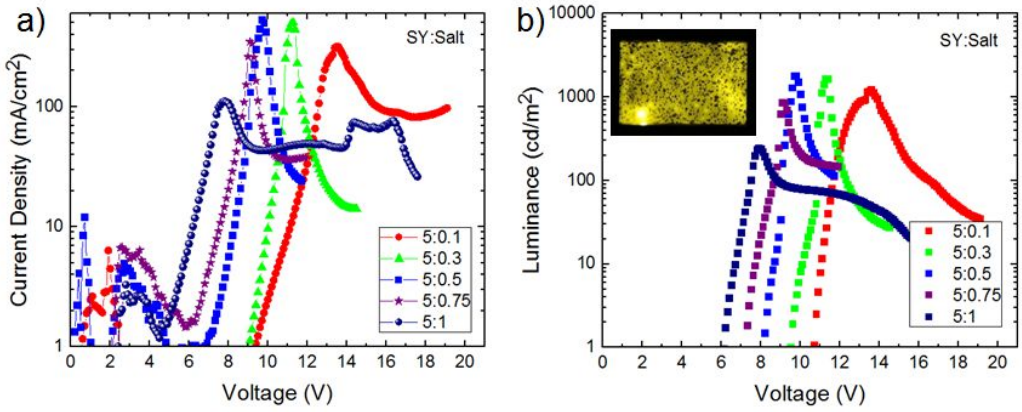

Figure 6.16 J-V-L characteristics of SY:salt (reference) cells. Inset: A photograph of device pixel under operation.

The lifetime of SY:DNA-CTMA LECs were investigated, and the results are shown in figure 6.17. The time-dependent voltage and luminance characteristics of SY:DNA-CTMA:$TBABF_4$ with the ratio of 5:1:0.1 were defined at a constant current density of 20 mA/cm^2. The lifetime of the device was around one hour. In figure 6.17b, an initial decrease of the operational voltage for SY:DNA-CTMA:$TBABF_4$ with a ratio of 5:1:0.5 was observed as the typical turn-on behavior of LECs. During galvanostatic operation at a set current, a decrease in voltage by time was typically taken as proof of in situ electrochemical doping in LECs[180]. A higher amount of ionic species grants a rapid ionic transport, resulting in faster electrochemical doping of the semiconductor at the electrode interface. The voltage drop was also observable at the beginning of the lifetime

measurements. The lifetime graphs were recorded at galvanostatic mode with three different constant current densities: 20 mA/cm^2, 18 mA/cm^2, 29 mA/cm^2 for the salt content of x:0.1, 0.3 and 0.5, respectively. Both the fraction and the operation conditions affected the lifetime and the maximum luminance of LECs. As reported previously, a faster turn-on time with the shorter lifetime was detected, when LEC was comprising a larger amount of SPE[240]. Additionally, a higher current density accelerated the undesired side reactions, which then limited the operational lifetime[241].

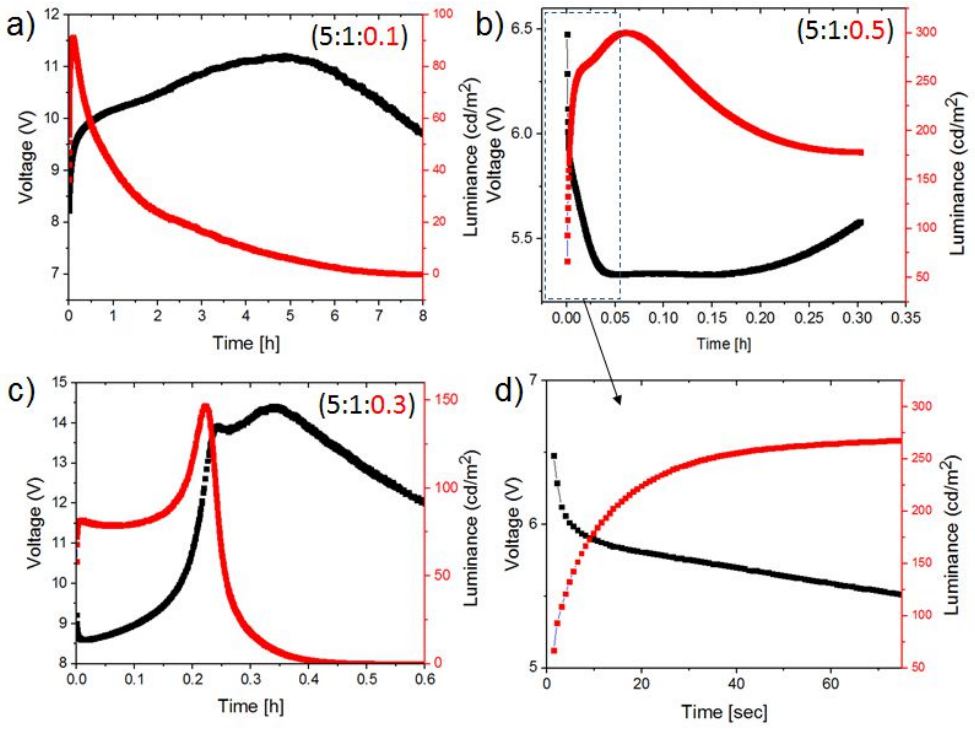

Figure 6.17 The time dependent voltage and luminance characteristics of SY-DNA-CTMA:TBABF$_4$ at different ration (5:1:x). The measurements were conducted at constant current densities of 20 mA/cm^2, 18 mA/cm^2 and 29 mA/cm^2 for the salt concentration x=0.1, 0.3 and 0.5, respectively.

The oxidation and reduction onsets of CP should not exceed the oxidation and reduction potentials of electrolyte to eliminate irreversible electrochemical side reactions [126], [127]. In other words, p and n doping of the semiconductor are expected to remain within the electrochemical stability window of SPEs for device stability. Therefore, solid polyelectrolytes with larger electrochemical stability windows were engaged in the active layer to improve the

device stability[115]–[117]. HOMO-LUMO levels of DNA-CTMA were already reported as 5.6 eV and 0.9 eV, respectively[221]. The HOMO-LUMO levels of SY were estimated 5.45 eV and 2.95 eV from the cyclic voltammograms in Chapter 5. The reduction potentials of SY stayed within the electrochemical stability window of DNA-CTMA. However, the higher salt amount in the blend resulted in shortening the device lifetime. We speculated that it might be associated with irreversible side reactions, due to the increased number of ionic species in the blend.

In polymer LECs, polymer blends in the active layer encounter a phase separation issue, which plays a critical role in device performance. Phase separation is a well-known phenomenon, due to the mismatch polarity between non-polar conductive polymer and a polar SPE, that we previously reported for PMMA:SY LECs[183]. A similar problem was also observed while testing other biodegradable polymers in our group. For instance, poly-Lactic-co-glycolic acid (PLGA) with the monomer ratio of 85:15 was examined by Bohui Wang in her master's thesis that was nominally supervised by me[242]. The device exhibited the maximum luminance of 1081 cd/m^2 at the lowest turn-on voltage of 4.3 V. After that, we reported PLGA with different monomer ratios, resulting in the highest luminance intensity of 3800 cd/m^2 with the turn-on voltage of 4.1 V for the monomer ratio 85:15[243]. A drawback of SY:PLGA was that they tend to phase separate in the film. Cao et al. demonstrated that the device performance was significantly improved when the phase separation was minimized via better polarity match of the components[244]. Therefore, another biodegradable polymer, polycaprolactone (PLC) was tested as an ion-solvating polymer in LECs by our group[245]. No phase separation was observed for the device that shows the highest luminance intensity of 262 cd/m^2 with a turn-on voltage of 3.8 V. The surface morphology of SY:DNA-CTMA blends with the ratio of 5:1 was investigated by using fluorescence microscopy, and the images are depicted in figure 6.18. SY:DNA-CTMA did not exhibit any phase separation in figure 6.18b while presenting only small aggregates in 6.18a.

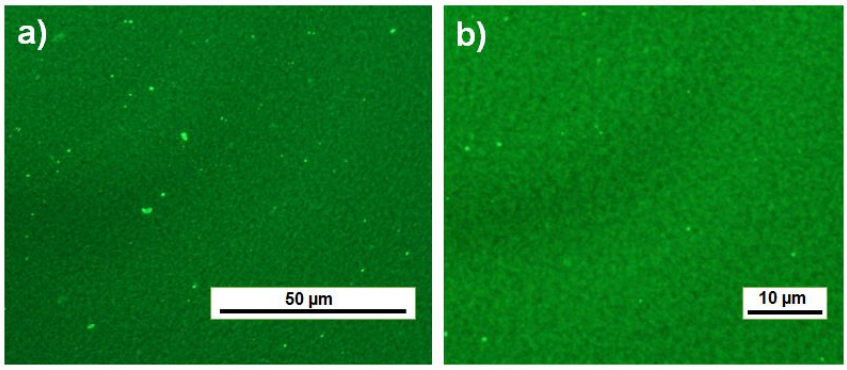

Figure 6.18 Fluorescence microscopy images of SY:DNA-CTMA (with w/w ratio of 5:1) films.

6.3 Conclusion

The main focus of this chapter was the investigation of natural biopolymers as solid polymer electrolyte in LECs, considering their potential applications in future biodegradable optoelectronics.

First, the water-soluble gelatin and deoxyribonucleic acid (DNA) based polyelectrolytes were tested in the active layer of LECs. The salt dopants at varying ratios were utilized as the additional ionic source to enhance the ionic conductivity of SPE systems. Additionally, the plasticizer effect was taken into account for the improvement of ionic conductivity. The maximum ionic conductivity of gelatin based SPEs was obtained 5.51×10^{-8} S/cm for gelatin:salt and 8.31×10^{-9} S/cm for gelatin:salt:glycerin blends. The ionic conductivity of DNA was found to be at the range of 10^{-9} S/cm. The highest ionic conductivity of DNA:salt and DNA:salt:plasticizer was reported before as 5.85×10^{-7} S/cm and 2.1×10^{-6} S/cm, respectively[233]. The ionic conductivity was increased by doping the layers with salt and plasticizer. The SPEs were mixed with water-soluble blue-emissive polymer PPP to form the active layer of LECs. Gelatin based blue LECs exhibited the highest luminance of 1.2 cd/m2 at ~8.5 V. A non-uniform light emission was observed with a very short lifetime for ten seconds or less. The highest luminance intensity of 7 cd/m^2 with a turn-on voltage of 9.2 V was obtained for DNA-based LECs. The device showed homogenous light output over the pixel area, yet the lifetime of the device was only several minutes.

The challenging aspect of gelatin and DNA based SPEs was that they were deposited from aqueous solution. The amount of water resided in gelatin and DNA would be detrimental for the lifetime purposes of electroluminescent devices. When the layers were annealed to eliminate water residue in the films, the ionic conductivity of layers was decreased. In short, it was difficult to improve the conductivity, while preventing the adverse effect of the residual water. Another issue was finding commercially available water-soluble emissive materials to test for better device performance.

As the second part of this chapter, we used modified DNA as the ion-solvating polymer in LECs. The DNA-surfactant complex (DNA-CTMA) is organo-soluble material due to the lipid surfactant CTMA group in the structure. The ionic conductivity of DNA-CTMA with the salt additive at varying ratios was defined. The highest ionic conductivity was obtained 9.41 $x10^{-8}$ S/cm and 4.6 $x10^{-9}$ S/cm for DNA-CTMA and DNA-CTMA:salt, respectively. For a better understanding of the ionic conductivity change, the surface topography and aggregation tendency of the films were investigated. We assumed that the inhomogeneous morphology and aggregation in the layers affected the bulk ionic conductivity of SPEs. The active layers of LECs exhibited more homogenous morphology when they were composed of the SPEs and the yellow emissive polymer (Super Yellow). The conductivity of SY:salt blends (reference cells) was significantly improved by introducing DNA-CTMA into the mixture. The DNA-CTMA based yellow LECs showed the maximum luminance intensity at the range of ~1500-2000 cd/m^2 with the turn-on voltage of 3.5-10 V. The higher number of ionic species in the blend resulted in a lower turn-on voltage. Electroluminescence of LEC was identical to reference SY OLED, showing the same CIE color coordinates. All samples with varying salt content exhibited homogenous light over the pixel area. The lifetime was around 1 hour for the device with the lowest salt content. In short, the first part of the chapter was the proof of concept for the implementation of biopolymers in LECs. The results of the second part the study related to organo-soluble materials were promising for further development.

Chapter 7

Summary and outlook

Thanks to tremendous efforts in the field, OLEDs are now at the largest share of the organic and printed electronics market[7] after 30 years of their invention. Due to their flexibility, lightweight, thin and highly efficiency structure, OLEDs have suited well with display technology. There are still challenges that need to be overcome. Some of these challenges are finding low-cost, flexible and stretchable barrier films, require of air-stable cathode materials and adapting cheap, high throughput methods for roll-to-roll manufacturing. In this context, LECs can serve as suitable alternative electroluminescent devices for particularly solid-state lighting (SSL), due to their simple device structure bearing air-stable cathodes and easy-processed fault-tolerant layer thickness[16]. However, the performance concerning lifetime and efficiency must be improved to make LECs competitive technology in the market.

In this final chapter, the contributions of our work in the field will be summarized first. After, an outlook for further research suggestions arising from the findings of this dissertation will be given. The viability of the organic light-emitting devices regarding the device stability and efficiency, as well as the cost, will be overviewed for future perspectives.

7.1 Summary

To wrap the whole story, we applied sustainable materials and processing techniques for the solution-based engineering of the organic light-emitting devices at the interface between device processing, material functionality, and device architecture (see figure 7.1). We deposited the organic layers by using either well-established solution processing methods such as spin coating and doctor-blading, or gravure printing which was highlighted as an alternative technique to scale up the production. We utilized different type of materials including organic semiconductors (small molecular weight material and conductive polymers), electrically inert host polymers, emissive and non-emissive polyelectrolytes in the different layers of altering device architectures depending on their functionalities. Organic light-emitting diode and light-emitting electrochemical cell structures were two main device types that were commonly implemented in our work. Alternatively, we suggested a hybrid device architecture uniting OLED and LEC functionalities in one single cell. All findings were examined in three main parts.

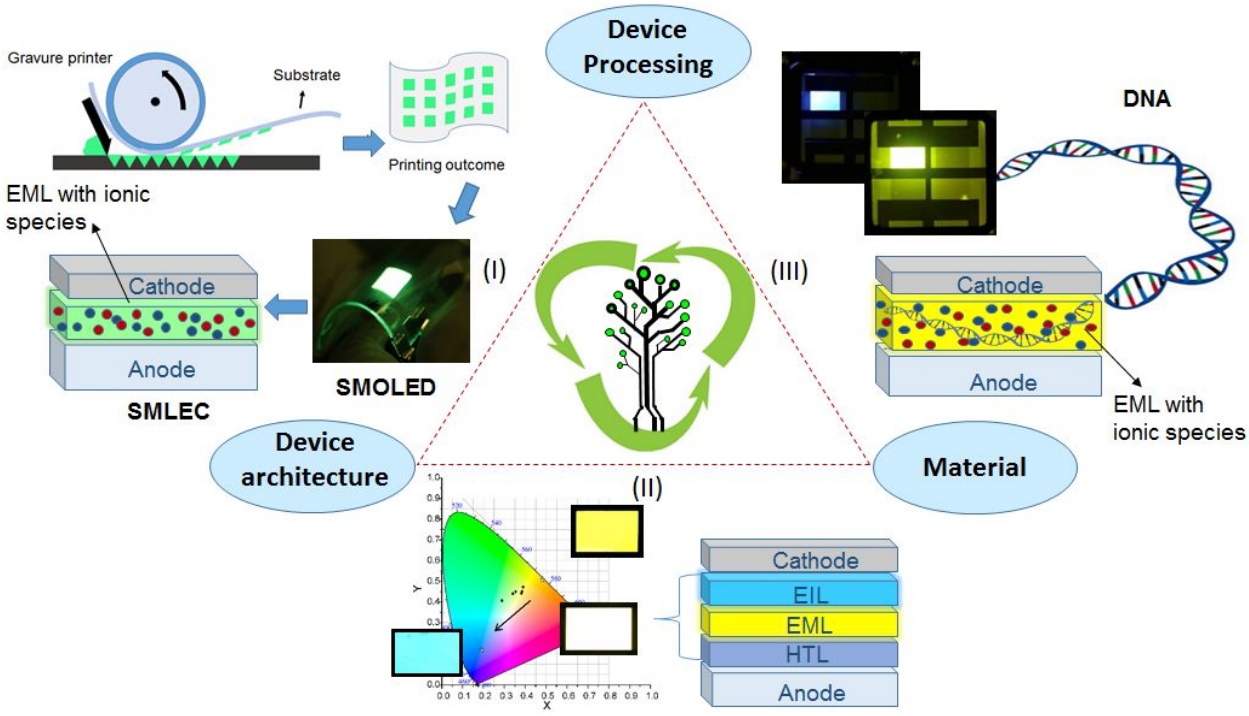

Figure 7.1 Interface between device processing – materials – device architecture.

In the first part, we presented the implementation of the gravure printing technique for the organic layers of flexible small molecule organic light-emitting diodes (OLEDs) and small molecule light-emitting electrochemical cells (SMLECs). The homogeneous printed films were granted either via tuning the functional ink properties or changing the parameters of the printing process. For this context, we considered the ink viscosity, the surface tension and solvent drying kinetics of the functional inks for the printability of active layers of SMOLEDs. The process parameters, particularly the gravure cell parameters (e.g., line screen and tone value) were altered to obtain sufficiently thin, homogenous active layers of SMLECs. In both cases, a common method of merging small molecules in inert polymer matrix was utilized as an approach to adjust the rheological behavior of the small molecule inks to a printable range. Additionally, the host materials assisted better device efficiencies via suppressing the small molecule aggregation in the solid film. The film morphology was analyzed in a qualitatively and quantitatively. After adjusting the parameters which are mentioned above, the homogenous printing outcomes were successfully applied in the emissive layer of organic light-emitting devices on flexible plastic substrates. The results, in terms of device efficiency and functionality with air-stable electrodes, showed that the gravure printing method would be a viable method for roll-to-roll (R2R) manufacturing of small molecule based devices in the future.

The second part described a hybrid device architecture for a simultaneous color-tuning and the white light emission in polymer OLEDs bearing air-stable electrodes. We fabricated the device by depositing a single component LEC on top of a conventional polymer OLED stack. The single layer LEC acted as the second emissive layer while maintaining the charge injection from an air-stable cathode into the emissive layer of OLED. Thus, two components dominated the overall device emission resulting in color-tuning at varying layer thicknesses of the LEC. The emission color of the bilayer device was shifted from the yellow-green region to the edge of the white light region on the CIE color chromaticity diagram by increasing the thickness of the LEC. The electroluminescence with a high color temperature demonstrated that this approach would be beneficial for white-light OLEDs bearing air-stable electrodes.

In the last part, we investigated biodegradable materials as solid polymer electrolytes (SPEs) for LECs. Gelatin, deoxyribonucleic acid (DNA), and modified DNA were utilized as SPEs and intermixed with different emissive polymers to form the active layer of LECs. As the first step, naturally derived, water-soluble polymers; gelatin and DNA were tested as ion-solvating polymers in the emissive layer. We modified the ionic conductivity of SPEs with the addition of salt and plasticizer dopants. We optimized the thin film formation and ionic conductivity of SPEs, accordingly. Additional to that, the electrochemical stability window of SPEs was defined to eliminate probable irreversible electrochemical side reactions during device operation. The poor device performances were related to the water residue in the blends. Since residual water would be detrimental for long-term device operations, we focused on the organo-soluble biomaterial based SPEs as the second step. We successfully implemented organo-soluble DNA-surfactant complex (DNA-CTMA) as SPE in LECs, where SPE was obtained by ionic exchange of the counter ions on DNA helix. The DNA-CTMA based SPE was doped with salt to enhance the ionic conductivity. A detailed surface topography analysis was conducted to characterize the phase separation between the polymer components and the aggregation tendency in the active layer of LECs. The results showed that biodegradable materials were adaptable as polyelectrolyte systems for LECs.

7.2 Outlook

Today, people are more aware of the environmental impact of electronics as a result of growing energy consumption and electronic waste, so that they have started to take reasonable steps towards a sustainable future. Researchers draw the attention of international policymakers for setting up new policies to reduce the ecological and health effects of electronic waste[12]. In recent years, there is a robust global momentum towards more energy efficient lighting by switching from halogen to LED bulbs. The National Academies Press 2017 reports that incandescent lamps will phase-out in 23 countries and regions[246]. For instance, the sale of halogen lights has been already restricted in German starting from 2009[247]. As another example, the International Year of Light 2015 was organized to raise awareness of the achievements of light science and its applications, and its importance to humankind[248].

The development of cheap, sustainable, and efficient electroluminescent devices remains the main focus of the material science and engineering field. According to Japan Display Inc. report, the power consumption of OLED panels has been dramatically reduced by 98% since the beginning of 2008[249]. Another critical point is how to fabricate a product by an environmentally friendly and economically feasible way. Printing can be considered as sustainable process technology that applies to R2R industrial manufacturing to reduce the production cost. In recent years OLED display manufacturers have started to develop ink-jet printed prototypes. Japan OLED display company JOLED Inc., which produced the first ink-jet printed OLED displays in 2017, intends to solicit $900 million to start mass production in 2019[250]. Cambridge Display Technology Ltd. offers printed small scale flexible OLED displays as low-cost everyday use products[251]. Even though ink-jet is a suitable process for pixelated displays, the main drawback is the limited resolution and the need for soluble and efficient materials. In this context, gravure printing with high resolution at high throughput properties[135], [145] would benefit large scale R2R fabrication of lighting, packaging products. Therefore, we adapted gravure printing technique for highly efficient small molecule based OLEDs and LECs using halogen-free solvents for upscaling purposes. For future studies, the micro-gravure method with advanced controlling in layer thickness and roughness (20 nm thickness, ~ 3-5 nm roughness) might be considered for printed electronics[252].

The lamination is still a hurdle for printed OLEDs, concerning to find low-cost and flexible barrier foils[7]. Therefore, seeking air-stable electron injection materials or different device architectures allowing electron injection from air-stable cathodes is another central topic in the field. In hybrid device architecture that we suggested for white light emission, the active layer provided electron injection from air-stable cathode while maintaining dual color emission. For general lighting applications, white light is required[28]. However, in our work, CRI and luminance values were lower compared to commercially available OLED panels. Different emissive materials might be tested to enhance the performance of the hybrid structure. Additionally, the need for stable blue emissive materials in the field remains challenging[253].

LECs have drawn intense attention with their simple device structure bearing air-stable cathodes[15] and easy processability[78]. However, they are not very well-suited for the state-of-the-art display applications, due to their relatively slow turn-on time[254]. They are suitable for integration in smart packaging, illumination, signage and healthcare devices[255]. After intense effort on understanding their complex device physics, LECs moved from fundamental science to industrial applications. Swedish company LunaLEC AB holds the patent of the first all-organic LEC and offers several prototypes with a minimum cost of 50 €[255]. According to cost analysis report on the fabrication of LECs, in the case of using high-throughput R2R processing techniques and low-cost materials, LEC can compete with other SSL technologies concerning price[256]. As pointed out in the report, the operational stability and efficiency of LECs should be improved for viability. Very recently, researchers developed LECs with a high brightness of 2000 cd/m^2 at 27.5% EQE[257].

Another important argument in the field of organic electronics is to replace the synthetic polymers with biopolymers to achieve biodegradable, biocompatible electronics for a sustainable future. The biomaterials have been already well integrated with biocompatible electronics[1] and implemented in different layers of OLEDs[206]. Testing low-cost and sustainable materials for LECs would be also beneficial for future technology. Therefore, we utilized different biodegradable natural polymers in the active layer of LECs. However, ionically and electrically conducting materials (DNA and DNA-CTMA) were considered in the charge transfer of the layers. Researchers can test different systems by intermixing DNA with different emissive polymers or small molecules for future work. Halogenated solvents were used in this part of the study. Chlorinated solvents should be eliminated due to their toxicity and environmental effects during device processing[258]. The biodegradability of SY and PPP remains unknown. Therefore, the biodegradability of emissive materials and salts might be investigated as well. Recently, as our ultimate goal to combine biomaterials with the cleaner manufacturing processes, our group published fully biodegradable printed LECs as a follow-up work of this thesis[259]. The results were promising for further research activities. Hence, I believe that there is an excellent future for printed and bio-based light-emitting devices. The material research and development will be the critical parameter for future advancement.

Chapter 8

Appendix

8.1 Synthesis and characterization of PFNCl

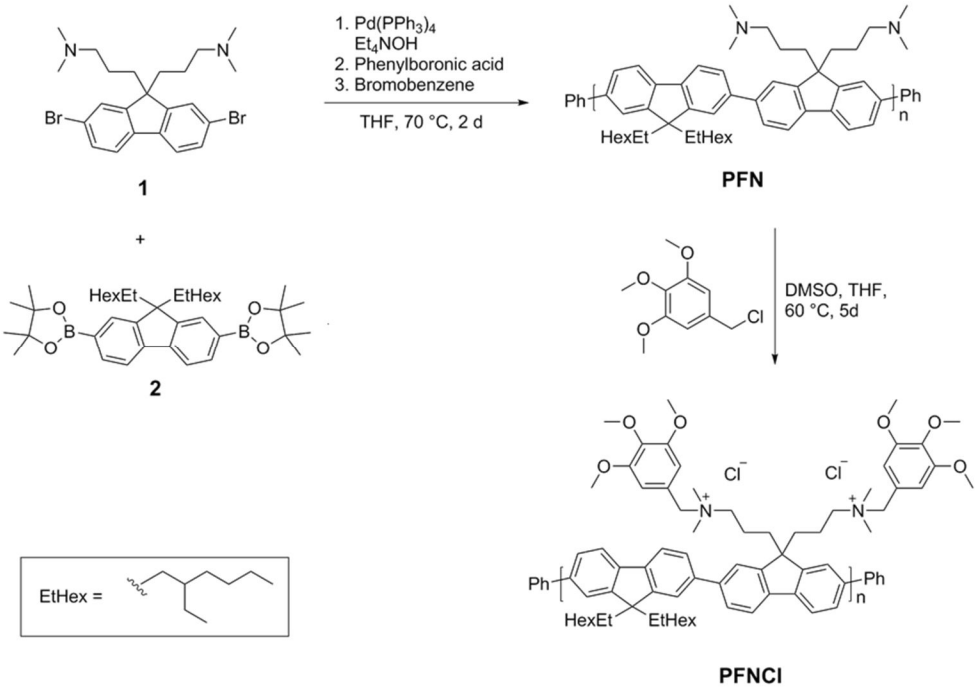

Figure 8.1 The synthesis route of the PFN and PFNCl polymers.

Dr. Petzoldt at Heidelberg University synthesized the PFNCl polymer by following the synthetic route that is illustrated above in figure 8.1. The detailed synthesis was described in ref.[186]. The characterization of the polymers, H-NMR, C-NMR data, and infrared spectra can be found in the dissertation of Dr. Petzoldt[148].

8.2 Film formation of gelatin

The plasticizers were used as the cross-linker to modify the mechanical strength of gelatin, as well as the film formation. The higher solid concentrations (sample no: 1-2) resulted in a hard gelatin or very viscous gel formation which did not allow film casting.

Table 8.1Summary of different gelatin solutions in 1 mL H_2O and their related film formations.

No	Gelatin	Plasticizer	Processing method	Layer thickness
1	133 mg	13 mg Glu	-	brownish soft plastic
2	133 mg	~0.26 mg Glu	-	viscous gel
3	80 mg	-	spin-cast	~800 nm
4	60 mg	2 mg Glu	spin-cast	460-485 nm
5	30 mg	1 mg Glu	spin-cast	110 nm
			drop-cast	10µm
6	30	10.5 mg Gly	spin-cast	265
7		-	spin-cast	~170
7	15	5.25 mg Gly	spin-cast	120-130
8		-	spin-cast	90-100

All solutions were prepared in 1 mL water and heated at 50°C. Thickness variations indicate to change in the solution temperature. Abbreviations for the plasticizers; Glu=Glutaralydeyde and Gly=Glycerin.

8.3 Absorption emission of PPP

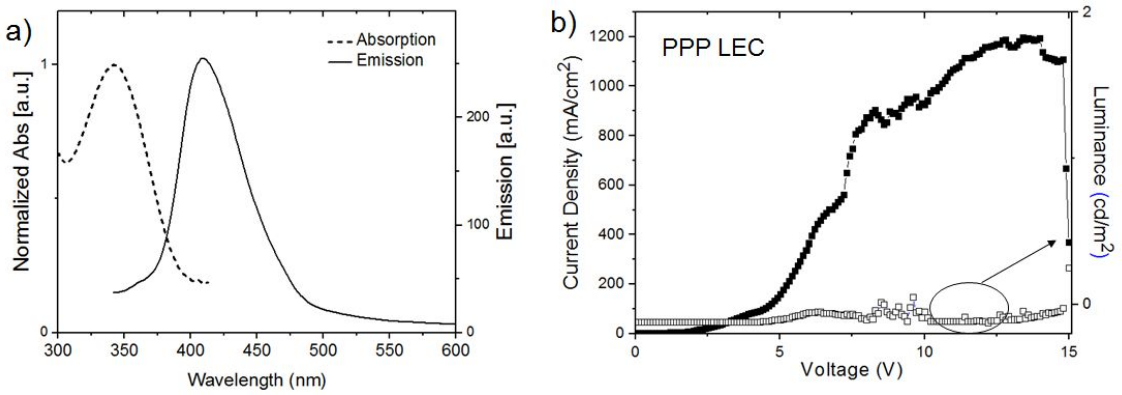

Figure 8.2 Normalized absorption and fluorescence spectra of PPP (a). For the optical characterization of the emissive polymer, a 50 nm thick film of PPP was deposited on glass. J-V-L characteristic of pristine PPP LEC.

8.4 Infrared spectra of DNA and DNA-CTMA

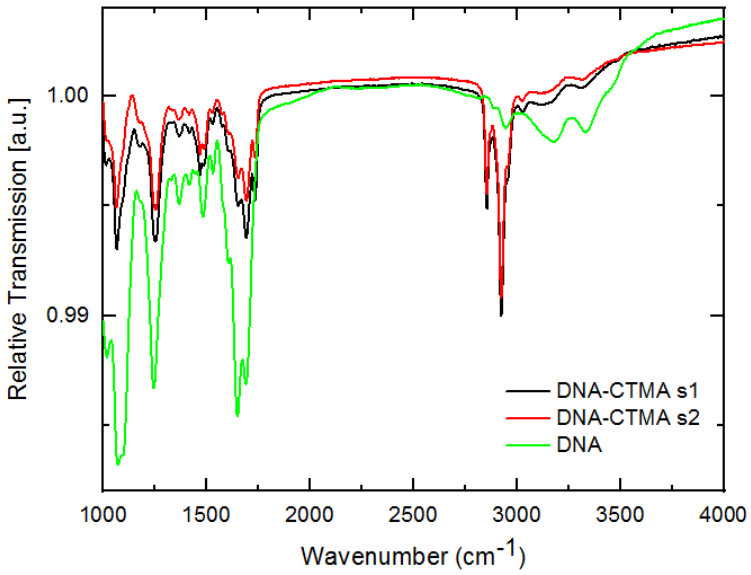

Figure 8.3 FTIR spectra of DNA and modified DNA with CTMA surfactant. DNA-CTMA s1 and s2 attributes to modification of DNA-CTMA at different time period.

Figure 8.3 shows the Fourier-transform infrared spectra (FTIR) of DNA and DNACTMA which were obtained by Dr. Sebastian Beck. The characteristic FTIR bands of DNA[260] were detected at 2926 and 2846 cm^{-1}, C=O stretching at 1647 cm^{-1}, C-N stretching at 1231 cm^{-1}, P-O at 1088 cm^{-1}, C-O at 1052 cm^{-1}, and CO bending at 962 cm^{-1}. The list of characteristic infrared band positions of DNA is summarized in Table 8.2. C-H stretch band at the wavelength number of ~2900 cm^{-1} corresponded to the aliphatic hexadecyltrimethylammonium group in the structure of DNA-CTMA.

Table 8.2 The list of characteristic infrared bands of DNA, compiled from an available reference data[260].

FTIR Band [cm^{-1}]	**Assignment**
970	Strongly coupled sugar–phosphodiester
1064	Vibration of ribose (C-C sugar)
1050–1100	Band due to the symmetric stretch PO2- emerges in phospholipids
1236	Antisymmetric stretching vibration of the phosphate group PO_2-, marker of B-form DNA
1200–1250	Phospholipids, occupied mainly by the intense band due to the antisymmetric PO_2- stretching mode
1328	Thymine aromatic amine stretch
ca. 1500	DNA in-plane vibrations related to G–C and A–T base pairs
1710–1715	Guanine carbonyl vibration stretch C-O

8.5 Impedance results of DNA-CTMA based SPEs

The equivalent circuits that were used to fit data of the impedance results and related Nyquist plots are shown in figure 8.4. The ionic conductivity (σ_i) of the SPE was calculated using either the bulk resistivity, R_b of associated Debye circuit or R_i of the equivalent circuit for grain boundaries. The impedance measurements were analyzed and fitted with the suitable equivalent circuits. We utilized the Debye model composed of a bulk resistance and a constant phase element (R_b//CPE) connected in series for the samples with no grain boundary effect. For the other samples presenting some deviations from a Debye semicircle, we applied the grain boundary model. Huggins suggested the model[238] describing a complex impedance plane plot with two semicircles. In this circuit, he connected a parallel R_{gb}/CPE_{gb} in series to the ionic resistance (R_i). He referred R_{gb} to the resistivity of the grain boundaries. In both models, we implemented a CPE instead of capacitance.

The Nyquist plots of the impedance spectra of DNA-CTMA based SPE films are shown in figure 8.5 and figure 8.6. The impedance data for SY:DNA-CTMA:salt and SY:salt blends are depicted in figure 8.7 and figure 8.8, respectively.

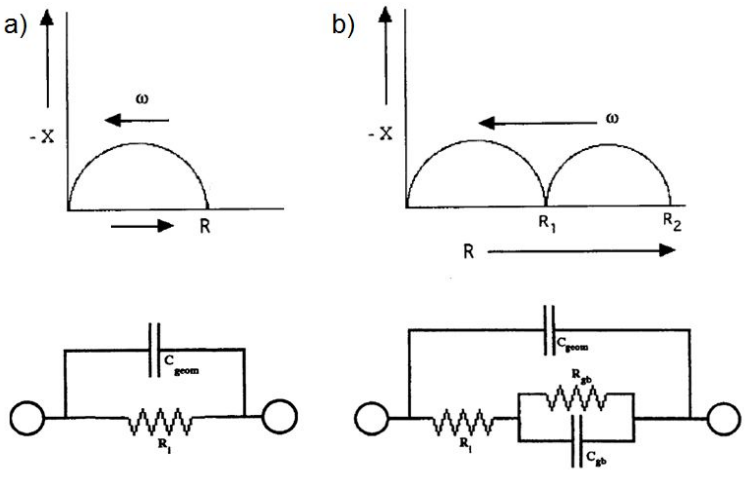

Figure 8.4 Equivalent circuit models: Debye model (a) and grain boundary model (b). Both models are modified using the equivalent circuits in ref. [238].

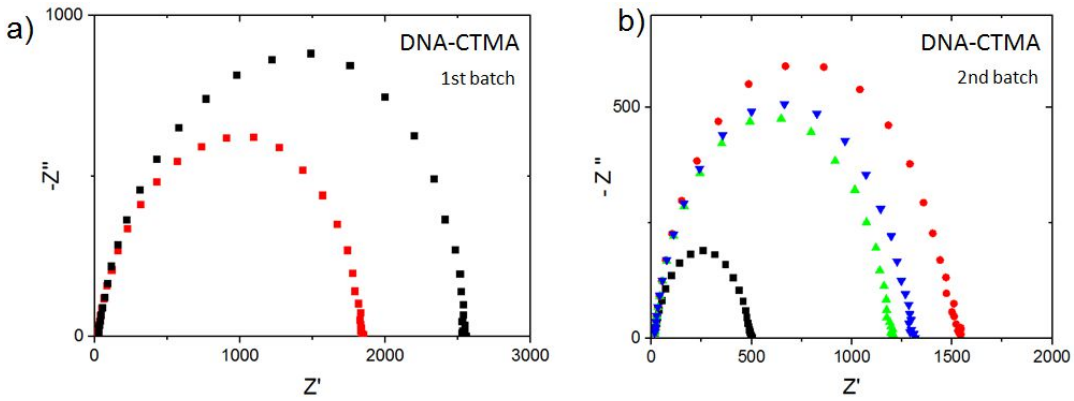

Figure 8.5 The Nyquist plots of impedance spectra for DNA-CTMA. For all Nyquist plots, both the imaginary (-Z") and the real (Z') axis are expressed in ohm [Ω].

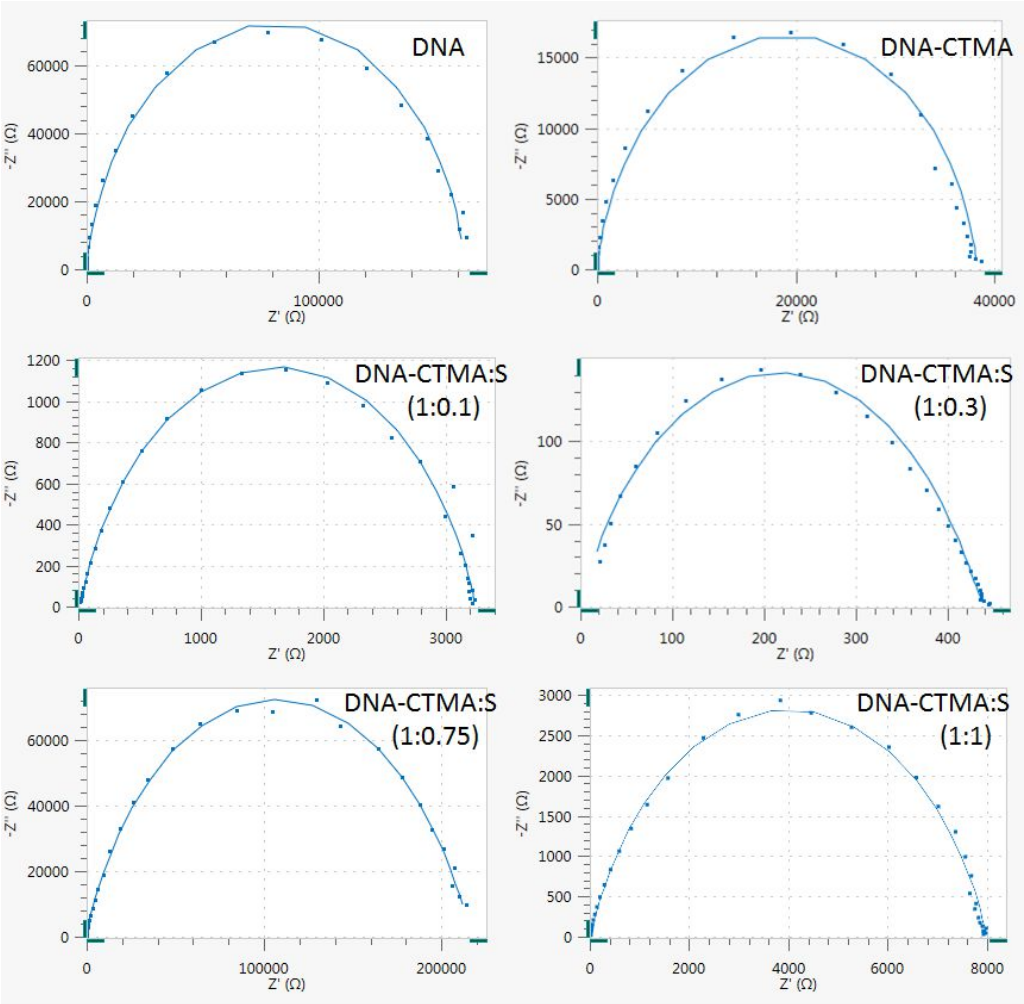

Figure 8.6 The Nyquist plots of impedance spectra and fitting curves for DNA and DNA-CTMA.based SPEs.

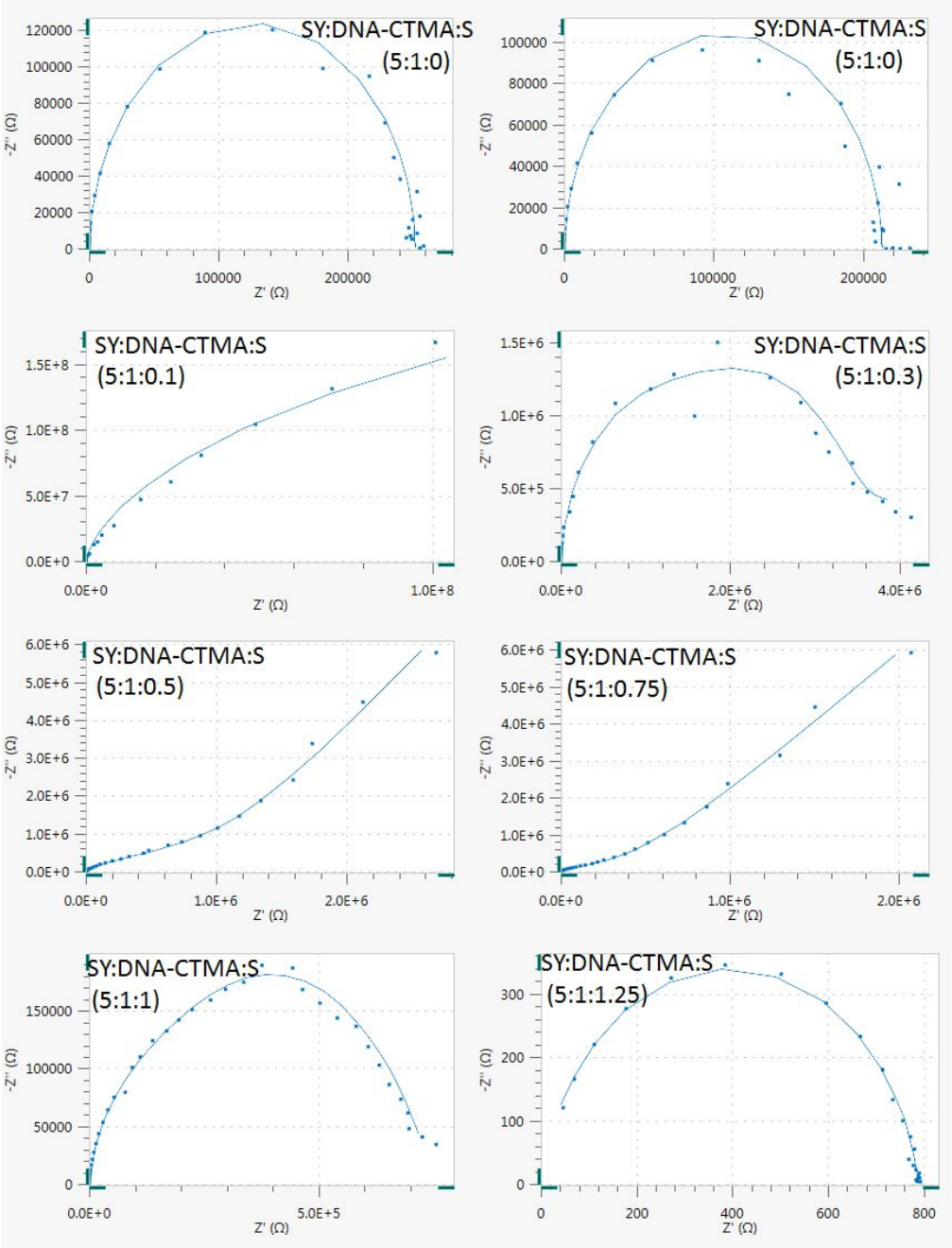

Figure 8.7 The Nyquist plots of impedance spectra and fitting curves for SY:DNA-CTMA:salt blends.

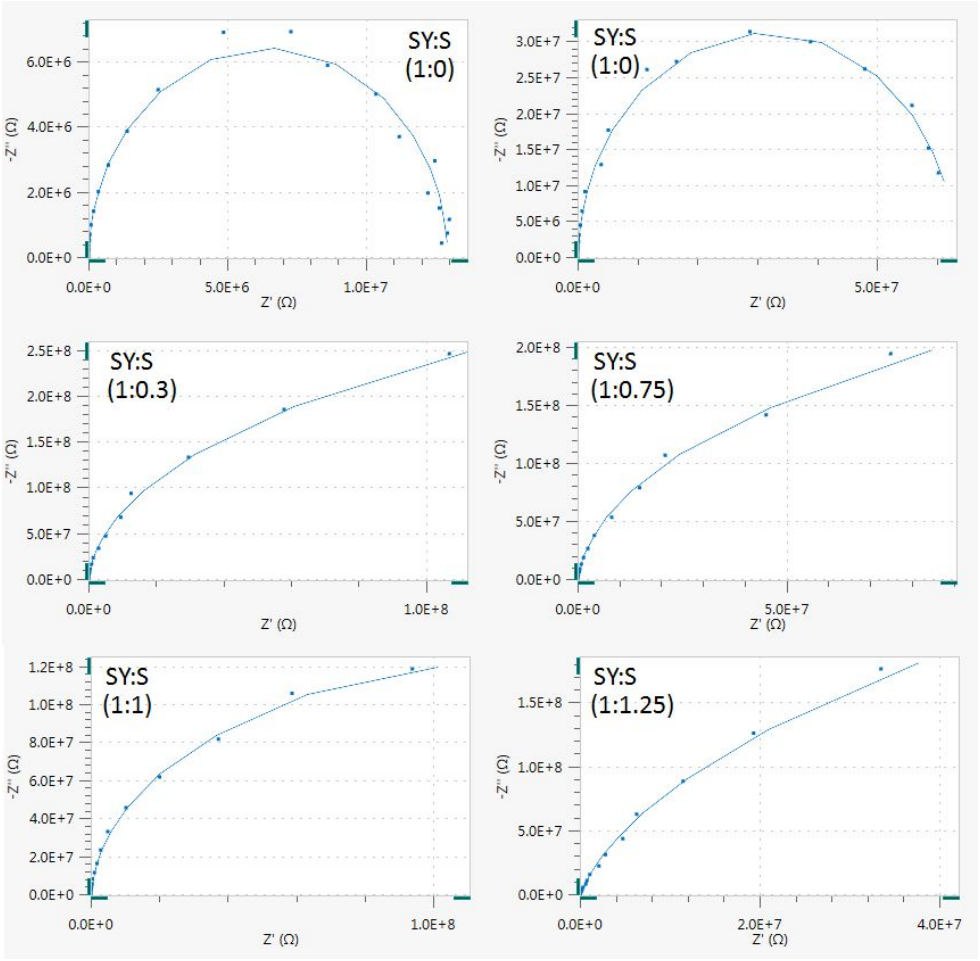

Figure 8.8 The Nyquist plots of impedance spectra and fitting curves for SY:salt mixtures.

Table 8.3 The ionic conductivity results of DNA and DNA-CTMA based SPEs.

	ratio	R_b Ω	R_i	R_{gb}	Thickness nm	Conductivity S/cm
DNA		$38.4x10^3$			94.59	$1.02x10^{-9}$
		$163 x10^3$			94.59	$2.41 x10^{-10}$
		$44.6x10^3$			90.96	$8.49 x10^{-10}$
		$340x10^3$			90.96	$1.11 x10^{-10}$
DNA-CTMA		1130			77.71	$2.86 x10^{-8}$
		517			77.71	$6.26 x10^{-8}$
		353			79.75	$9.41 x10^{-8}$
		988			79.75	$3.36 x10^{-8}$
DNA-CTMA:S	[1:0.1]		$18.6 x10^3$	$17.2 x10^3$	46.67	$1.04 x10^{-9}$
			$18.2 x10^3$	$18 x10^3$	52.18	$1.19 x10^{-9}$
			$7.12 x10^3$	$7.15 x10^3$	52.18	$3.05 x10^{-9}$
DNA-CTMA:S	[1:0.3]		$32.2 x10^3$	$32.2 x10^3$	32.81	$4.24 x10^{-10}$
			$28.5 x10^3$	$27.6 x10^3$	40.6	$5.93 x10^{-10}$
			$19 x10^3$	$268 x10^3$	33.67	$7.38 x10^{-10}$
			$15.9 x10^3$	$163 x10^3$	30.69	$8.04 x10^{-10}$
	[1:0.5]		$33.9 x10^3$	$34.1 x10^3$	36.6	$4.49 x10^{-12}$
			$214 x10^3$	$172 x10^3$	36.6	$7.12 x10^{-11}$
	[1:0.75]		$11.4 x10^3$	$80.7 x10^3$	44.28	$1.61 x10^{-9}$
			$625 x10^3$	$634 x10^3$	46.03	$3.06 x10^{-11}$
			$36.8 x10^3$	$181 x10^3$	46.67	$5.28 x10^{-10}$
	[1:1]		$3.78 x10^3$	$4.23 x10^3$	41.77	$4.6 x10^{-9}$
			$14.2 x10^3$	$3.78 x10^3$	41.18	$1.2 x10^{-9}$
			$8.99 x10^3$	$23.7 x10^3$	41.18	$1.9 x10^{-9}$

Table 8.4 The ionic conductivity results of SY:DNA-CTMA:salt blends.

ratio	R_b Ω	R_i	R_{gb}	Thickness nm	Conductivity S/cm
[5:1:0]	$213 x10^3$			78.9	$1.54x10^{-10}$
	$253 x10^3$			78.9	$1.29x10^{-10}$
[5:1:0.1]		$6.4 x10^6$	$193 x10^6$	76.4	$4.97 x10^{-12}$
		$22.9 x10^6$	$373 x10^6$	76.4	$1.39 x10^{-12}$
[5:1:0.3]		$131 x10^3$	$3.98 x10^6$	61.6	$1.95x10^{-10}$
		$709x10^3$	$804x10^3$	67.9	$3.99x10^{-11}$
		$663x10^3$	$1.24 x10^6$	61.6	$3.87x10^{-11}$
[5:1:0.5]		$243 x10^3$	$1.83 x10^6$	78.7	$1.34x10^{-10}$
		$84.9 x10^3$	$1.35 x10^6$	78.7	$3.86x10^{-10}$
		$87.9 x10^3$	$1.27 x10^6$	85.13	$4.03x10^{-10}$
		$84.6 x10^3$	$1.16 x10^6$	85.13	$4.19 x10^{-10}$
[5:1:0.75]		$44.7 x10^3$	$770 x10^3$	66.32	$6.18 x10^{-10}$
		$56.4 x10^3$	$673 x10^3$	66.32	$4.89 x10^{-10}$
		$45.2x10^3$	$613x10^3$	69.6	$6.41 x10^{-10}$
		$119 x10^3$	$121 x10^3$	69.6	$2.43 x10^{-10}$
[5:1:1]		$67.8 x10^3$	$687.5 x10^3$	69.2	$4.25 x10^{-10}$
[5:1:1.25]	791			73.27	$3.85x10^{-8}$
		$13.2 x10^3$	$14 x10^3$	66.5	$2.09x10^{-9}$
		$11.5x10^3$	$12.2 x10^3$	72.34	$2.62x10^{-9}$
		$9.68 x10^3$	$33.6 x10^3$	72.34	$3.11 x10^{-9}$

Table 8.5 The ionic conductivity results of SY:salt blends. The layer thickness is 90 nm for the all samples.

Ratio [SY:x]	R_b Ω	Thickness nm	Conductivity S/cm
5:0	$13x10^6$	90	$2.88x10^{-12}$
	$63.2\ x10^6$	90	$5.93x10^{-13}$
[5:0.1]	$416\ x10^6$	90	$9.01x10^{-14}$
	$514\ x10^6$	90	$7.29x10^{-14}$
	$524x10^6$	90	$7.13x10^{-14}$
[5:0.3]	$2.77\ x10^6$	90	$1.35x10^{-11}$
	$691\ x10^6$	90	$5.42x10^{-14}$
	$4.23\ x10^6$	90	$8.86x10^{-12}$
[5:0.5]	$88.3\ x10^6$	90	$4.24x10^{-13}$
	$12.8\ x10^6$	90	$2.92x10^{-12}$
	$3.30\ x10^6$		$1.13x10^{-11}$
[5:0.75]	$74.8\ x10^6$		$5.01x10^{-13}$
	$593\ x10^6$		$6.32x10^{-14}$
	$526\ x10^6$		$7.12x10^{-14}$
	$1.51\ x10^9$		$2.48x10^{-14}$
[5:1]	$66.7\ x10^6$		$5.62x10^{-13}$
	$257\ x10^6$		$1.45x10^{-13}$
	$1.09\ x10^9$		$3.44x10^{-14}$
	$1.18\ x10^9$		$3.17x10^{-14}$
[5:1.25]	$2.06\ x10^9$		$1.82x10^{-14}$
	$1.26\ x10^9$		$2.97x10^{-14}$

8.6 While light interferometry images of SY:salt blends

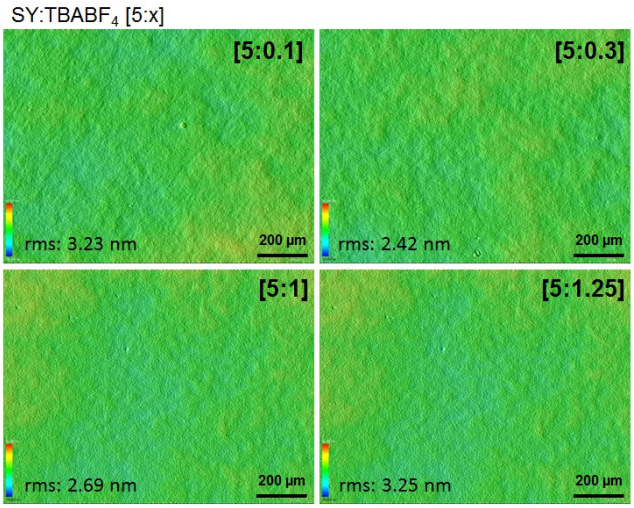

Figure 8.9 Representative white light interferometric maps for SY:salt blends.

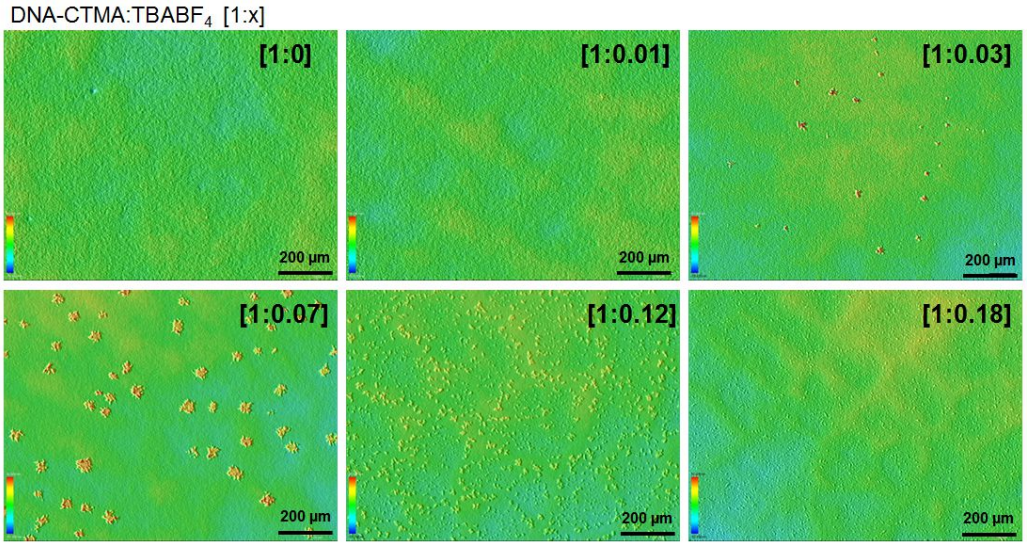

Figure 8.10 White light interferometry topography images of DNA-CTMA SPEs with reduced salt content.

BIBLIOGRAPHY

[1] M. Irimia-Vladu, "'Green' electronics: biodegradable and biocompatible materials and devices for sustainable future," *Chem. Soc. Rev.*, vol. 43, no. 2, pp. 588–610, 2014.

[2] Y. K. Jung *et al.*, "3 Stacked Top Emitting White OLED for High Resolution OLED TV," pp. 707–710, 2016.

[3] M. B. Panish, "Molecular Beam Epitaxy," *Science*, vol. 208, pp. 916–922, 1980.

[4] M. S. Branham, J. B. Dahmus, and A. J. Jones, "Thermodynamic Analysis of Processes," vol. 43, no. 5, pp. 1584–1590, 2009.

[5] A. Heeger, A. G. MacDiarmid, and H. Shirakawa, "The Nobel Prize in chemistry, 2000: conductive polymers," *Stock. Sweden R. Swedish Acad. Sci.*, pp. 1–16, 2000.

[6] J. Hast *et al.*, "Roll-to-Roll manufacturing of printed OLEDs," *Dig. Tech. Pap. - SID Int. Symp.*, vol. 44, no. 1, pp. 192–195, 2013.

[7] OE-A, *Organic Printed Electronics: Application, Technologies, Supliers*, 7th ed. Frankfurt am Main: VDMA Verlag GmbH, 2017.

[8] C. W. Tang and S. a. Vanslyke, "Organic electroluminescent diodes," *Appl. Phys. Lett.*, vol. 51, no. 12, pp. 913–915, 1987.

[9] The StEP Initiative, "Solving the E-Waste Problem (Step) White Paper One Global Definition of E-waste," 2014. [Online]. Available: http://www.step-initiative.org/files/step/_documents/StEP_WP_One Global Definition of E-waste_20140603_amended.pdf.

[10] K. Breivik, J. M. Armitage, F. Wania, A. J. Sweetman, and K. C. Jones, "Tracking the Global Distribution of Persistent Organic Pollutants Accounting for E-Waste Exports to Developing Regions," *Environ. Sci. Technol.*, vol. 50, no. 2, pp. 798–805, 2016.

[11] P. Modak, "Towards a Green Economy," *Waste: investing in energy and resource efficiency.*, 2011. [Online]. Available: https://www.unilever.com.sg/Images/waste-investing-in-energy-and-resource-efficiency-sgp_tcm1312-507943_en.pdf.

[12] M. Heacock, C. B. Kelly, and K. A. Asante, "E-waste and harm to vulnerable populations: a growing global problem.," *Env. Heal. Perspect 205 doi 101289ehp1509699*, vol. 550, no. 5, pp. 550–555, 2015.

[13] International Energy Agency (IEA), "Light's Labour's Lost: Policies for Energy-efficient

Lighting," 2006. [Online]. Available: http://www.iea.org/publications/freepublications/publication/name,3644,en.html. [Accessed: 16-Apr-2018].

[14] F. So, J. Kido, and P. Burrows, "Organic Light- Emitting Devices for Solid-State Lighting Introduction : The Potential for," *Mrs Bull.*, vol. 33, no. July, pp. 663–669, 2008.

[15] Q. Pei, G. Yu, C. Zhang, Y. Yang, and A. J. Heeger, "Polymer Light-Emitting Electrochemical Cells," *Science*, vol. 269, pp. 1086–1088, 1995.

[16] R. D. Costa, Ed., *Light-emitting electrochemical cells: Concepts, advances and challenges*, 1st ed. Switzerland: Springer International Publishing AG, 2017.

[17] K. Sato *et al.*, "Low-Cost, Organic Light-Emitting Electrochemical Cells with Mass-Producible Nanoimprinted Substrates Made Using Roll-to-Roll Methods," *Adv. Mater. Technol.*, vol. 2, no. 5, 2017.

[18] H. Shirakawa, J. Louis, and A. G. Macdiarmid, "Synthesis of Electrically Conducting Organic Polymers : Halogene Derivatives of Polyacetylene, (CH)x," *J. C. S. Chem. Comm*, no. 578, pp. 578–580, 1977.

[19] C. Brütting, W., Adachi, Ed., *Physics of Organic Semiconductors*. Weinheim: Wiley-VCH, 2012.

[20] H. Bässler, "Charge Transport in Disordered Organic Photoconductors a Monte Carlo Simulation Study," *Phys. Status Solidi*, vol. 175, no. 1, pp. 15–56, 1993.

[21] Y.-L. Chang, Ed., *Efficient Organic Light Emitting Diodes (OLEDs)*. Singapore: Pan Stanford.

[22] "LG's 65-inch rollable OLED TV," 2018. [Online]. Available: https://www.theverge.com/2018/1/6/16859102/lg-display-rollable-oled-65-inch-ces-2018. [Accessed: 24-Jul-2018].

[23] "Transparent OLED touch display," *MMT GmbH & Co. KG.*, 2018. [Online]. Available: https://www.mmt.io/transparent-oled-touch-screen-display/. [Accessed: 24-Jul-2018].

[24] "Sony's new wearable display," 2014. [Online]. Available: https://www.pcworld.com/article/2860592/sony-highres-oled-screen-attaches-to-any-eyewear.html. [Accessed: 24-Jul-2018].

[25] T. Yokota *et al.*, "Ultraflexible organic photonic skin," *Sci. Adv.*, vol. 2, no. 4, p. e1501856, 2016.

[26] J. Lee, M. Slootsky, K. Lee, Y. Zhang, and S. R. Forrest, "An electrophosphorescent organic light emitting concentrator," *Light Sci. Appl.*, vol. 3, no. February, pp. 1–5, 2014.

[27] M. Pope, H. P. Kallmann, and P. Magnante, “Electroluminescence in Organic Crystals,” *J. Chem. Phys.*, vol. 38, no. 8, p. 2042, 1963.

[28] B. W. D’Andrade and S. R. Forrest, “White organic light-emitting devices for solid-state lighting,” *Adv. Mater.*, vol. 16, no. 18, pp. 1585–1595, 2004.

[29] A. Misra, P. Kumar, M. N. Kamalasanan, and S. Chandra, “White organic LEDs and their recent advancements,” *Semicond. Sci. Technol.*, vol. 21, no. 7, 2006.

[30] J. H. Burroughes *et al.*, “Light-emitting diodes based on conjugated polymers,” *Nature*, vol. 347, pp. 539–541, 1990.

[31] J. H. Burroughes, C. A. Jones, and R. H. Friend, “New semiconductor device physics in polymer diodes and transistors,” *Nature*, vol. 335, pp. 137–141, 1988.

[32] A. J. Harris, R. S. Walker, R. Sneddon, A. J. H. R. S. Walker, and R. Sneddon, “Current-voltage characteristics of amorphous silicon P-N junctions current-voltage characteristics of amorphous silicon p-n junctions,” vol. 51, no. 1980, pp. 4287–4290, 1980.

[33] K. Müllen and U. Scherf, Eds., *Organic Light-Emitting Devices. Snythesis, Properties and Applications*. Weinheim: Wiley-VCH Verlag, 2006.

[34] M. A. Lampert and P. Mark, *Current Injection in Solids*. New York: Academic Press, 1970.

[35] W. Schottky, “Halbleitertheorie der Sperrschicht,” *Z. Phys.*, vol. 113, p. 367, 1939.

[36] Y. Shen, A. R. Hosseini, M. H. Wong, and G. G. Malliaras, “How to make ohmic contacts to organic semiconductors,” *ChemPhysChem*, vol. 5, no. 1, pp. 16–25, 2004.

[37] A. J. Campbell, D. D. C. Bradley, and D. G. Lidzey, “Space-charge limited conduction with traps in poly(phenylene vinylene) light emitting diodes,” *J. Appl. Phys.*, vol. 82, no. 12, pp. 6326–6342, 1997.

[38] P. W. M. . Blom and M. J. M. De Jong, “Device operation of polymer light-emitting diodes,” *Philips J. Res.*, vol. 51, no. 4, pp. 479–494, 1998.

[39] L. Pautmeier, R. Richert, and H. Bässler, “Poole-Frenkel behavior of charge transport in organic solids with off-diagonal disorder studied by Monte Carlo simulation,” *Synth. Met.*, vol. 37, no. 1–3, pp. 271–281, 1990.

[40] M. Kuik, L. J. A. Koster, G. A. H. Wetzelaer, and P. W. M. Blom, “Trap-assisted recombination in disordered organic semiconductors,” *Phys. Rev. Lett.*, vol. 107, no. 25, pp. 3–6, 2011.

[41] Y. E. Al Baldo, M. A.; O’Brien, DF; You, “Highly efficient phosphorescent emission from organic electroluminescent devices,” *Nature*, vol. 395, no. 6698, pp. 151–154, 1998.

[42] Y. Cao, I. D. Parker, G. Yu, C. Zhang, and A. J. Heeger, “Improved quantum efficiency for electroluminescence in semiconducting polymers,” *Nature*, vol. 397, no. 6718, pp. 414–415, 1999.

[43] C. Adachi, M. A. Baldo, M. E. Thompson, and S. R. Forrest, “Nearly 100% internal phosphorescence efficiency in an organic light emitting device,” *J. Appl. Phys.*, vol. 90, no. 10, pp. 5048–5051, 2001.

[44] G. Baryshnikov, B. Minaev, and H. Ågren, “Theory and Calculation of the Phosphorescence Phenomenon,” *Chem. Rev.*, vol. 117, no. 9, pp. 6500–6537, 2017.

[45] T. J. Penfold, E. Gindensperger, C. Daniel, and C. M. Marian, “Spin-Vibronic Mechanism for Intersystem Crossing,” *Chem. Rev.*, p. acs.chemrev.7b00617, 2018.

[46] H. Uoyama, K. Goushi, K. Shizu, H. Nomura, and C. Adachi, “Highly efficient organic light-emitting diodes from delayed fluorescence,” *Nature*, vol. 492, no. 7428, pp. 234–238, 2012.

[47] M. Y. Wong and E. Zysman-Colman, “Purely Organic Thermally Activated Delayed Fluorescence Materials for Organic Light-Emitting Diodes,” *Adv. Mater.*, vol. 29, no. 22, 2017.

[48] M. Cocchi *et al.*, “Efficient exciplex emitting organic electroluminescent devices,” *Appl. Phys. Lett.*, vol. 80, no. 13, pp. 2401–2403, 2002.

[49] B. Hu, Z. Yang, and F. E. Karasz, “Electroluminescence of pure poly(N-vinylcarbazole) and its blends with a multiblock copolymer,” *J. Appl. Phys.*, vol. 76, no. 4, pp. 2419–2422, 1994.

[50] D. D. Gebler *et al.*, “Exciplex emission in bilayer polymer light-emitting devices,” *Appl. Phys. Lett.*, vol. 70, no. 13, pp. 1644–1646, 1997.

[51] S. Wehrmeister *et al.*, “Combined electrical and optical analysis of the efficiency roll-off in phosphorescent organic light-emitting diodes,” *Phys. Rev. Appl.*, vol. 3, no. 2, pp. 1–10, 2015.

[52] R. Coehoorn, L. Zhang, P. A. Bobbert, and H. Van Eersel, “Effect of polaron diffusion on exciton-polaron quenching in disordered organic semiconductors,” *Phys. Rev. B*, vol. 95, no. 13, p. 134202, 2017.

[53] K. W. Hershey and R. J. Holmes, “Unified Analysis of Transient and Steady-State Electroluminescence -Establishing an Analytical Formalism for OLED Charge Balance,” *SID Symp. Dig. Tech. Pap.*, vol. 48, no. 1, pp. 115–118, 2017.

[54] T. Förster, “Zwischenmolekulare Energiewanderung und Fluoreszenz,” *Ann. Phys.*, vol. 2, no. 6, pp. 55–75, 1948.

[55] D. L. Dexter, “A theory of sensitized luminescence in solids,” *J. Chem. Phys.*, vol. 21, no. 5, pp. 836–850, 1953.

[56] H. Murata *et al.*, “Molecular Organic Light-Emitting Diodes Based on a Guest-Host Active Layer: Approaches for Enhancing Device Performance,” *Mol. Cryst. Liq. Cryst.*, vol. 353, no. 1, pp. 567–580, 2000.

[57] C. Weichsel, S. Reineke, M. Furno, B. Lssem, and K. Leo, “Organic light-emitting diodes for lighting: High color quality by controlling energy transfer processes in host-guest-systems,” *J. Appl. Phys.*, vol. 111, no. 3, p. 033102, 2012.

[58] D. Y. Zhou, H. Zamani Siboni, Q. Wang, L. S. Liao, and H. Aziz, “Host to guest energy transfer mechanism in phosphorescent and fluorescent organic light-emitting devices utilizing exciplex-forming hosts,” *J. Phys. Chem. C*, vol. 118, no. 41, pp. 24006–24012, 2014.

[59] W. Li, J. Li, F. Wang, Z. Gao, and S. Zhang, “Universal Host Materials for High-Efficiency Phosphorescent and Delayed-Fluorescence OLEDs,” *ACS Appl. Mater. Interfaces*, vol. 7, no. 47, pp. 26206–26216, 2015.

[60] R. Englman and J. Jortner, “The energy gap law for non-radiative decay in large molecules,” *J. Lumin.*, vol. 1–2, no. C, pp. 134–142, 1970.

[61] S. J. He, R. White, D. K. Wang, J. Zhang, N. Jiang, and Z. H. Lu, “A simple organic diode structure with strong rectifying characteristics,” *Org. Electron.*, vol. 15, no. 11, pp. 3370–3374, 2014.

[62] D. Kabra, L. P. Lu, M. H. Song, H. J. Snaith, and R. H. Friend, “Efficient single-layer polymer light-emitting diodes,” *Adv. Mater.*, vol. 22, no. 29, pp. 3194–3198, 2010.

[63] N. C. . Greenham, R. H. . Friend, and D. D. C. Bradley, “Angular Dependence of the Emission from a Conjugated Polymer Light-Emitting Diode : Implications for Efficiency Calculations,” *Adv. Mater.*, vol. 6, no. 6, pp. 491–494, 1994.

[64] J. Kido, M. Kimura, and K. Nagai, “Multilayer white light-emitting organic electroluminescent device.,” *Science*, vol. 267, no. 5202, pp. 1332–4, 1995.

[65] M.-K. Fung, Y.-Q. Li, and L.-S. Liao, “Tandem Organic Light-Emitting Diodes,” *Adv. Mater.*, vol. 28, no. 47, pp. 10381–10408, 2016.

[66] M. J. Park, Y. H. Son, H. I. Yang, S. K. Kim, R. Lampande, and J. H. Kwon, “Optical Design and Optimization of Highly Efficient Sunlight-like Three-Stacked Warm White Organic Light Emitting Diodes,” *ACS Photonics*, vol. 5, pp. 655–662, 2017.

[67] T. Zhang, D. K. Wang, N. Jiang, and Z. H. Lu, “Stacking multiple connecting functional materials in tandem organic light-emitting diodes,” *Sci. Rep.*, vol. 7, pp. 1–8, 2017.

[68] E. Cantatore, Ed., *Applications of Organic and Printed Electronics*. New York: Springer US, 2013.

[69] J. Huang, M. Pfeiffer, A. Werner, J. Blochwitz, K. Leo, and S. Liu, "Low-voltage organic electroluminescent devices using pin structures," *Appl. Phys. Lett.*, vol. 80, no. 1, pp. 139–141, 2002.

[70] M. Pfeiffer, S. R. Forrest, K. Leo, and M. E. Thompson, "Electrophosphorescent p-i-n organic light-emitting devices for very-high-efficiency flat-panel displays," *Adv. Mater.*, vol. 14, no. 22, pp. 1633–1636, 2002.

[71] D. M. Small, W. Y. Sanchez, M. J. Hickey, and G. C. Gobe, "Multiphoton fluorescence microscopy of the live kidney in health and disease Multiphoton fluorescence microscopy of the live kidney in health and disease," *J. Biomed. Opt.*, vol. 19, no. 2, p. 020901, 2014.

[72] N. C. . Greenham and R. H. Friend, "Semiconductor Device Physics of Conjugated Polymers," *Solid State Phys.*, vol. 49, no. 1, pp. 1–149, 1996.

[73] M. M. Richter, F. R. F. Fan, F. Klavetter, A. J. Heeger, and A. J. Bard, "Electrochemistry and electrogenerated chemiluminescence of films of the conjugated polymer 4-methoxy-(2-ethylhexoxyl)-2,5-polyphenylenevinylene," *Chem. Phys. Lett.*, vol. 226, no. 1–2, pp. 115–120, 1994.

[74] P. V. Jaguiro, A. G. Smirnov, and S. K. Kang, "P-24: Liquid-Phase Electroluminescent Displays," in *SID International Symposium Digest of Technical Papers*, 1995, p. p.470.

[75] Q. Pei, Y. Yang, G. Yu, C. Zhang, and A. J. Heeger, "Polymer light-emitting electrochemical cells: In situ formation of a light-emitting p-n junction," *J. Am. Chem. Soc.*, vol. 118, no. 16, pp. 3922–3929, 1996.

[76] Z. Yu, M. Sun, and Q. Pei, "Electrochemical formation of stable p-i-n junction in conjugated polymer thin films," *J. Phys. Chem. B*, vol. 113, no. 25, pp. 8481–8486, 2009.

[77] F.-C. Chen, Y. Yang, and Q. Pei, "Phosphorescent light-emitting electrochemical cell," *Appl. Phys. Lett.*, vol. 81, no. 22, p. 4278, 2002.

[78] N. Kaihovirta, A. Asadpoordarvish, A. Sandström, and L. Edman, "Doping-Induced Self-Absorption in Light-Emitting Electrochemical Cells," *ACS Photonics*, vol. 1, no. 3, pp. 182–189, 2014.

[79] Y. P. Jhang, H. F. Chen, H. B. Wu, Y. S. Yeh, H. C. Su, and K. T. Wong, "Improving device efficiencies of solid-state white light-emitting electrochemical cells by adjusting the emissive-layer thickness," *Org. Electron. physics, Mater. Appl.*, vol. 14, no. 10, pp. 2424–2430, 2013.

[80] X. Li, J. Gao, and G. Liu, "Thickness dependent device characteristics of sandwich polymer

light-emitting electrochemical cell," *Org. Electron. physics, Mater. Appl.*, vol. 14, no. 6, pp. 1441–1446, 2013.

[81] Y. Yang and Q. Pei, "Voltage controlled two color light-emitting electrochemical cells," *Appl. Phys. Lett.*, vol. 68, no. 19, pp. 2708–2710, 1996.

[82] B. K. Crone, I. H. Campbell, P. S. Davids, D. L. Smith, C. J. Neef, and J. P. Ferraris, "Device physics of single layer organic light-emitting diodes," *J. Appl. Phys.*, vol. 86, no. 10, pp. 5767–5774, 1999.

[83] B. Gautier, X. Wu, F. Altal, S. Chen, and J. Gao, "Reverse bias activation of salt-doped polymer light-emitting devices," *Org. Electron. physics, Mater. Appl.*, vol. 28, pp. 47–52, 2016.

[84] Q. Sun, Y. Li, and Q. Pei, "Polymer Light-Emitting Electrochemical Cells for High-Efficiency Low-Voltage Electroluminescent Devices," *J. Disp. Technol.*, vol. 3, no. 2, pp. 211–224, 2007.

[85] Q. . Sun, H. . Wang, C. . Yang, X. . Wang, D. . Liu, and Y. . Li, "Polymer light-emitting electrochemical cells with the block copolymers containing PEO segments," *Thin Solid Films*, vol. 417, no. 1–2, pp. 14–19, 2002.

[86] H. Wang, Q. Sun, Y. Li, and X. Li, "Synthesis of block copolymers with well-defined alternating chromophore and flexible spacer for electroluminescence application," *Thin Solid Films*, vol. 426, no. 1–2, pp. 40–46, 2003.

[87] M. Sun, C. Zhong, F. Li, Y. Cao, and Q. Pei, "A Fluorene−Oxadiazole Copolymer for White Light-Emitting Electrochemical Cells," *Macromolecules*, vol. 43, no. 4, pp. 1714–1718, 2010.

[88] N. Jaballah, K. Hriz, M. Majdoub, M. Jouini, and J.-L. Fave, "New Blue-Photoluminescent Semi-Conducting Polymer Derived from Fluorinated Bisphenol A," *High Perform. Polym.*, vol. 22, no. 4, pp. 483–497, 2010.

[89] S. Tang, J. Pan, H. a. Buchholz, and L. Edman, "White light from a single-emitter light-emitting electrochemical cell," *J. Am. Chem. Soc.*, vol. 135, no. 9, pp. 3647–3652, 2013.

[90] H. C. Su, C. C. Wu, F. C. Fang, and K. T. Wong, "Efficient solid-state host-guest light-emitting electrochemical cells based on cationic transition metal complexes," *Appl. Phys. Lett.*, vol. 89, no. 26, pp. 4–7, 2006.

[91] L. He *et al.*, "Blue-emitting cationic iridium complexes with 2-(1H-pyrazol-1-yl)pyridine as the ancillary ligand for efficient light-emitting electrochemical cells," *Adv. Funct. Mater.*, vol. 18, no. 14, pp. 2123–2131, 2008.

[92] L. He, L. Duan, J. Qiao, G. Dong, L. Wang, and Y. Qiu, "Highly efficient blue-green and

white light-emitting electrochemical cells based on a cationic iridium complex with a bulky side group," *Chem. Mater.*, vol. 22, no. 11, pp. 3535–3542, 2010.

[93] M. Mydlak, C. Bizzarri, D. Hartmann, W. Sarfert, G. Schmid, and C. L. De, "Positively Charged Iridium(III) Triazole Derivatives as Blue Emitters for Light-Emitting Electrochemical Cells," *Adv. Funct. Mater.*, vol. 20, no. Copyright (C) 2011 American Chemical Society (ACS). All Rights Reserved., pp. 1812–1820, 2010.

[94] R. D. Costa, E. Ortí, H. J. Bolink, F. Monti, G. Accorsi, and N. Armaroli, "Luminescent ionic transition-metal complexes for light-emitting electrochemical cells," *Angew. Chemie - Int. Ed.*, vol. 51, no. 33, pp. 8178–8211, 2012.

[95] S. B. Meier *et al.*, "Dynamic doping in planar ionic transition metal complex-based light-emitting electrochemical cells," *Adv. Funct. Mater.*, vol. 23, no. 28, pp. 3531–3538, 2013.

[96] S. Van Reenen, T. Akatsuka, D. Tordera, M. Kemerink, and H. J. Bolink, "Universal transients in polymer and ionic transition metal complex light-emitting electrochemical cells," *J. Am. Chem. Soc.*, vol. 135, no. 2, pp. 886–891, 2013.

[97] A. J. Norell Bader, A. a. Ilkevich, I. V. Kosilkin, and J. M. Leger, "Precise color tuning via hybrid light-emitting electrochemical cells," *Nano Lett.*, vol. 11, no. 2, pp. 461–465, 2011.

[98] M. F. Aygüler, M. D. Weber, B. M. D. Puscher, D. D. Medina, P. Docampo, and R. D. Costa, "Light-Emitting Electrochemical Cells Based on Hybrid Lead Halide Perovskite Nanoparticles," *J. Phys. Chem. C*, vol. 119, no. 21, pp. 12047–12054, 2015.

[99] J. Liu, J. Oliva, K. Tong, F. Zhao, D. Chen, and Q. Pei, "Multi-colored light-emitting electrochemical cells based on thermal activated delayed fluorescence host," *Sci. Rep.*, vol. 7, no. 1, pp. 1–8, 2017.

[100] M. Y. Wong, M.-G. La-Placa, A. Pertegas, H. J. Bolink, and E. Zysman-Colman, "Deep-blue thermally activated delayed fluorescence (TADF) emitters for light-emitting electrochemical cells (LEECs)," *J. Mater. Chem. C*, vol. 5, no. 7, pp. 1699–1705, 2017.

[101] P. Lundberg, E. M. Lindh, S. Tang, and L. Edman, "Toward Efficient and Metal-Free Emissive Devices: A Solution-Processed Host-Guest Light-Emitting Electrochemical Cell Featuring Thermally Activated Delayed Fluorescence," *ACS Appl. Mater. Interfaces*, vol. 9, no. 34, pp. 28810–28816, 2017.

[102] T. J. Mills and M. C. Lonergan, "Charge injection and transport in low-mobility mixed ionic/electronic conducting systems: Regimes of behavior and limiting cases," *Phys. Rev. B - Condens. Matter Mater. Phys.*, vol. 85, no. 3, pp. 1–19, 2012.

[103] P. Matyba, K. Maturova, M. Kemerink, N. D. Robinson, and L. Edman, "The dynamic organic p-n junction.," *Nat. Mater.*, vol. 8, no. 8, pp. 672–676, 2009.

[104] P. W. M. Blom, M. J. M. De Jong, and J. J. M. Vleggaar, “Electron and hole transport in poly(p-phenylene vinylene) devices,” *Appl. Phys. Lett.*, vol. 68, no. 23, pp. 3308–3310, 1996.

[105] D. B. Rodovsky, O. G. Reid, L. S. C. Pingree, and D. S. Ginger, “Concerted emission and local potentiometry of light-emitting electrochemical cells,” *ACS Nano*, vol. 4, no. 5, pp. 2673–2680, 2010.

[106] J. C. deMello, “Organic Electronics: What’s in a name ?,” *Nat. Mater.*, vol. 6, no. November, pp. 796–797, 2007.

[107] L. S. C. Pingree, D. B. Rodovsky, D. C. Coffey, G. P. Bartholomew, and D. S. Ginger, “Scanning Kelvin Probe imaging of the potential profiles in fixed and dynamic planar LECs,” *J. Am. Chem. Soc.*, vol. 129, no. 51, pp. 15903–15910, 2007.

[108] J. C. DeMello, J. J. M. Halls, S. C. Graham, N. Tessler, and R. H. Friend, “Electric field distribution in polymer light-emitting electrochemical cells,” *Phys. Rev. Lett.*, vol. 85, no. 2, pp. 421–424, 2000.

[109] S. van Reenen, P. Matyba, A. Dzwilewski, R. A. J. Janssen, L. Edman, and M. Kemerink, “A Unifying Model for the Operation of Light-Emitting Electrochemical Cells,” *J. Am. Chem. Soc.*, vol. 132, no. 39, pp. 13776–13781, 2010.

[110] G. Gozzi, L. F. Santos, and R. M. Faria, “Transient and d.c. analysis of the operation mechanism of light-emitting electrochemical cells,” *Epl*, vol. 100, no. 1, 2012.

[111] G. Yu, Y. Cao, C. Zhang, Y. Li, J. Gao, and A. J. Heeger, “Complex admittance measurements of polymer light-emitting electrochemical cells: Ionic and electronic contributions,” *Appl. Phys. Lett.*, vol. 73, no. 1, pp. 111–113, 1998.

[112] X. Li, F. Altal, G. Liu, and J. Gao, “Long-term, intermittent testing of sandwich polymer light-emitting electrochemical cells,” *Appl. Phys. Lett.*, vol. 103, no. 24, p. 243304, 2013.

[113] P. G. Bruce, “Structure and Electrochemistry of Polymer Electrolytes,” *Electrochim. Acta*, vol. 40, no. 13, pp. 2077–2085, 1995.

[114] S. Van Reenen, R. A. J. Janssen, and M. Kemerink, “Dynamic processes in sandwich polymer light-emitting electrochemical cells,” *Adv. Funct. Mater.*, vol. 22, no. 21, pp. 4547–4556, 2012.

[115] S. Tang, J. Mindemark, C. M. G. Araujo, D. Brandell, and L. Edman, “Identifying key properties of electrolytes for light-emitting electrochemical cells,” *Chem. Mater.*, vol. 26, no. 17, pp. 5083–5088, 2014.

[116] J. Mindemark, S. Tang, J. Wang, N. Kaihovirta, D. Brandell, and L. Edman, “High-Performance Light-Emitting Electrochemical Cells by Electrolyte Design,” *Chem. Mater.*,

vol. 28, no. 8, pp. 2618–2623, 2016.

[117] J. Mindemark and L. Edman, “Illuminating the electrolyte in light-emitting electrochemical cells,” *J. Mater. Chem. C*, vol. 4, no. 3, pp. 420–432, 2016.

[118] S. B. Aziz, T. J. Woo, M. F. Z. Kadir, and H. M. Ahmed, “A Conceptual Review on Polymer Electrolytes and Ion Transport Models,” *J. Sci. Adv. Mater. Devices*, vol. 3, no. 1, pp. 1–17, 2018.

[119] C. S. Tsai, S. H. Yang, B. C. Liu, and H. C. Su, “Single-component polyfluorene electrolytes bearing different counterions for white light-emitting electrochemical cells,” *Org. Electron. physics, Mater. Appl.*, vol. 14, no. 2, pp. 488–499, 2013.

[120] Y. Shao, “Ionic Liquid Used in Long-Lifetime Polymer Light-Emitting Electrochemical Cells,” 2006.

[121] D. L. Smith, “Steady state model for polymer light-emitting electrochemical cells,” *J. Appl. Phys.*, vol. 81, no. 6, pp. 2869–2880, 1997.

[122] J. H. Shin, N. D. Robinson, S. Xiao, and L. Edman, “Polymer light-emitting electrochemical cells: Doping concentration, emission-zone position, and turn-on time,” *Adv. Funct. Mater.*, vol. 17, no. 11, pp. 1807–1813, 2007.

[123] S. Van Reenen, P. Matyba, A. Dzwilewski, R. A. J. Janssen, L. Edman, and M. Kemerink, “Salt concentration effects in planar light-emitting electrochemical cells,” *Adv. Funct. Mater.*, vol. 21, no. 10, pp. 1795–1802, 2011.

[124] S. B. Meier, D. Hartmann, D. Tordera, H. J. Bolink, A. Winnacker, and W. Sarfert, “Dynamic doping and degradation in sandwich-type light-emitting electrochemical cells,” *Phys. Chem. Chem. Phys.*, vol. 14, no. 31, pp. 10886–10890, 2012.

[125] J. Slinker, D. Bernards, P. L. Houston, H. D. Abruña, S. Bernhard, and G. G. Malliaras, “Solid-state electroluminescent devices based on transition metal complexes,” *Chem. Commun.*, no. 19, pp. 2392–2399, 2003.

[126] S. Tang and L. Edman, “Quest for an Appropriate Electrolyte for High-Performance Light-Emitting Electrochemical Cells,” *J. Phys. Chem. Lett.*, vol. 1, no. 18, pp. 2727–2732, 2010.

[127] P. Matyba, M. R. Andersson, and L. Edman, “On the desired properties of a conjugated polymer-electrolyte blend in a light-emitting electrochemical cell,” *Org. Electron. physics, Mater. Appl.*, vol. 9, no. 5, pp. 699–710, 2008.

[128] J. H. Shin, S. Xiao, and L. Edman, “Polymer light-emitting electrochemical cells: The formation and effects of doping-induced micro shorts,” *Adv. Funct. Mater.*, vol. 16, no. 7, pp. 949–956, 2006.

[129] G. Gustafsson, G. M. Treacy, Y. Cao, F. Klavetter, N. Colaneri, and A. J. Heeger, “The ‘plastic’ led: A flexible light-emitting device using a polyaniline transparent electrode,” *Synth. Met.*, vol. 57, no. 1, pp. 4123–4127, 1993.

[130] G. Gu, P. E. Burrows, S. Venkatesh, and S. R. Forrest, “Vacuum-deposited , nonpolymeric flexible organic light-emitting devices,” *Opt. Lett.*, vol. 22, no. 3, pp. 172–174, 1997.

[131] T. Minakata *et al.*, “16.4: Fully R2R-Processed Flexible OLEDs for Lighting,” in *SID International Symposium Digest of Technical Papers*, 2015, no. 1, pp. 219–222.

[132] A. C, B. Luszcynska, B. G. R. Dupont, and Z. Sieradzki, “Inkjet Printing Technique and Its Application in Organic Light Emitting Diodes,” *Disp. Imaging*, vol. 2, pp. 339–358, 2017.

[133] E. Böhm *et al.*, “57-1: Ink-Jet-Printed OLED Displays,” in *SID International Symposium Digest of Technical Papers*, 2017, pp. 842–844.

[134] D. H. Lee, J. S. Choi, H. Chae, C. H. Chung, and S. M. Cho, “Screen-printed white OLED based on polystyrene as a host polymer,” *Curr. Appl. Phys.*, vol. 9, no. 1, pp. 161–164, 2009.

[135] P. Kopola, M. Tuomikoski, R. Suhonen, and A. Maaninen, “Gravure printed organic light emitting diodes for lighting applications,” *Thin Solid Films*, vol. 517, no. 19, pp. 5757–5762, 2009.

[136] S. Raupp *et al.*, “Slot Die Coated and Flexo Printed Highly Efficient SMOLEDs,” *Adv. Mater. Technol.*, vol. 2, no. 2, p. 1600230, 2017.

[137] S. Olberding, M. Wessely, and J. Steimle, “PrintScreen : Fabricating Highly Customizable Thin - film Touch - Displays,” in *UIST’14*, 2014, pp. 281–290.

[138] J. A. Rogers *et al.*, “Paper-like electronic displays: Large-area rubber-stamped plastic sheets of electronics and microencapsulated electrophoretic inks,” *Proc. Natl. Acad. Sci.*, vol. 98, no. 9, pp. 4835–4840, 2001.

[139] S. M. Jo and B. D. Chin, “S4.3 : Printed Circuit and OLED on Foldable Paper Substrates,” in *Proceedings: EuroDisplay 2015*, 2015, p. 19.

[140] I. Verboven, J. Stryckers, V. Mecnika, G. Vandevenne, M. Jose, and W. Deferme, “Printing Smart Designs of Light Emitting Devices with Maintained Textile Properties,” *Materials (Basel).*, vol. 11, no. 2, p. 290, 2018.

[141] A. Sandström, H. F. Dam, F. C. Krebs, and L. Edman, “Ambient fabrication of flexible and large-area organic light-emitting devices using slot-die coating,” *Nat. Commun.*, vol. 3, p. 1002, 2012.

[142] A. Sandström, A. Asadpoordarvish, J. Enevold, and L. Edman, “Spraying light: Ambient-air

fabrication of large-area emissive devices on complex-shaped surfaces," *Adv. Mater.*, vol. 26, no. 29, pp. 4975–4980, 2014.

[143] T. Lanz, A. Sandström, S. Tang, P. Chabrecek, U. Sonderegger, and L. Edman, "A light-emission textile device: Conformal spray-sintering of a woven fabric electrode," *Flex. Print. Electron.*, vol. 1, no. 2, pp. 1–5, 2016.

[144] Z. Shu, O. Pabst, E. Beckert, R. Eberhardt, and A. Tünnermann, "Inkjet Printed Organic Light-emitting Electrochemical Cells for Disposable Lab-on-chip Applications Manufactured at Ambient Atmosphere," *Mater. Today Proc.*, vol. 3, no. 3, pp. 733–738, 2016.

[145] W. Wu, "Inorganic nanomaterials for printed electronics: a review," *Nanoscale*, vol. 9, no. 22, pp. 7342–7372, 2017.

[146] L. Akcelrud, "Electroluminescent polymers," *Prog. Polym. Sci.*, vol. 28, no. 6, pp. 875–962, 2003.

[147] N. I. Craciun, J. Wildeman, and P. W. M. Blom, "Substituted polyfluorene-based hole transport layer with tunable solubility," *J. Phys. Chem. C*, vol. 114, no. 23, pp. 10559–10564, 2010.

[148] M. Petzoldt, "Fluorenbasierte Materialien für die Organische Elektronik und Sensorik," Ruprecht-Karls-Universität Heidelberg, 2015.

[149] S. H. Oh, S. I. Na, Y. C. Nah, D. Vak, S. S. Kim, and D. Y. Kim, "Novel cationic water-soluble polyfluorene derivatives with ion-transporting side groups for efficient electron injection in PLEDs," *Org. Electron. physics, Mater. Appl.*, vol. 8, no. 6, pp. 773–783, 2007.

[150] A. Garcia, R. C. Bakus, P. Zalar, C. V. Hoven, J. Z. Brzezinski, and T. Q. Nguyen, "Controlling ion motion in polymer light-emitting diodes containing conjugated polyelectrolyte electron injection layers," *J. Am. Chem. Soc.*, vol. 133, no. 8, pp. 2492–2498, 2011.

[151] R. E. Franklin and R. G. Gosling, "Molecular Configuration in Sodium Thymonucleate," *Nature*, vol. 171, pp. 740–741, 1953.

[152] J. Watson and F. Crick, "Molecular structure of nucleic acids," *Nature.*, vol. 171, pp. 737–738, 1953.

[153] X. Liu, Q. Fan, and W. Huang, "DNA biosensors based on water-soluble conjugated polymers," *Biosens. Bioelectron.*, vol. 26, no. 5, pp. 2154–2164, 2011.

[154] B. Liu and G. C. Bazan, "Interpolyelectrolyte Complexes of Conjugated Copolymers and DNA: Platforms for Multicolor Biosensors," *J. Am. Chem. Soc.*, vol. 126, no. 7, pp. 1942–1943, 2004.

[155] J. Marmur and P. Doty, “Determination of the base composition of deoxyribonucleic acid from its thermal denaturation temperature,” *J. Mol. Biol.*, vol. 5, no. 1, pp. 109–118, 1962.

[156] K. Tanaka and Y. Okahata, “A DNA-lipid complex in organic media and formation of an aligned cast film,” *J. Am. Chem. Soc.*, vol. 118, no. 44, pp. 10679–10683, 1996.

[157] L. K. Mao *et al.*, “Pentacene organic thin-film transistors with solution-based gelatin dielectric,” *Org. Electron. physics, Mater. Appl.*, vol. 14, no. 4, pp. 1170–1176, 2013.

[158] S. Budavari, Ed., *Product information of gelatin*, 12th ed. Merck, 1996.

[159] G. Hernandez-Sosa *et al.*, “The compromises of printing organic electronics: A case study of gravure-printed light-emitting electrochemical cells,” *Adv. Mater.*, vol. 26, no. 20, pp. 3235–3240, 2014.

[160] A. Pawlicka, A. Firmino, D. Vieira, F. Sentanin, J. G. Grote, and F. Kajzar, “Gelatin- and DNA-based ionic conducting membranes for electrochromic devices,” in *SPIE*, 2009, vol. 7487, p. 74870J.

[161] R. McKENNELL, “Cone-Plate Viscometer Comparison with Coaxial Cylinder Viscometer,” *Anal. Chem.*, vol. 28, no. 11, pp. 1710–1714, 1954.

[162] J. R. Lakowicz, *Principles of Fluorescence Spectroscopy*. New York: Springer, 2006.

[163] C. M. Cardona, W. Li, A. E. Kaifer, D. Stockdale, and G. C. Bazan, “Electrochemical considerations for determining absolute frontier orbital energy levels of conjugated polymers for solar cell applications,” *Adv. Mater.*, vol. 23, no. 20, pp. 2367–2371, 2011.

[164] R. Memming, *Semiconductor Electrochemistry*, 2nd ed. Weinheim, Germany: Wiley-VCH Verlag, 2015.

[165] B. Cappella and G. Dietler, “Force-distance curves by atomic force microscopy,” *Surf. Sci. Rep.*, vol. 34, no. 1–3, pp. 1–104, 1999.

[166] S. Tekoglu, G. Hernandez-Sosa, E. Kluge, U. Lemmer, and N. Mechau, “Gravure printed flexible small-molecule organic light emitting diodes,” *Org. Electron. physics, Mater. Appl.*, vol. 14, no. 12, pp. 3493–3499, 2013.

[167] D. Y. Chung, J. Huang, D. D. C. Bradley, and A. J. Campbell, “High performance, flexible polymer light-emitting diodes (PLEDs) with gravure contact printed hole injection and light emitting layers,” *Org. Electron. physics, Mater. Appl.*, vol. 11, no. 6, pp. 1088–1095, 2010.

[168] G. Hernandez-Sosa *et al.*, “Rheological and drying considerations for uniformly gravure-printed layers: Towards large-area flexible organic light-emitting diodes,” *Adv. Funct.*

Mater., vol. 23, no. 25, pp. 3164–3171, 2013.

[169] H. Kipphan, Ed., *Handbook of Print Media: Technologies and Production Methods*. Berlin: Springer, 2001.

[170] N. Bornemann, H. M. Sauer, and E. Dörsam, "Gravure Printed Ultrathin Layers of Small-Molecule Semiconductors on Glass," vol. 55, no. 4, pp. 1–8, 2011.

[171] H. Lee, A. Kim, S. M. Cho, and H. Chae, "Nanoscale Thickness and Roughness Control of Gravure Printed Organic Light Emitting Layer with Poly(N-vinyl carbazole) and Ir(ppy)(3)," *J. Nanosci. Nanotechnol.*, vol. 9, pp. 7278–7282, 2009.

[172] A. Kim, H. Lee, J. Lee, S. M. Cho, and H. Chae, "Bi-layer gravure printed nanoscale thick organic layers for organic light emitting diode.," *J. Nanosci. Nanotechnol.*, vol. 11, no. 1, pp. 546–549, 2011.

[173] F. O. Odongo Ngome, Y. T. Kim, H. D. Lee, Y. H. Kim, T. W. Lee, and C. G. Park, "A correlation between small-molecule dependent nanomorphology and device performance of organic light-emitting diodes with ternary blend emitting layers," *J. Mater. Chem. C*, vol. 5, no. 37, pp. 9761–9769, 2017.

[174] P. G. Saffman and G. Taylor, "The Penetration of a Fluid into a Porous Medium or Hele-Shaw Cell Containing a More Viscous Liquid," *Proc. R. Soc. A Math. Phys. Eng. Sci.*, vol. 245, no. 1242, pp. 312–329, 1958.

[175] A. Wu, D. Yoo, J. K. Lee, and M. F. Rubner, "Solid-state light-emitting devices based on the tris-chelated ruthenium(II) complex: 3. High efficiency devices via a layer-by-layer molecular-level blending approach," *J. Am. Chem. Soc.*, vol. 121, no. 20, pp. 4883–4891, 1999.

[176] A. Kunz, P. W. M. Blom, and J. J. Michels, "Charge carrier trapping controlled by polymer blend phase dynamics," *J. Mater. Chem. C*, vol. 5, no. 12, pp. 3042–3048, 2017.

[177] H. Rudmann and M. F. Rubner, "Single layer light-emitting devices with high efficiency and long lifetime based on tris(2,2′ bipyridyl) ruthenium(II) hexafluorophosphate," *J. Appl. Phys.*, vol. 90, no. 9, pp. 4338–4345, 2001.

[178] J. Yang *et al.*, "Blue pyrene-based AIEgens: inhibited intermolecular π–π stacking through the introduction of substituents with controllable intramolecular conjugation, and high external quantum efficiencies up to 3.46% in non-doped OLEDs," *Mater. Chem. Front.*, vol. 1, no. 1, pp. 91–99, 2017.

[179] E. M. Lindh, A. Sandström, M. R. Andersson, and L. Edman, "Luminescent line art by direct-write patterning," *Light Sci. Appl.*, vol. 5, no. August 2015, p. e16050, 2016.

[180] S. Tang, W.-Y. Tan, X.-H. Zhu, and L. Edman, "Small-molecule light-emitting

electrochemical cells: evidence for in situ electrochemical doping and functional operation.," *Chem. Commun. (Camb).*, vol. 49, no. 43, pp. 4926–8, 2013.

[181] H.-F. Chen, C.-T. Liao, M.-C. Kuo, Y.-S. Yeh, H.-C. Su, and K.-T. Wong, "UV light-emitting electrochemical cells based on an ionic 2,2'-bifluorene derivative," *Org. Electron.*, vol. 13, no. 10, pp. 1765–1773, 2012.

[182] H. J. Bolink, L. Cappelli, E. Coronado, M. Grätzel, and M. K. Nazeeruddin, "Efficient and Stable Solid-State Light-Emitting Electrochemical Cell Using Tris(4,7-diphenyl-1,10-phenanthroline)ruthenium(II) Hexafluorophosphate," *J. Am. Chem. Soc.*, vol. 128, pp. 46–47, 2006.

[183] G. Hernandez-Sosa *et al.*, "The role of the polymer solid electrolyte molecular weight in light-emitting electrochemical cells," *Org. Electron. physics, Mater. Appl.*, vol. 14, no. 9, pp. 2223–2227, 2013.

[184] M. Seiberlich, "Herstellung gedruckter OLEDs auf Basis kleiner kupferbasieter Moleküle," Universität Heidelberg, 2015.

[185] I. H. Campbell, D. L. Smith, C. J. Neef, and J. P. Ferraris, "Capacitance measurements of junction formation and structure in polymer light-emitting electrochemical cells," *Appl. Phys. Lett.*, vol. 72, no. 20, pp. 2565–2567, 1998.

[186] S. Tekoglu *et al.*, "Emissive Polyelectrolytes As Interlayer for Color Tuning and Electron Injection in Solution-Processed Light-Emitting Devices," *ACS Appl. Mater. Interfaces*, vol. 8, no. 11, pp. 7320–7325, 2016.

[187] N. J. Miller and F. A. Leon, "OLED Lighting Products: Capabilities, Challenges, Potential," *Rep. U.S. DOE under Contract - Pacific Northwest Natl. Lab.*, no. May, p. 29, 2016.

[188] S. Altomonte, "Daylight for Energy Savings and Psycho-Physiological Well-Being in Sustainable Built Environments," *J. Sustain. Dev.*, vol. 1, no. 3, pp. 3–16, 2009.

[189] "Bus stop lighting panels." [Online]. Available: https://www.news.com.au/lifestyle/health/feeling-down-look-into-the-bus-stop-light/news-story/dee86b0629a2103a294df6a9c040d233. [Accessed: 25-Jul-2018].

[190] J. H. Jou *et al.*, "Sunlight-style color-temperature tunable organic light-emitting diode," *Appl. Phys. Lett.*, vol. 95, no. 1, pp. 2007–2010, 2009.

[191] C. Zhong, C. Duan, F. Huang, H. Wu, and Y. Cao, "Materials and devices toward fully solution processable organic light-emitting diodes," *Chem. Mater.*, vol. 23, no. 3, pp. 326–340, 2011.

[192] F. Huang, P. I. Shih, C. F. Shu, Y. Chi, and A. K. Y. Jen, "Highly efficient polymer white-light-emitting diodes based on lithium salts doped electron transporting layer," *Adv. Mater.*,

vol. 21, no. 3, pp. 361–365, 2009.

[193] Y. Tian, X. Xu, J. Wang, C. Yao, and L. Li, “Solution-processed white organic light-emitting diodes with enhanced efficiency by using quaternary ammonium salt doped conjugated polyelectrolyte,” *ACS Appl. Mater. Interfaces*, vol. 6, no. 11, pp. 8631–8638, 2014.

[194] H.-F. Chen, C.-T. Liao, T.-C. Chen, H.-C. Su, K.-T. Wong, and T.-F. Guo, “An ionic terfluorene derivative for saturated deep-blue solid state light-emitting electrochemical cells,” *J. Mater. Chem.*, vol. 21, no. 12, p. 4175, 2011.

[195] K. Shanmugasundaram, M. S. Subeesh, C. D. Sunesh, R. K. Chitumalla, J. Jang, and Y. Choe, “Synthesis and photophysical characterization of an ionic fluorene derivative for blue light-emitting electrochemical cells,” *Org. Electron. physics, Mater. Appl.*, vol. 24, pp. 297–302, 2015.

[196] K. Shanmugasundaram, M. S. Subeesh, C. D. Sunesh, and Y. Choe, “Non-doped deep blue light-emitting electrochemical cells from charged organic small molecules,” *RSC Adv.*, vol. 6, no. 34, pp. 28912–28918, 2016.

[197] H. Sasabe and J. Kido, “Development of high performance OLEDs for general lighting,” *J. Mater. Chem. C*, vol. 1, p. 1699, 2013.

[198] A. Köhnen, M. Irion, M. C. Gather, N. Rehmann, P. Zacharias, and K. Meerholz, “Highly color-stable solution-processed multilayer WOLEDs for lighting application,” *J. Mater. Chem.*, vol. 20, no. 16, p. 3301, 2010.

[199] D. T. Simon, E. O. Gabrielsson, K. Tybrandt, and M. Berggren, “Organic Bioelectronics: Bridging the Signaling Gap between Biology and Technology,” *Chem. Rev.*, vol. 116, no. 21, pp. 13009–13041, 2016.

[200] A. Steude, E. C. Witts, G. B. Miles, and M. C. Gather, “Arrays of microscopic organic LEDs for high-resolution optogenetics,” *Sci. Adv.*, vol. 2, no. 5, 2016.

[201] E. Fresta, V. Fernández-Luna, P. B. Coto, and R. D. Costa, “Merging Biology and Solid-State Lighting: Recent Advances in Light-Emitting Diodes Based on Biological Materials,” *Adv. Funct. Mater.*, vol. 1707011, pp. 1–48, 2018.

[202] Y. You, Y. He, P. E. Burrows, S. R. Forrest, N. A. Petasis, and M. E. Thompson, “Fluorophores related to the green fluorescent protein and their use in optoelectronic devices,” *Adv. Mater.*, vol. 12, no. 22, pp. 1678–1681, 2000.

[203] H. Tajima *et al.*, “Light-emitting diodes fabricated from cytochrome c and myoglobin,” *Synth. Met.*, vol. 153, no. 1–3, pp. 29–32, 2005.

[204] K. Nakamura, T. Ishikawa, D. Nishioka, T. Ushikubo, and N. Kobayashi, “Color-tunable multilayer organic light emitting diode composed of DNA complex and tris(8-

hydroxyquinolinato)aluminum," *Appl. Phys. Lett.*, vol. 97, no. 19, 2010.

[205] Y.-W. Kwon, D. Hoon Choi, and J.-I. Jin, "Optical, electro-optic and optoelectronic properties of natural and chemically modified DNAs," *Polym. J.*, vol. 44, no. 12, pp. 1191–1208, 2012.

[206] E. F. Gomez and A. J. Steckl, "Improved performance of OLEDs on cellulose/epoxy substrate using adenine as a hole injection layer," *ACS Photonics*, vol. 2, no. 3, pp. 439–445, 2015.

[207] N. Hendler, E. D. Mentovich, B. Belgorodsky, D. Rimmerman, and S. Richter, "Controlled electroluminescence from films composed of mixed bio-composites and nanotubes," *ChemPhysChem*, vol. 14, no. 18, pp. 4065–4068, 2013.

[208] N. Jürgensen *et al.*, "Solution-Processed Bio-OLEDs with a Vitamin-Derived Riboflavin Tetrabutyrate Emission Layer," *ACS Sustain. Chem. Eng.*, vol. 5, no. 6, pp. 5368–5372, 2017.

[209] Y. F. Liu, M. H. An, Y. G. Bi, D. Yin, J. Feng, and H. B. Sun, "Flexible Efficient Top-Emitting Organic Light-Emitting Devices on a Silk Substrate," *IEEE Photonics J.*, vol. 9, no. 5, 2017.

[210] L. Migliaccio *et al.*, "Eumelanin–PEDOT:PSS Complementing En Route to Mammalian-Pigment-Based Electrodes: Design and Fabrication of an ITO-Free Organic Light-Emitting Device," *Adv. Electron. Mater.*, vol. 3, no. 5, pp. 1–6, 2017.

[211] J. Jin *et al.*, "Chitin Nanofi ber Transparent Paper for Flexible Green Electronics," *Adv. Mater.*, vol. 28, pp. 5169–5175, 2016.

[212] A. Asadpoordarvish *et al.*, "Light-Emitting Paper," *Adv. Funct. Mater.*, p. n/a-n/a, 2015.

[213] B. Liu, W. L. Yu, Y. H. Lai, and W. Huang, "Blue-light-emitting cationic water-soluble polyfluorene derivatives with tunable quaternization degree," *Macromolecules*, vol. 35, no. 13, pp. 4975–4982, 2002.

[214] M. Ramos, A. Valdés, A. Beltrán, and M. Garrigós, "Gelatin-Based Films and Coatings for Food Packaging Applications," *Coatings*, vol. 6, no. 4, p. 41, 2016.

[215] M. Santoro, A. M. Tatara, and A. G. Mikos, "Gelatin carriers for drug and cell delivery in tissue engineering," *J. Control. Release*, vol. 190, pp. 210–218, 2014.

[216] G. Hernandez-Sosa, S. Tekoglu, S. Valouch, U. Lemmer, M. Hamburger, and N. Mechau, "G4.14 Towards Bio-Degradable Light-Emitting Devices," in *MRS Fall*, 2013.

[217] M. Mindroiu *et al.*, "DNA- and DNA-CTMA: novel bio-nanomaterials for application in photonics and in electronics," vol. 8882, pp. 888202-888202–12, 2013.

[218] J. G. Grote *et al.*, “Investigation of polymers and marine-derived DNA in optoelectronics,” *J. Phys. Chem. B*, vol. 108, no. 25, pp. 8584–8591, 2004.

[219] C. Yumusak, T. B. Singh, N. S. Sariciftci, and J. G. Grote, “Bio-organic field effect transistors based on crosslinked deoxyribonucleic acid (DNA) gate dielectric,” *Appl. Phys. Lett.*, vol. 95, no. 26, p. 263304, 2009.

[220] P. Stadler *et al.*, “Organic field-effect transistors and memory elements using deoxyribonucleic acid (DNA) gate dielectric,” *Org. Electron. physics, Mater. Appl.*, vol. 8, no. 6, pp. 648–654, 2007.

[221] Q. Sun *et al.*, “Highly Efficient Quantum-Dot Light-Emitting Diodes with DNA-CTMA as a Combined Hole-Transporting and Electron-Blocking Layer,” *ACS Nano*, vol. 3, no. 3, pp. 737–743, 2009.

[222] P. Zalar *et al.*, “DNA electron injection interlayers for polymer light-emitting diodes,” *J. Am. Chem. Soc.*, vol. 133, no. 29, pp. 11010–11013, 2011.

[223] A. Pawlicka, F. Sentanin, A. Firmino, J. G. Grote, F. Kajzar, and I. Rau, “Ionically conducting DNA-based membranes for eletrochromic devices,” *Synth. Met.*, vol. 161, no. 21–22, pp. 2329–2334, 2011.

[224] C. C. Jayme, J. Kanicki, F. Kajzar, A. F. Nogueira, and A. Pawlicka, “Influence of DNA and DNA-PEDOT: PSS on dye sensitized solar cell performance,” *Mol. Cryst. Liq. Cryst.*, vol. 627, no. 1, pp. 38–48, 2016.

[225] S. Tsuneyasu, R. Takahashi, H. Minami, K. Nakamura, and N. Kobayashi, “Ultrafast Response in AC-Driven Electrochemiluminescent Cell Using Electrochemically Active DNA/Ru(bpy)32+ Hybrid Film with Mesoscopic Structures,” *Sci. Rep.*, vol. 7, no. 1, pp. 1–7, 2017.

[226] R. G. Endres, D. L. Cox, and R. R. P. Singh, “Colloquium: The quest for high-conductance DNA,” *Rev. Mod. Phys.*, vol. 76, no. 1, pp. 195–214, 2004.

[227] G. S. Manning, “The molecular theory of polyelectrolyte solutions with applications to the electrostatic properties of polynucleotides,” *Q. Rev. Biophys.*, vol. 11, no. 2, pp. 179–246, 1978.

[228] D. D. Eley and G. D. Parfitt, “Semiconductivity of organic substances. 9. Nucleic acid in dry state,” *Trans. Faraday Soc.*, vol. 58, pp. 411–415, 1962.

[229] J. C. Genereux and J. K. Barton, “Mechanisms for DNA charge transport,” *Chem. Rev.*, vol. 110, no. 3, pp. 1642–1662, 2010.

[230] L. Xiang, J. L. Palma, C. Bruot, V. Mujica, M. A. Ratner, and N. Tao, “Intermediate tunnelling-hopping regime in DNA charge transport,” *Nat. Chem.*, vol. 7, no. 3, pp. 221–

226, 2015.

[231] M. Fujitsuka and T. Majima, “Charge transfer dynamics in DNA revealed by time-resolved spectroscopy,” *Chem. Sci.*, vol. 8, no. 3, pp. 1752–1762, 2017.

[232] A. J. Storm, J. Van Noort, S. De Vries, and C. Dekker, “Insulating behavior for DNA molecules between nanoelectrodes at the 100 nm length scale,” *Appl. Phys. Lett.*, vol. 79, no. 23, pp. 3881–3883, 2001.

[233] G. N. Yeo, “Investigation of DNA-based Polymer Solid Electrolyte Systems for Light-Emitting Electrochemical Cells,” Karlsruhe Institute of Technology, 2014.

[234] J. Zhan, H. Matsuno, H. Masunaga, H. Ogawa, and K. Tanaka, “Green solid films with tunable mechanical properties made from deoxyribonucleic acid,” *NPG Asia Mater.*, vol. 6, no. 3, pp. e92-5, 2014.

[235] J. R. Wong and F. Shao, “Hole Transport in A-form DNA/RNA Hybrid Duplexes,” *Sci. Rep.*, vol. 7, no. January, pp. 1–8, 2017.

[236] J. R. Arias-Gonzalez, “Single-molecule portrait of DNA and RNA double helices,” *RSC Integr. Biol.*, vol. 6, no. 10, pp. 904–925, 2014.

[237] S. Kim *et al.*, “Water Soluble Photo- and Electroluminescent Alkoxy-Sulfonated Poly(*p* -phenylenes) Synthesized via Palladium Catalysis,” *Macromolecules*, vol. 31, no. 4, pp. 964–974, 1998.

[238] R. A. Huggins, “Simple method to determine electronic and ionic components of the conductivity in mixed conductors a review,” *Ionics (Kiel).*, vol. 8, no. 3–4, pp. 300–313, 2002.

[239] I. Khimji, J. Shin, and J. Liu, “DNA duplex stabilization in crowded polyanion solutions,” *Chem. Commun.*, vol. 49, no. 13, pp. 1306–1308, 2013.

[240] J. Fang, P. Matyba, N. D. Robinson, and L. Edman, “Identifying and alleviating electrochemical side-reactions in light-emitting electrochemical cells,” *J. Am. Chem. Soc.*, vol. 130, no. 13, pp. 4562–4568, 2008.

[241] D. Tordera *et al.*, “Low current density driving leads to efficient, bright and stable green electroluminescence,” *Adv. Energy Mater.*, vol. 3, no. 10, pp. 1338–1343, 2013.

[242] B. Wang, “Investigation of PLGA-based Polymer Solid Electrolyte Systems for Light-Emitting Electrochemical Cells,” Karlsruhe Institute of Technology, 2014.

[243] J. Zimmermann, N. Jürgensen, A. J. Morfa, B. Wang, S. Tekoglu, and G. Hernandez-Sosa, “Poly(lactic-co-glycolic acid) (PLGA) as Ion-Conducting Polymer for Biodegradable Light-Emitting Electrochemical Cells,” *ACS Sustain. Chem. Eng.*, vol. 4, no. 12, pp. 7050–7055,

2016.

[244] J. Gao, Y. Li, G. Yu, and A. J. Heeger, “Polymer light-emitting electrochemical cells with frozen junctions,” *J. Appl. Phys.*, vol. 86, no. 8, pp. 4594–4599, 1999.

[245] N. Jürgensen, J. Zimmermann, A. J. Morfa, and G. Hernandez-Sosa, “Biodegradable Polycaprolactone as Ion Solvating Polymer for Solution-Processed Light-Emitting Electrochemical Cells,” *Sci. Rep.*, vol. 6, no. October, pp. 4–10, 2016.

[246] “Public Policy and Deployment of New Lighting Technologies,” in *Assesment of Solid-State Lighting, Phase Two*, Washington, DC: The National Academies Press, 2017, pp. 11–31.

[247] A. Jung, “Getting Around the EU Ban: Germans Hoarding Traditional Light Bulbs,” *Spiegel Online*, 27-Jul-2009.

[248] “2015 Internationale Year of Light and Light-Based Technologies,” 2015. [Online]. Available: http://www.light2015.org/Home.html.

[249] OLED Association, “Focus on the 6th Annual China OLED Summit,” 2017. [Online]. Available: https://www.oled-a.org/focus-on-the-6th-annual-china-oled-summit-jan-23-2017.html. [Accessed: 22-Jul-2018].

[250] “JOLED Establishes Nomi Site in Ishikawa -Commences Mass Production of Printed OLED in 2020,” 2018. [Online]. Available: https://www.j-oled.com/news-eng/2018-6-26e/. [Accessed: 22-Jul-2018].

[251] “Printed Flexible OLED Displays,” *Cambridge Displays Technology Ltd.*, 2016. [Online]. Available: https://www.cdtltd.co.uk/technology-scope/flexoled/. [Accessed: 22-Jul-2018].

[252] G. Grau *et al.*, “A development and evaluation of micro-gravure coater for printed electronics,” *Jpn. J. Appl. Phys.*, vol. 53, p. 05HC12, 2014.

[253] W. Song and J. Y. Lee, “Degradation Mechanism and Lifetime Improvement Strategy for Blue Phosphorescent Organic Light-Emitting Diodes,” *Adv. Opt. Mater.*, vol. 5, no. 9, p. 1600901, 2017.

[254] S. B. Meier, D. Tordera, A. Pertegás, C. Roldán-Carmona, E. Ortí, and H. J. Bolink, “Light-emitting electrochemical cells: Recent progress and future prospects,” *Mater. Today*, vol. 17, no. 5, pp. 217–223, 2014.

[255] “Liquid Light: For next generation packing, illumination and signage,” 2018. [Online]. Available: http://lunalec.com/. [Accessed: 23-Jul-2018].

[256] A. Sandström and L. Edman, “Towards High-Throughput Coating and Printing of Light-

Emitting Electrochemical Cells: A Review and Cost Analysis of Current and Future Methods," *Energy Technol.*, vol. 3, no. 4, pp. 329–339, 2015.

[257] S. Tang *et al.*, "Design rules for light-emitting electrochemical cells delivering bright luminance at 27.5 percent external quantum efficiency," *Nat. Commun.*, vol. 8, no. 1, 2017.

[258] B. Schmidt-Hansberg *et al.*, "Investigation of non-halogenated solvent mixtures for high throughput fabrication of polymerfullerene solar cells," *Sol. Energy Mater. Sol. Cells*, vol. 96, no. 1, pp. 195–201, 2012.

[259] J. Zimmermann, L. Porcarelli, T. Rödlmeier, A. Sanchez-Sanchez, D. Mecerreyes, and G. Hernandez-Sosa, "Fully Printed Light-Emitting Electrochemical Cells Utilizing Biocompatible Materials," *Adv. Funct. Mater.*, vol. 28, no. 24, p. 1705795, 2017.

[260] N. Kobayashi *et al.*, "DNA based electrolyte/separator for lithium battery application," *Proc. SPIE*, vol. 9557, p. 95570A, 2015.